

Chapter 15

Finite rate of innovation sampling

In previous chapters we have seen that the UoS model can pave the way to sub-Nyquist sampling of certain categories of structured analog signals. In this chapter we consider an alternative model that relies on parametric representations: *finite rate of innovation (FRI) signals* [105]. This class corresponds to families of functions defined by a finite number of parameters per unit time, a quantity referred to as the *rate of innovation*. More specifically, a FRI signal $x(t)$ is characterized by the fact that any finite duration segment of length r is completely determined by no more than k parameters. In this case, the function $x(t)$ is said to have a local rate of innovation equal to k/r . The FRI viewpoint complements the UoS framework: a signal may lie in a UoS and have FRI; however, not all FRI signals can be described by a UoS model and vice versa, as we will show in examples below.

Interest in this class of signals emerges from the observation that several commonly encountered FRI signals can be perfectly recovered from samples taken at their rate of innovation. The advantage of this result is self-evident: FRI signals need not be bandlimited, and even if they are, the Nyquist frequency may be much higher than their rate of innovation. Thus, by using FRI techniques, the sampling rate required for perfect reconstruction can be reduced substantially. However, exploiting these capabilities requires careful design of the sampling mechanism and of the digital postprocessing. One of the most popular families of functions studied within this framework is streams of pulses which appear in many applications including bio-imaging, radar, and spread-spectrum communication.

This chapter focuses on the theory, recovery techniques, and several applications of the FRI model. We mainly concentrate on pulse streams, and consider in particular the cases of periodic, finite, infinite, and semiperiodic pulse streams. Towards the end of the chapter we will also discuss more general FRI settings.

15.1 Finite rate of innovation signals

The signals we treat in this chapter are those that are determined by a finite number of parameters per time unit. FRI signals were introduced in [105] and are given formally by the following definition:

Definition 15.1. Let $N_r(t)$ denote a counting function that is equal to the number of parameters defining the segment of a signal $x(t)$ over the time interval $[t, t + r]$. The r -local rate of innovation of $x(t)$, denoted ρ_r , is defined as

$$\rho_r = \max_{t \in \mathbb{R}} \frac{N_r(t)}{r}. \quad (15.1)$$

The rate of innovation, ρ , is given by

$$\rho = \lim_{r \rightarrow \infty} \rho_r. \quad (15.2)$$

A signal is said to have a finite rate of innovation (FRI) if ρ is finite.

By definition, ρ_r measures the maximal number of parameters over an interval of length r . The rate of innovation is the limit of this value as r increases to infinity. Given an FRI signal with rate of innovation ρ , we expect to be able to recover $x(t)$ from a number of samples per unit time proportional to ρ . As we will see, for many types of FRI signals, recovery methods exist that operate at the rate of innovation. This rate turns out to have another interesting interpretation in the presence of noise: it is a lower bound on the ratio between the MSE achievable by any unbiased estimator of $x(t)$ and the noise variance, regardless of the sampling method [314].

Before discussing sampling and recovery of FRI signals, we begin by providing some examples of this class of functions.

15.1.1 Shift-invariant spaces

Perhaps the simplest example of a FRI signal corresponds to a SI function that can be expressed as

$$x(t) = \sum_{n \in \mathbb{Z}} a[n]h(t - n\tau) \quad (15.3)$$

for some sequence $a[n] \in \ell_2$, where $h(t)$ is a known pulse in L_2 and $\tau > 0$ is a given scalar¹. Intuitively, every signal lying in a SI space with spacing τ has one degree of freedom per τ seconds (corresponding to one coefficient from the sequence $a[n]$). It is thus tempting to regard the rate of innovation of such signals as $1/\tau$. As we now show, this is indeed the (asymptotic) rate of innovation for compactly supported pulses $h(t)$. For any finite window size r , the r -local rate of innovation ρ_r is generally larger.

Specifically, suppose that the support of $h(t)$ is contained in $[t_a, t_b]$ and consider intervals of the form $[t, t + r]$, where $r > 0$. Owing to the overlap of the pulses, for any such interval we can only assure that there are no more than $\lceil (t_b - t_a + r)/\tau \rceil$ coefficients $a[n]$ affecting the value of $x(t)$. This is demonstrated in Fig. 15.1(a). The r -local rate of innovation of signals of the form (15.3) is therefore

¹ We note that in earlier chapters the period of SI signals was denoted by T . In the context of FRI we will see that the sampling period is typically different than the underlying signal period. We therefore modify the notation so that T is used to denote the sampling period, while the signal period is represented by τ .

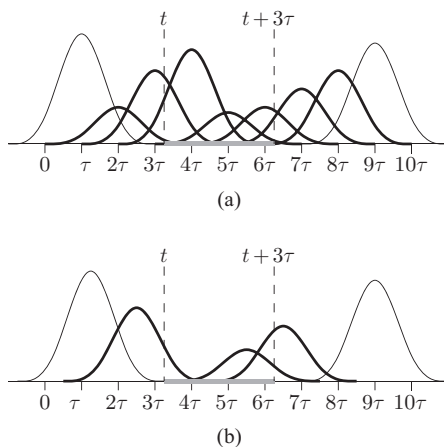


Figure 15.1 Streams of shifted versions of a pulse $h(t)$, supported on $[-2\tau, 2\tau]$. Bold pulses are those that affect the observation segment $[t, t + 3\tau]$. (a) Fixed pulse positions, spaced τ seconds apart. Here, the segment $[t, t + 3\tau]$ is affected by seven pulses so that $\rho_{3\tau} = 7/(3\tau)$. (b) Unknown pulse positions with minimal separation τ . Here, the rate of innovation is $\rho_{3\tau} = 2 \cdot 7/(3\tau) = 14/(3\tau)$. Note that the specific segment $[t, t + 3\tau]$ is affected only by three pulses so that there are $(2 \cdot 3)/(3\tau) = 2/\tau$ parameters per time unit at that location.

$$\rho_r = \frac{1}{r} \left\lceil \frac{t_b - t_a + r}{\tau} \right\rceil. \quad (15.4)$$

The rate of innovation, which is determined by taking r to infinity, is equal $1/\tau$.

We note that if $h(t)$ is not compactly supported, then the rate of innovation is infinite. Thus, for example, bandlimited signals (which correspond to $h(t) = \text{sinc}(t/\tau)$) are not FRI by Definition 15.1. This reflects the fact that it is impossible to recover any finite-duration segment $[t_a, t_b]$ of such signals from a finite number of measurements.

We have seen in earlier chapters that SI signals of the form (15.3) can be recovered from samples at rate $1/\tau$ irrespective of the bandwidth of $h(t)$. The recovery techniques we studied were based on simple filtering operations. Thus, in this case, sampling at the rate of innovation is sufficient to recover the signal using linear filtering methods. The SI model corresponds to a subspace prior. In contrast, many FRI families of signals form nonlinear signal models, rather than a subspace, but nonetheless can often still be sampled and perfectly reconstructed at the rate of innovation. In this case, though, more elaborate recovery techniques are needed, as shown later in the chapter.

15.1.2 Channel sounding

Single-burst channel sounding

A more complicated model than (15.3) results when the location of the pulses are unknown *a priori*, which often happens in channel sounding, ultrasound, and radar applications. Specifically, we have seen in Example 4.11 that in certain medium identification and channel sounding scenarios, as well as in radar and ultrasound, the echoes of a transmitted pulse $h(t)$ are analyzed to identify the positions and reflectance coefficients

of scatterers in the medium [399, 429, 430, 431, 432]. In these cases, the received signal has the form

$$x(t) = \sum_{\ell=1}^L a_\ell h(t - t_\ell), \quad (15.5)$$

where L is the number of scatterers and the amplitudes $\{a_\ell\}_{\ell=1}^L$ and time delays $\{t_\ell\}_{\ell=1}^L$ correspond to the reflectance and location of the scatterers. Such signals can be thought of as belonging to a UoS, where the parameters $\{t_\ell\}_{\ell=1}^L$ determine an L -dimensional subspace, and the coefficients $\{a_\ell\}_{\ell=1}^L$ describe the position within the subspace. Since there are infinitely many possible values for the parameters t_1, \dots, t_L we have a union of an infinite number of subspaces.

For any window of size $r > \max_\ell\{t_\ell\} - \min_\ell\{t_\ell\}$, the r -local rate of innovation is given by

$$\rho_r = \frac{2L}{r}. \quad (15.6)$$

Therefore, if the signal is defined on the interval $[0, \tau]$, then the local rate of innovation over τ is $2L/\tau$. This is consistent with the fact that the signal has $2L$ degrees of freedom over its domain.

Periodic channel sounding

Occasionally, channel sounding techniques consist of repeatedly probing the medium [433]. Assuming the medium does not change throughout the experiment, the result is a periodic signal

$$x(t) = \sum_{\ell=1}^L \sum_{n \in \mathbb{Z}} a_\ell h(t - t_\ell - n\tau). \quad (15.7)$$

As before, the set of feasible signals is an infinite union of finite-dimensional subspaces in which $\{t_\ell\}_{\ell=1}^L$ determine the subspace and $\{a_\ell\}_{\ell=1}^L$ define the position within the subspace. The r -local rate of innovation coincides with (15.6).

Semiperiodic channel sounding

Another interesting setting is when a channel consists of L paths whose amplitudes change, but the time delays can be assumed constant throughout the duration of the experiment [433, 434, 435]. One example where this occurs is in the context of radar applications in which the targets are moving at a constant velocity, as we discuss in Section 15.7.1. In these cases the received signal has the form:

$$x(t) = \sum_{\ell=1}^L \sum_{n \in \mathbb{Z}} a_\ell[n] h(t - t_\ell - n\tau), \quad (15.8)$$

where $a_\ell[n]$ is the amplitude of the ℓ th path at the n th probing experiment. This is, once again, a UoS, but here each subspace is infinite-dimensional, as it is determined by the infinite set of parameters $\{a_\ell[n]\}$.

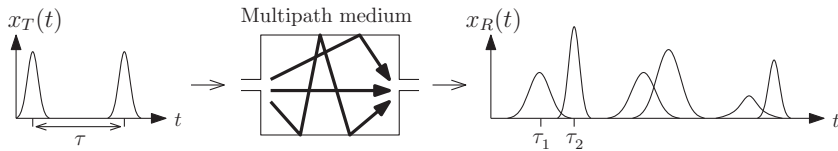


Figure 15.2 A multipath medium. Pulses with *a priori* known shape are transmitted over the channel. The output signal is composed of delayed and weighted replicas of the transmitted pulses.

The model (15.8) can also describe the case in which the signal consists of a finite number of periods. In this setting $n \in \mathbb{Z}$ is replaced by a finite sum over $n = 1, \dots, P$, as in the following example.

Example 15.1 The model (15.8) can be applied to time-varying channel estimation in wireless communications [434]. In this setting, the aim of the receiver is to estimate the channel's parameters from samples of the received signal [436]. In a typical scenario, pulses with *a priori* known shape are transmitted through a multipath medium, which consists of several propagation paths. As a result of the multiple paths, the received signal is composed of delayed and weighted replicas of the transmitted pulses, as illustrated in Fig. 15.2. In order to identify the medium, the time delay and gain coefficient of each multipath component has to be estimated from the received signal.

Consider a baseband communication system working with pulse amplitude modulation (PAM). The transmitted signal has the form

$$x_T(t) = \sum_{n=1}^N d[n]h(t - n\tau), \quad (15.9)$$

where $d[n]$ are the data symbols taken from a finite alphabet, and N is the total number of transmitted symbols. The signal $x_T(t)$ passes through a baseband time-varying multipath channel whose impulse response at time s to an impulse at time t is modeled as [399] $h(s, t) = \sum_{\ell=1}^L \alpha_\ell(t)\delta(s - \tau_\ell)$, where $\alpha_\ell(t)$ is the time-varying complex gain for the ℓ th multipath propagation path and τ_ℓ is the corresponding time delay. The total number of paths is denoted by L . We assume that the channel is slowly varying relative to the symbol rate, so that the path gains are considered to be constant over one symbol period:

$$\alpha_\ell(t) = \alpha_\ell[n\tau], \quad \text{for } t \in [n\tau, (n+1)\tau].$$

In addition, we confine the propagation delays to one symbol, i.e. $\tau_\ell \in [0, \tau]$. Under these assumptions, the received signal (in a noise-free environment) is given by

$$x_R(t) = \sum_{\ell=1}^L \sum_{n=1}^N a_\ell[n]h(t - \tau_\ell - n\tau), \quad (15.10)$$

where $a_\ell[n] = \alpha_\ell[n\tau]d[n]$.

This signal can be seen as a special case of (15.8). Thus, the techniques we study in this chapter can be used to sample such multipath signals at rates below Nyquist. The resulting sampling rate will depend only on the number of multipath components and the transmission rate, but not on the bandwidth of the transmitted pulse. This can lead to significant sampling rate reduction when only a small number of propagation paths exists, or when the bandwidth of the transmitted pulse is relatively high. This application is explored in more detail in [434].

Assume as in the SI setting that the support of $h(t)$ is contained in $[t_a, t_b]$, and consider intervals of the form $[t, t+r]$, where $r > 0$. Then, similar to the SI case, there are no more than $L \lceil (t_b - t_a + r)/\tau \rceil$ coefficients $a[n]$ affecting the value of $x(t)$ for every such interval. In addition, there are at most L unknown delays. Thus,

$$\rho_r = \frac{L}{r} \left(\left\lceil \frac{t_b - t_a + r}{\tau} \right\rceil + 1 \right). \quad (15.11)$$

Taking r to infinity, the rate of innovation is $\rho = L/\tau$, which is half the rate of the single-burst case. Here ρ is not affected by the fact that we do not know the L delays but rather is determined only by the L unknown amplitudes. This is because when we increase the observation period, the effect of the delays becomes negligible.

15.1.3 Other examples

Multi-carrier signals

The model (15.5) and its variants have received the largest amount of attention in the FRI literature. However, other interesting FRI signal classes exist. As an example, suppose that L transmissions of the form (15.3) are modulated, each with a different carrier frequency, to yield

$$x(t) = \sum_{\ell=1}^L \sum_{n \in \mathbb{Z}} a_\ell[n] h(t - n\tau) \sin(\omega_\ell t). \quad (15.12)$$

Here, $a_\ell[n]$ is the data transmitted by the ℓ th user on the carrier frequency ω_ℓ . This setting is analogous in many respects to the semiperiodic channel sounding case; in particular, the r -local rate of innovation is the same.

Continuous-phase modulation

The examples we discussed so far all correspond to special cases of a UoS. Clearly, not all UoS models are FRI: in particular, as we have seen, when $h(t)$ of (15.3) is not compactly supported then the corresponding model does not have a finite number of parameters per unit time. Conversely, although the UoS representation is currently the most common setting treated within the FRI literature, FRI signals do not have to conform to the UoS model. An example is continuous-phase modulation (CPM) transmissions. These include continuous-phase frequency shift keying (CPFSK) and minimum shift keying (MSK), tamed frequency modulation (TFM), Gaussian MSK (GMSK) and more. Here, the transmitted signal takes on the form

$$x(t) = \cos \left(\omega_0 t + 2\pi h \int_{-\infty}^t \sum_{n \in \mathbb{Z}} a[n] h(r - m\tau) dr \right), \quad (15.13)$$

where ω_0 is a fixed carrier frequency, $a[n] \in \{\pm 1, \pm 3, \dots, \pm(Q-1)\}$ are the message symbols, h is the modulation index, and $h(t)$ is a pulse shape that is supported on $[0, L\tau]$ for some integer $L > 0$ and satisfies $\int_0^{L\tau} h(t) dt = 0.5$.

The rate of innovation of CPM signals can be determined by expressing (15.13) as (see Exercise 2)

$$x(t) = \cos \left(\omega_0 t + \sum_{m \in \mathbb{Z}} \tilde{a}[m] \tilde{h}(t - m\tau) \right), \quad (15.14)$$

where $\tilde{a}[m] = \sum_{n=-\infty}^m a[n]$ and

$$\tilde{h}(t) = 2\pi h \int_{-\infty}^t (h(r) - h(r - \tau)) dr. \quad (15.15)$$

Since knowing $a[n]$ is equivalent to knowing $\tilde{a}[n]$ (up to initial boundary condition) and $\tilde{h}(t)$ is supported on $[0, (L+1)\tau]$, the number of coefficients affecting $x(t)$ on any interval $[t, t+r]$ is the same as in (15.3) with $t_a = 0$ and $t_b = (L+1)\tau$. Consequently, the r -local rate of innovation of CPM signals is

$$\rho_r = \frac{1}{r} \left(\left\lceil \frac{r + (L+1)\tau}{\tau} \right\rceil \right) \quad (15.16)$$

and their asymptotic rate is $1/\tau$.

Nonlinearly distorted shift-invariant spaces

Another example of an FRI model that is not a UoS is when a signal belonging to a UoS is distorted by a nonlinear operation. In Chapter 8 we considered in detail sampling in the presence of nonlinear distortions such as companding methods used to avoid clipping in various communication settings. If the original signal lies in a SI space with a compactly supported generator $h(t)$, then the resulting transmission takes the form

$$x(t) = M \left(\sum_{n \in \mathbb{Z}} a[n] h(t - n\tau) \right), \quad (15.17)$$

where $M(\cdot)$ is a nonlinear, invertible function. Clearly, the r -local rate of innovation ρ_r of this type of signal is the same as that of the underlying SI function, and is thus given by (15.4). As we have seen in Chapter 8, under appropriate conditions on the nonlinear distortion, $x(t)$ can be recovered from samples at the rate of innovation $1/\tau$.

Having presented several examples of FRI signals, we now study sampling theorems for this model. We begin by focusing on streams of pulses.

Periodic FRI signals turn out to be particularly convenient for analysis, and will be discussed in depth in Section 15.2. After introducing a matched-filtering approach to signal recovery, we will see that it is beneficial to analyze the problem in the frequency domain. In this domain, FRI recovery is equivalent to estimating a sum of sinusoids with unknown frequencies – a problem which has been well-studied in the array processing

literature. The techniques used in this setting can then be extended to treat more general pulse streams including the infinite and semi-infinite cases.

We focus on several key approaches to treating the sum-of-sinusoids problem, including Prony's method, Cadzow denoising, matrix pencil, MUSIC, ESPRIT, and algorithms based on compressed sensing. These techniques all assume that we are given Fourier coefficients of the periodic pulse stream from which the signal parameters are estimated. Approaches for obtaining such coefficients from low-rate samples of the signal are discussed in Sections 15.3 and 15.4. In Section 15.3 we treat two sub-Nyquist sampling methods based on single channel filters: coset sampling and sampling with a sum-of-sincs prefilter. Multichannel structures for sub-Nyquist sampling, including modulation banks and filter banks, are introduced in Section 15.4.

In Section 15.5 we discuss ultimate bounds that can be achieved when estimating FRI signals in the presence of noise. Iterative recovery techniques for general FRI models are treated in Section 15.6. We end the chapter with several applications of the pulse stream model to radar and ultrasound.

15.2 Periodic pulse streams

Consider a τ -periodic stream of pulses, defined as

$$x(t) = \sum_{\ell=1}^L \sum_{n \in \mathbb{Z}} a_\ell h(t - t_\ell - n\tau), \quad (15.18)$$

where $h(t)$ is a known pulse shape, τ is the known period, and $\{t_\ell, a_\ell\}_{\ell=1}^L, t_\ell \in [0, \tau], a_\ell \in \mathbb{C}, \ell = 1 \dots L$ are the unknown delays and amplitudes. Our goal is to sample $x(t)$ and reconstruct it, from a minimal number of samples. Since the signal has $2L$ degrees of freedom per period, we expect the minimal number of samples over one period to be $2L$. We are primarily interested in pulses which have large bandwidth corresponding to small time support. In this case the Nyquist rate of the signal $x(t)$ of (15.18) is high so that sub-Nyquist methods can be beneficial. Note that the bandwidth of $x(t)$ is no larger than that of $h(t)$ since delays and summations do not increase bandwidth.

When the number of degrees of freedom in $x(t)$ is less than its bandwidth, we expect to be able to recover $x(t)$ from a small number of measurements. The question, though, is how to choose these low-rate samples. Owing to the short time support, direct uniform sampling of $2L$ samples will typically result in many zeros, since the probability of a sample to hit a pulse is very low, as illustrated in Fig. 15.3(a). Therefore, more sophisticated sampling schemes must be designed.

In the previous chapter we developed techniques for low-rate sampling of multiband signals which were based on aliasing the signal in frequency prior to sampling. This aliasing allowed us to collapse the high bandwidth signal content onto a low-dimensional subspace which was then sampled at a low rate. We will follow a similar approach here, where now the aliasing is performed in time rather than in frequency. More specially, suppose that we spread each of the pulses prior to sampling, as illustrated in Fig. 15.3(b).

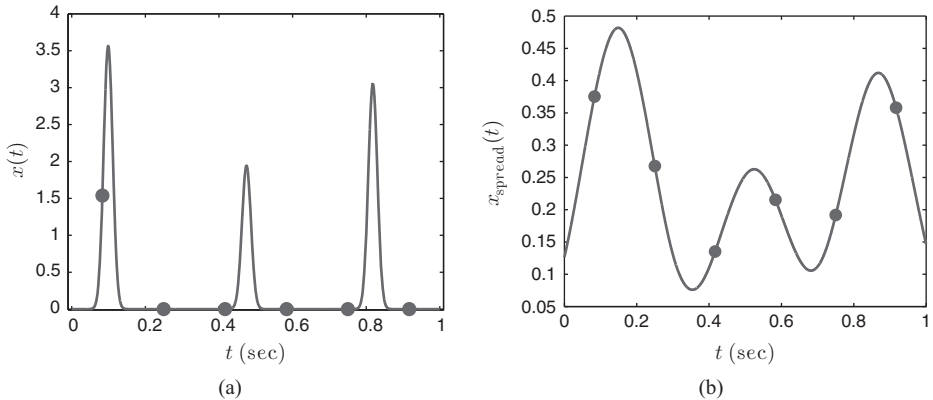


Figure 15.3 Direct uniform sampling of the pulse stream $x(t)$ of (15.18) and its time-aliased (spread) version. Here $h(t)$ is a Gaussian pulse with small variance $\sigma^2 = 3 \times 10^{-4}$, and the amplitudes and delays were chosen randomly. (a) Direct uniform sampling at a low rate. (b) Time-aliased version of $x(t)$ generated using a low-pass filter, and its (nonzero) samples.

This now enables sampling at a low rate while still acquiring information about the signal. Once the signal is sampled, we can gain back the seemingly lost resolution by employing appropriate recovery methods in the digital domain. These techniques exploit ideas from spectral analysis and compressed sensing by analyzing the stream of pulses in the frequency domain. Recovering the delays and amplitudes from the low rate samples will then correspond to determining the frequencies in a sum of complex exponentials from a small number of Fourier coefficients.

15.2.1 Time-domain formulation

We begin by considering standard time-domain methods for estimating the delays and amplitudes which are based on Nyquist-rate sampling of $x(t)$ in (15.18). The most popular (and simplest) approach is through a process known in the communication literature as a *rake receiver* [399]. This receiver was proposed back in the 1950s, and is designed to counter the effects of multipath fading.

To develop the rake receiver, suppose that $L = 1$ so that there is a single unknown delay. In the presence of noise, we then have that $x(t) \approx a_1 h(t - t_1)$ for $t \in [0, \tau]$ where a_1 and t_1 are the unknown amplitude and delay, respectively. To simplify the derivations, we assume that the pulse is normalized to unit energy so that $\int_0^\tau |h(t)|^2 dt = 1$ and that $h(t - t')$ is confined to $[0, \tau]$ for all possible delays t' . A reasonable approach to estimate a_1, t_1 is to seek the values that minimize the error:

$$\min_{a_1, t_1} \int_0^\tau |x(t) - a_1 h(t - t_1)|^2 dt. \quad (15.19)$$

This is also the maximum-likelihood estimate when the noise is Gaussian.

By differentiating the result and equating it to zero, we can see that the optimal value of a_1 is given by

$$a_1 = \frac{\int_0^\tau \overline{h(t-t_1)}x(t)dt}{\int_0^\tau |h(t-t_1)|^2 dt}. \quad (15.20)$$

By substituting this value back into the objective (15.19), the optimal value of t_1 can be computed as

$$t_1 = \arg \max_{t'} \frac{\left| \int_0^\tau \overline{h(t-t')}x(t)dt \right|^2}{\int_0^\tau |h(t-t')|^2 dt} = \arg \max_{t'} \left| \int_0^\tau \overline{h(t-t')}x(t)dt \right|^2, \quad (15.21)$$

where in the last equality we relied on the assumption that $h(t-t')$ is confined to $[0, \tau]$ for all feasible t' . To implement (15.21), we note that

$$y(t) = \int_0^\tau \overline{h(\alpha-t)}x(\alpha)d\alpha = \overline{h(-t)} * x(t). \quad (15.22)$$

Thus we can find t_1 by first creating the function $y(t)$ which is the convolution between $x(t)$ and $\overline{h(-t)}$, and then choosing t_1 as the value at which $|y(t)|$ obtains its maximum. This process is known as *matched filtering* [437].

When there are multiple delays, a popular approach is to follow the same procedure, where now the estimated delays are chosen as the arguments corresponding to the L largest values of $|y(t)|$. This method will no longer be optimal in general owing to the interference between overlapping pulses. If L is not known in advance, then it is common to choose all peaks that are beyond a given threshold, where the bound is often set as a percentage of the largest peak or as a function of the background noise level. Model order selection methods can also be used [17].

In practice, the matched filter (MF) is usually implemented digitally. Since the bandwidth of $y(t)$ is no larger than that of $h(t)$, the MF output $y(t)$ can be determined from its samples at the Nyquist rate, corresponding to the bandwidth of $h(t)$. Let $1/T$ denote the Nyquist rate of $y(t)$ and let $y[n] = y(nT)$. Then $y[n] = \overline{h[-n]} * x[n]$ where $h[n] = h(nT)$ and $x[n]$ are samples at rate $1/T$ of a bandlimited version of $x(t)$ (see Exercise 3). Therefore, to estimate t_1 one can first compute the digital MF output $y[n]$, as illustrated in Fig. 15.4, and then construct $y(t)$ by bandlimited interpolation of $y[n]$. Note that in the figure, instead of performing the MF operation and then sampling its output, one can equivalently sample $x(t)$ and then compute $y[n]$ digitally.

To retain computational efficiency, the sinc interpolation step is typically omitted entirely, or approximated by local interpolation. In the former case the delays are found on the discrete (Nyquist) grid; that is, we seek the peaks in $|y[n]|$ and estimate the delays as the values of n at which the peaks are attained. The performance of this simple MF strategy can be improved by first interpolating the discrete sequence $y[n]$ locally, for example using cubic interpolation, and then determining the peaks.

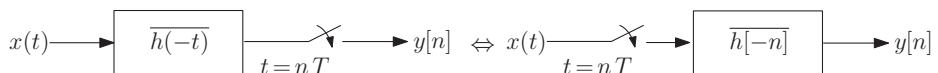


Figure 15.4 Matched filtering in the analog and digital domains.

Algorithm 15.1 Matched filtering

Input: Samples $x[n], h[n]$ of the received signal $x(t)$ and the pulse shape $h(t)$ respectively, with period τ
 Output: Time delays $t_\ell, \ell = 1, \dots, L$
 Create the matched-filter output $y[n] = \overline{h[-n]} * x[n]$
 Optional: apply local interpolation
 Find the L largest peaks of $|y[n]|$
 Determine t_ℓ as the values at which the maximum is obtained

Evidently, performing the MF operation in the digital domain requires sampling the data at the Nyquist rate or higher, in order to approximate the continuous MF output. If $h(t)$ is time-limited and has N nonzero Fourier coefficients over the interval $[0, \tau)$, then at least N samples are needed over the period τ . Equivalently, if $h(t)$ is bandlimited to $2\pi f_c$ and we consider its τ -periodic extension $h_\tau(t) = \sum_{k \in \mathbb{Z}} h(t + k\tau)$, then at least $f_c\tau$ samples per period are required. We summarize the MF approach to time-delay estimation in Algorithm 15.1.

The MF procedure is illustrated by the following example.

Example 15.2 Consider a signal $x(t) = \sum_{\ell=1}^L \sum_{n \in \mathbb{Z}} a_\ell h(t - t_\ell - n\tau)$ consisting of $L = 4$ pulses along the period $\tau = 1$. The waveform $h(t)$ is a sinc function with bandwidth equal to 81 Hz (this bandwidth is chosen in order to enable a comparison with the methods demonstrated in Examples 15.3 15.4 and 15.8). The rate of innovation of $x(t)$ is equal to $2L$ (see Exercise 5). The delays and amplitudes are set to $a_\ell = 1, t_\ell = \ell\Delta$, where Δ is a parameter. The signal is sampled at its Nyquist rate so that we have 81 samples of $x(t)$ along the period $\tau = 1$. The sampling phase is chosen randomly so that the delays are not aligned to a grid. We consider the case in which the signal $x(t)$ is contaminated by noise so that we are given noisy versions of the samples $x[n]$. The added noise is white Gaussian with variance $1/\text{SNR}$. The digital MF output $y[n]$ is computed by filtering the received sampled signal $x[n]$ with the sampled MF $h[n]$.

We estimate the delays and amplitudes using (15.21) and (15.20) in two ways. In the first, we approximate the values of $\{t_\ell\}$ on the Nyquist grid by seeking the maximum of the absolute MF output over the sampled data. In the second, we use local interpolation to improve the result. Figure 15.5 depicts the MSE (in a log scale) in estimating the delays and amplitudes as a function of the SNR averaged over 500 simulations, for two choices of Δ : distant delays, $\Delta = 0.2$, and close delays, $\Delta = 0.025$. The MF approach is compared with the performance of the matrix pencil method, a frequency-based technique described in Section 15.2.5. Observing the figures it can be seen that estimation using the MF method is limited by the sampling rate, particularly at high SNR. The superior performance of the frequency-based matrix pencil approach is clearly evident.

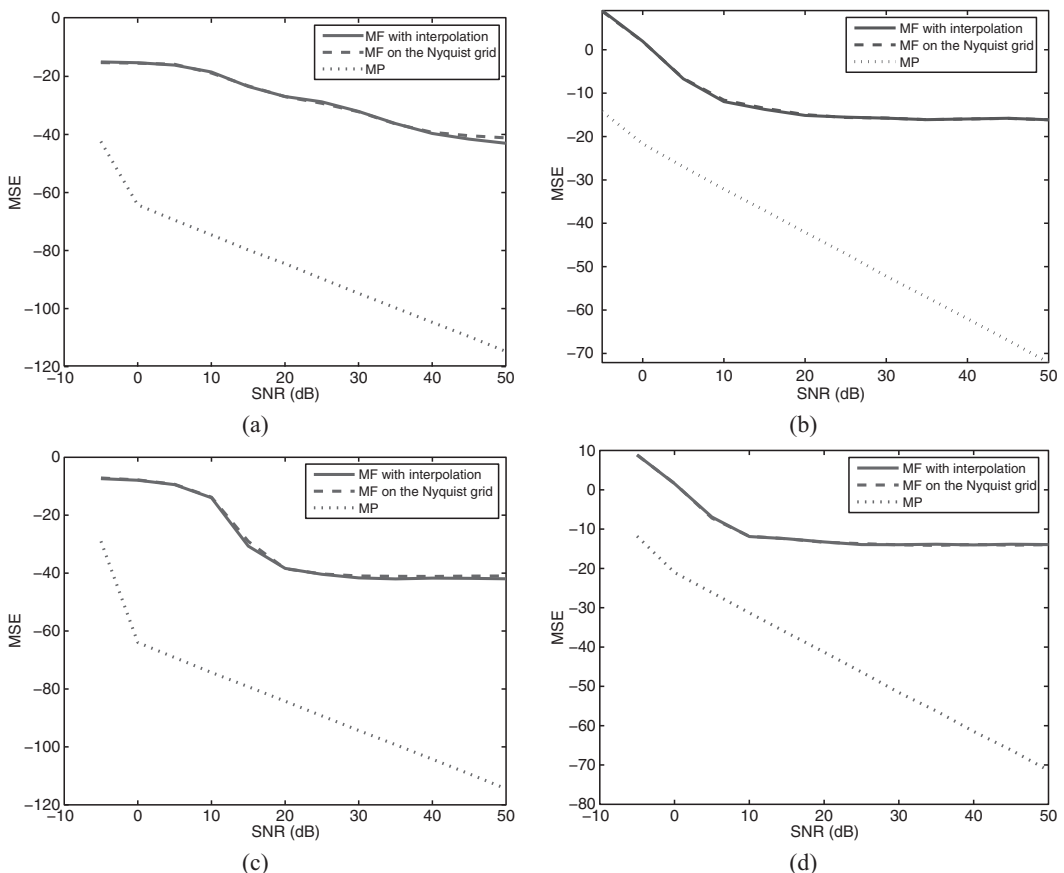


Figure 15.5 Delay and amplitude estimation using the MF and matrix pencil (MP) methods for $L = 4$. (a) MSE in estimating the delays $t_\ell = \ell\Delta$ for $\Delta = 0.2$. (b) MSE in estimating the amplitudes for $\Delta = 0.2$. (c) MSE in estimating the delays for $\Delta = 0.025$. (d) MSE in estimating the amplitudes for $\Delta = 0.025$.

The previous example illustrates that estimating the delays using a MF may lead to poor performance, especially for close delays. Furthermore, this approach requires sampling the data at the Nyquist rate which can be quite high when the underlying pulse $h(t)$ is very narrow in time, as is the case in many applications, particularly those involving localization (such as radar). In the next subsection we introduce a frequency-based framework for time-delay estimation which leads to several alternative recovery methods. These techniques can be adapted to operate on low-rate samples and tend to lead to superior performance when multiple targets are present.

15.2.2 Frequency-domain formulation

Instead of considering time-domain methods for delay estimation, we now analyze the signal in the Fourier domain. This allows us to connect our problem with that of spectral estimation and exploit powerful methods developed in that context, resulting in a

convenient route to sampling-rate reduction. These approaches tend to lead to better resolution in high enough SNR, namely, they improve the ability to distinguish between close delays. Compressed sensing techniques are also readily applicable in frequency, once again suggesting ways to recover the delays and amplitudes from low-rate samples in a robust fashion, particularly in low SNR regimes.

Fourier series representation

Consider the signal $x(t)$ of (15.18). Since $x(t)$ is periodic, we can represent it in terms of its Fourier series. To this end, define the periodic continuation of $h(t)$ as $f(t) = \sum_{m \in \mathbb{Z}} h(t + m\tau)$. Using Poisson's summation formula (3.89) with $x(t') = h(t' + t)$, $f(t)$ may be written as

$$f(t) = \frac{1}{\tau} \sum_{k \in \mathbb{Z}} H\left(\frac{2\pi k}{\tau}\right) e^{j2\pi kt/\tau}, \quad (15.23)$$

where $H(\omega)$ denotes the CTFT of the pulse $h(t)$. Substituting (15.23) into (15.18) we obtain

$$\begin{aligned} x(t) &= \sum_{\ell=1}^L a_\ell f(t - t_\ell) \\ &= \sum_{k \in \mathbb{Z}} \left(\frac{1}{\tau} H\left(\frac{2\pi k}{\tau}\right) \sum_{\ell=1}^L a_\ell e^{-j2\pi k t_\ell / \tau} \right) e^{j2\pi k t / \tau} \\ &= \sum_{k \in \mathbb{Z}} X[k] e^{j2\pi k t / \tau}, \end{aligned} \quad (15.24)$$

where we denoted

$$X[k] = \frac{1}{\tau} H\left(\frac{2\pi k}{\tau}\right) \sum_{\ell=1}^L a_\ell e^{-j2\pi k t_\ell / \tau}. \quad (15.25)$$

The expansion in (15.24) is the Fourier series representation of the τ -periodic signal $x(t)$ with Fourier coefficients given by (15.25).

We next show that if $2L$ or more consecutive Fourier coefficients of $x(t)$ are given, then $\{t_\ell, a_\ell\}_{\ell=1}^L$ can be determined from (15.25) using the fact that $h(t)$ is known. This number of coefficients is typically much smaller than the number N of nonzero values of $H\left(\frac{2\pi k}{\tau}\right)$ which is the number of samples obtained over τ when sampling at the Nyquist rate. Furthermore, if we are willing to recover the delays on a grid, then we can formulate the recovery in the frequency domain using tools of CS (see Chapter 11). This will allow for robust recovery in the presence of strong noise. In Section 15.3 we discuss methods to obtain the required Fourier coefficients from low-rate samples of $x(t)$ in the time domain. Intuitively, since only on the order of $2L$ Fourier measurements are needed, these can be obtained from low-rate samples in time. Thus, the ability to recover $x(t)$ from a small number of Fourier coefficients immediately implies that low-rate sampling is possible, where the number of samples is equal to the number of Fourier coefficients used in the recovery process.

Sum-of-sinusoids problem

Suppose we are given $m \geq 2L$ coefficients $X[k], k \in \mathcal{K}$ where \mathcal{K} is a consecutive index set of size $|\mathcal{K}| = m$. We assume that \mathcal{K} can be chosen such that $H\left(\frac{2\pi k}{\tau}\right) \neq 0$ for $k \in \mathcal{K}$. Let $Y[k] = \tau X[k]/H\left(\frac{2\pi k}{\tau}\right)$. Then,

$$Y[k] = \sum_{\ell=1}^L a_\ell e^{-j\omega_\ell k}, \quad k \in \mathcal{K}, \quad (15.26)$$

where $\omega_\ell = 2\pi t_\ell/\tau$. The problem (15.26) has been studied extensively in the array processing literature and is referred to as the *sum-of-sinusoids problem*. The goal is to recover the unknown frequencies ω_ℓ and unknown amplitudes a_ℓ from the sums $Y[k]$. Many methods have been proposed to recover the unknown frequencies, several of which we outline below. Further details can be found for example in [438]. These techniques allow exact recovery when there is no noise, and work well in small to moderate noise levels. However, when the noise increases, it is very difficult to determine ω_ℓ . An alternative is to discretize the possible frequency values so that we assume $\omega_\ell = (2\pi/\tau)\Delta s_\ell$ for some integer s_ℓ where Δ is the chosen time resolution. By discretizing the delays, we can formulate (15.26) within the framework of CS and use any of the methods for sparse vector recovery to determine the values of s_ℓ . This approach is typically more robust in the presence of noise, although it entails a loss of resolution due to the discretization.

Once the values of ω_ℓ are found, the amplitudes a_ℓ can be determined by solving a simple least-squares problem:

$$\min_{a_\ell} \sum_{k \in \mathcal{K}} \left| Y[k] - \sum_{\ell=1}^L a_\ell e^{-j\omega_\ell k} \right|^2. \quad (15.27)$$

To solve (15.27) let \mathcal{K} consist of the values k_1, k_2, \dots, k_m with $k_m = k_1 + (m-1)$ for some value k_1 . We can then express the objective in matrix form as

$$\min_{\mathbf{a}} \|\mathbf{y} - \mathbf{V}(\{\omega_\ell\}, k_1)_{m \times L} \mathbf{a}\|^2, \quad (15.28)$$

where $\mathbf{a} = [a_1, \dots, a_L]^T$ is the vector containing the unknown amplitudes, \mathbf{y} is the length- m vector of measurements $Y[k], k \in \mathcal{K}$, and

$$\mathbf{V}(\{\omega_\ell\}, k_1)_{m \times L} = \begin{bmatrix} e^{-j\omega_1 k_1} & e^{-j\omega_2 k_1} & \dots & e^{-j\omega_L k_1} \\ e^{-j\omega_1 k_2} & e^{-j\omega_2 k_2} & \dots & e^{-j\omega_L k_2} \\ \vdots & & & \vdots \\ e^{-j\omega_1 k_m} & e^{-j\omega_2 k_m} & \dots & e^{-j\omega_L k_m} \end{bmatrix}. \quad (15.29)$$

When $k_1 = 0$ we use the notation

$$\mathbf{V}(\{\omega_\ell\})_{m \times L} = \begin{bmatrix} 1 & 1 & \dots & 1 \\ e^{-j\omega_1} & e^{-j\omega_2} & \dots & e^{-j\omega_L} \\ \vdots & & & \vdots \\ e^{-j\omega_1(m-1)} & e^{-j\omega_2(m-1)} & \dots & e^{-j\omega_L(m-1)} \end{bmatrix}, \quad (15.30)$$

which is an $m \times L$ Vandermonde matrix with roots $\lambda_i = e^{-j\omega_i}$. Note that $\mathbf{V}(\{\omega_\ell\}, k_1)_{m \times L}$ can be expressed as $\mathbf{V}(\{\omega_\ell\}, k_1) = \mathbf{V}(\{\omega_\ell\}) \operatorname{diag}(e^{-j\omega_1 k_1}, e^{-j\omega_2 k_1}, \dots, e^{-j\omega_L k_1})$.

Throughout the chapter we will rely on several useful properties of Vandermonde matrices. In particular, an important result which we use often is the following (see Appendix A):

Proposition 15.1. *Let \mathbf{V} be an $m \times n$ Vandermonde matrix with $m \geq n$ and roots λ_i so that $V_{i\ell} = \lambda_\ell^i$. Then \mathbf{V} has full column-rank if and only if the roots are distinct. In this case it holds in addition that any n rows of \mathbf{V} are linearly independent.*

Assuming that $e^{-j\omega_i}$ are distinct, the solution to (15.28) is given by (see Appendix A)

$$\hat{\mathbf{a}} = (\mathbf{V}^* \mathbf{V})^{-1} \mathbf{V}^* \mathbf{y}, \quad (15.31)$$

where for brevity we denoted $\mathbf{V} = \mathbf{V}(\{\omega_\ell\})_{m \times L}$. Since \mathbf{V} is Vandermonde with $m \geq L$, $\mathbf{V}^* \mathbf{V}$ is invertible.

In the next subsections we outline several methods for recovering the frequencies $\{\omega_\ell\}$ in (15.26):

1. Prony's method and its extensions: total least-squares Prony, Cadzow denoising;
2. Matrix pencil;
3. Subspace methods: Pisarenko and MUSIC;
4. Correlation methods;
5. Compressed sensing formulation.

For simplicity, we assume throughout that $k_1 = 0$. The first four methods are based on spectral analysis techniques and recover the frequencies exactly when the number of measurements $m \geq 2L$ and there is no noise. The last approach is based on discretizing the frequencies (or delays), but is more robust in the presence of moderate to large noise. To describe the various techniques we rewrite (15.26) as a power series

$$Y[k] = \sum_{\ell=1}^L a_\ell u_\ell^k, \quad (15.32)$$

where $u_\ell = e^{-j\omega_\ell}$. Our goal then is to recover $\{u_\ell\}$ from a small number $m \geq 2L$ of Fourier coefficients $Y[k]$.

Before concluding this section we note that our derivations below are based on the model (15.26) (or (15.32)). To arrive at this formulation, we divided the Fourier coefficients of the signal $X[k]$ by those of the pulse shape $H(2\pi k/\tau)$. When the pulse is relatively flat, this is a reasonable route to take. However, if the pulse decays in frequency, then dividing by $H(2\pi k/\tau)$ can lead to noise enhancement. In such cases we may prefer a MF approach where we multiply $X[k]$ by $\overline{H(2\pi k/\tau)}$, or if the noise variance σ^2 is known, then we can use a Wiener prefilter. This corresponds to multiplying $X[k]$ by

$$W[k] = \frac{\overline{H(2\pi k/\tau)}}{|H(2\pi k/\tau)|^2 + \sigma^2}. \quad (15.33)$$

Note that when $\sigma \rightarrow 0$, namely, the noise is low, $W[k]$ approaches $1/H(2\pi k/\tau)$. On the other hand, in low SNR corresponding to large σ^2 , $W[k]$ is proportional to the MF $H(2\pi k/\tau)$. For the remainder of this chapter, we continue to assume the model (15.26) (or (15.32)).

15.2.3 Prony's method

Prony's method [196] for estimating $\{u_\ell\}$ in (15.32) begins by defining a filter $G(z)$ whose roots equal the values u_ℓ to be found:

$$G(z) = \sum_{\ell=0}^L g_\ell z^{-\ell} = \prod_{\ell=1}^L (1 - u_\ell z^{-1}), \quad (15.34)$$

where $\{g_\ell\}_{\ell=0}^L$ are the filter coefficients. The important property of $G(z)$ is that it *annihilates* the measurements $Y[k]$. Specifically, define the sequence $q[k] = g_k * Y[k]$ as the convolution of g_k and $Y[k]$. Then, for $L \leq k \leq m-1$ we have

$$q[k] = \sum_{i=0}^L g_i Y[k-i] = \sum_{i=0}^L \sum_{\ell=1}^L a_\ell g_i u_\ell^{k-i} = \sum_{\ell=1}^L a_\ell u_\ell^k \underbrace{\sum_{i=0}^L g_i u_\ell^{-i}}_{=0} = 0 \quad (15.35)$$

where the last equality is due to the fact that $G(u_\ell) = 0$. Note that $m-1 \geq L$ since $m \geq 2L$. The filter $\{g_\ell\}$ is therefore called an *annihilating filter*. Its roots uniquely define $\{u_\ell\}$, provided that these values are distinct. We can thus recover $\{u_\ell\}$ once we determine the filter coefficients $\{g_\ell\}$ (up to a scaling factor which does not affect the resulting zeros).

The identity in (15.35) can be written in matrix/vector form as

$$\mathbf{Y}_{(m-L) \times (L+1)} \mathbf{g} = \mathbf{0}, \quad (15.36)$$

where $\mathbf{g} = [g_L, \dots, g_1, g_0]^T$ and $\mathbf{Y}_{s \times n}$ is the data matrix defined by

$$\mathbf{Y}_{s \times n} = \begin{pmatrix} Y[0] & Y[1] & \cdots & Y[n-1] \\ Y[1] & Y[2] & \cdots & Y[n] \\ \vdots & \vdots & \ddots & \vdots \\ Y[s-1] & Y[s] & \cdots & Y[s+n-2] \end{pmatrix}. \quad (15.37)$$

When the dimensions are clear from the context, we use the shorthand notation $\mathbf{Y} = \mathbf{Y}_{s \times n}$. Note that the $k\ell$ th element of \mathbf{Y} is given by

$$\mathbf{Y}_{k\ell} = Y[k+\ell], \quad k = 0, \dots, s-1 \text{ and } \ell = 0, \dots, n-1, \quad (15.38)$$

thus it depends only on the sum $k+\ell$. This results in a matrix whose skew-diagonals are all equal and is called a *Hankel matrix*. The Cadzow technique below exploits this property to improve recovery in the presence of noise.

In order to be able to uniquely identify the vector of unknowns \mathbf{g} (up to scaling) we need to ensure that the null space of $\mathbf{Y}_{(m-L) \times (L+1)}$ has dimension equal to 1. For this to happen, we must have that the number of rows $s = m-L$ satisfies $s \geq n-1$.

where $n = L + 1$ denotes the number of columns. This is because if $s \leq n - 2$ then the null space will always have dimension at least 2. Substituting in the values of s and n , we arrive at the condition $m \geq 2L$. Thus, we need at least $2L$ consecutive values of $Y[k]$ to solve (15.36). In Proposition 15.2 (and Corollary 15.1) below we show that this condition is also sufficient, namely, if $m \geq 2L$ then there is a unique solution to (15.36) (up to scaling). Once the filter has been found, the locations $\{t_\ell\}$ are retrieved from the zeros $\{\omega_\ell\}$ of (15.34) via $u_\ell = e^{-j\omega_\ell}$ and $\omega_\ell = 2\pi t_\ell/\tau$. Given the locations, the weights $\{a_\ell\}$ can be obtained by (15.31).

Proposition 15.2. *Suppose that the values of $Y[k]$ in (15.36) are not equal to zero and let $\mathbf{Y} = \mathbf{Y}_{s \times n}$ be the matrix defined by (15.37). Then we can express \mathbf{Y} as*

$$\mathbf{Y} = \mathbf{V}(\{\omega_\ell\})_{s \times L} \operatorname{diag}(\mathbf{a}) \mathbf{V}^T(\{\omega_\ell\})_{n \times L}, \quad (15.39)$$

where \mathbf{a} is the length- L vector of coefficients a_ℓ . In addition, if $s, n \geq L$ then the rank of \mathbf{Y} satisfies $\operatorname{rank}(\mathbf{Y}) = L$.

Proposition 15.2 is related to the well-known Caratheodory–Toeplitz theorem [197, 439] which states that any nonnegative definite Toeplitz matrix can be represented in a similar form as (15.39) with $a_\ell \geq 0$ and \mathbf{V}^T replaced by \mathbf{V}^* .

Proof: To prove the proposition, we note that for any two matrices \mathbf{A}, \mathbf{B} with L columns $\mathbf{a}_\ell, \mathbf{b}_\ell$ and a diagonal matrix $\mathbf{D} = \operatorname{diag}(\mathbf{d})$ with diagonal elements d_ℓ we have

$$\mathbf{A} \operatorname{diag}(\mathbf{d}) \mathbf{B}^T = \sum_{\ell=1}^L d_\ell \mathbf{a}_\ell \mathbf{b}_\ell^T. \quad (15.40)$$

Let $\mathbf{C} = \mathbf{V}(\{\omega_\ell\})_{s \times L} \operatorname{diag}(\mathbf{a}) \mathbf{V}^T(\{\omega_\ell\})_{n \times L}$. Then, applying (15.40) to (15.39), we can write

$$\mathbf{C} = \sum_{\ell=1}^L a_\ell \mathbf{e}(\omega_\ell)_s \mathbf{e}^T(\omega_\ell)_n, \quad (15.41)$$

where $\mathbf{e}(\omega_\ell)_s$ is the length- s vector defined by

$$\mathbf{e}(\omega_\ell)_s = \begin{pmatrix} 1 \\ e^{-j\omega_\ell} \\ \vdots \\ e^{-j\omega_\ell(s-1)} \end{pmatrix} = \begin{pmatrix} 1 \\ u_\ell \\ \vdots \\ u_\ell^{(s-1)} \end{pmatrix}. \quad (15.42)$$

Therefore, the km th value of \mathbf{C} for $k = 0, \dots, s - 1$ and $m = 0, \dots, n - 1$ is equal to

$$c_{km} = \sum_{\ell=1}^L a_\ell u_\ell^k u_\ell^m = \sum_{\ell=1}^L a_\ell u_\ell^{k+m} = Y[k + m], \quad (15.43)$$

where we used (15.32). From (15.38) it follows that $\mathbf{C} = \mathbf{Y}$.

We next use (15.39) to prove that $\operatorname{rank}(\mathbf{Y}) = L$. From Proposition 15.1, $\mathbf{V}(\{\omega_\ell\})_{s \times L}$ has full column-rank equal to L and $\mathbf{V}^T(\{\omega_\ell\})_{n \times L}$ has full row-rank equal to L . Finally,

Algorithm 15.2 Prony's method (combined with TLS)

Input: $m \geq 2L$ measurements $Y[k], k = 0, \dots, m - 1$, number of delays L

Output: Time delays $t_\ell, \ell = 1, \dots, L$

Build the measurement matrix $\mathbf{Y}_{(m-L) \times (L+1)}$ of (15.37)

Choose $\mathbf{g} = [g_L, \dots, g_1, g_0]^T$ as a right singular vector of $\mathbf{Y}_{(m-L) \times (L+1)}$ corresponding to its smallest singular value

Find the L roots $\{u_\ell\}$ of $G(z) = \sum_{\ell=0}^L g_\ell z^{-\ell}$

Determine t_ℓ via $u_\ell = e^{-j\omega_\ell}$ and $\omega_\ell = 2\pi t_\ell/\tau$

since $a_\ell \neq 0$, $\text{diag}(\mathbf{a})$ is invertible so that its rank is also equal to L . We now rely on the following lemma, whose proof is straightforward (see Exercise 3).

Lemma 15.1. *Let $\mathbf{A}_{n \times m}$ with $n \geq m$ be a full column-rank matrix, let $\mathbf{C}_{m \times k}$ with $m \leq k$ be a full row-rank matrix, and let \mathbf{B} be a matrix with rank r . Then the rank of \mathbf{ABC} is equal to r .*

From Lemma 15.1 and (15.39) it follows immediately that the rank of \mathbf{Y} equals L , as long as $n, s \geq L$. \square

Corollary 15.1. *Suppose that the values of $Y[k]$ in (15.36) are not identically equal to zero and let $m \geq 2L$. Then there is a unique (nonzero) solution to (15.36) (up to scaling).*

Proof: From Proposition 15.2, the rank of $\mathbf{Y}_{(m-L) \times (L+1)}$ is equal L as long as $m - L \geq L$, or $m \geq 2L$. The dimension of the null space is therefore equal to $L + 1 - L = 1$. \square

Prony's method is summarized in Algorithm 15.2. In the literature, this approach is also referred to as the *annihilating filter method*. In line 4 of the algorithm description we included the total least-squares step which will be described in the next subsection. In the noise-free setting in which there exists a \mathbf{g} solving $\mathbf{Y}_{(m-L) \times (L+1)}\mathbf{g} = \mathbf{0}$, this step is identical to finding \mathbf{g} in the null space of \mathbf{Y} .

This technique can be improved by noticing that in addition to (15.35) we also have the relation:

$$\sum_{i=0}^L g_i \overline{Y[k+i]} = \sum_{i=0}^L \sum_{\ell=1}^L \overline{a_\ell} g_i u_\ell^{-(k+i)} = \sum_{\ell=1}^L \overline{a_\ell} u_\ell^{-k} \sum_{i=0}^L g_i u_\ell^{-i} = 0, \quad (15.44)$$

for $0 \leq k \leq m - L - 1$. This relation can be written in matrix/vector form as

$$\overline{\mathbf{Y}}_{(m-L) \times (L+1)} \mathbf{J} \mathbf{g} = \mathbf{0}, \quad (15.45)$$

where

$$\mathbf{J} = \begin{pmatrix} 0 & \dots & 0 & 1 \\ 0 & \dots & 1 & 0 \\ \vdots & & & \vdots \\ 1 & \dots & 0 & 0 \end{pmatrix}. \quad (15.46)$$

The matrix \mathbf{J} flips the elements in the vector \mathbf{g} so that $\mathbf{J}\mathbf{g} = [g_0, g_1, \dots, g_L]^T$. Alternatively, $\bar{\mathbf{Y}}\mathbf{J}$ flips the order of the columns in $\bar{\mathbf{Y}}$. Combining (15.36) and (15.45) leads to more equations, which may be useful in order to render the solution more robust in the presence of noise.

15.2.4 Noisy samples

When the samples are noisy, several possible modifications to Prony's method have been suggested in order to improve the robustness of the estimates.

Total least-squares approach

One possibility is to combine Prony's algorithm with the total least-squares (TLS) [440] approach. Specifically, in the presence of noise, the measurements $\{Y[k]\}$ are not known precisely, and consequently we only have access to a noisy version of \mathbf{Y} , which we denote here by $\tilde{\mathbf{Y}}$. For notational brevity, we have omitted the indices. Thus, instead of having $\mathbf{Y}\mathbf{g} = \mathbf{0}$ as in (15.36) we have $\tilde{\mathbf{Y}}\mathbf{g} \approx \mathbf{0}$. The TLS technique seeks the vector \mathbf{g} that minimizes the squared-norm of $\tilde{\mathbf{Y}}\mathbf{g}$. To preclude the trivial solution $\mathbf{g} = \mathbf{0}$, without loss of generality, we constrain the norm of \mathbf{g} to be equal to 1, resulting in

$$\min_{\mathbf{g}} \|\tilde{\mathbf{Y}}\mathbf{g}\|^2 \quad \text{s. t. } \|\mathbf{g}\|^2 = 1. \quad (15.47)$$

Clearly, if $\tilde{\mathbf{Y}} = \mathbf{Y}$ so that there is no noise, then the minimum value is 0 and \mathbf{g} is a normalized vector in the null space of \mathbf{Y} .

From the properties of the SVD (see Appendix A) it follows that the vector solving (15.47) is given by the right singular vector corresponding to the smallest singular value of $\tilde{\mathbf{Y}}$. Once the filter \mathbf{g} is found, one can determine its roots and identify the time delays, as in Prony's method.

Although Prony's algorithm is simple, when the measurements $Y[k]$ are noisy, the error in estimating $\{t_\ell\}$ can be quite large even when the TLS approach is used, as we show below in Example 15.3. Furthermore, it is known that the resulting estimates are not consistent [441], namely, the estimates do not necessarily converge in probability to their true values as the number of samples increases.

Cadzow iterative denoising algorithm

One way to improve the performance of TLS is to reduce the noise prior to applying (15.47). Tufts and Kumaresan [442], and Rahman and Yu [443], proposed exploiting the fact that the noise-free matrix $\mathbf{Y}_{(m-L) \times (L+1)}$ of (15.37) has rank L (for $m \geq 2L$), as we showed in Proposition 15.2 (and Corollary 15.1). This fact can be used to first approximate the noisy matrix $\tilde{\mathbf{Y}}$ by its best rank- L approximation using the SVD (see Theorem A.4 in Appendix A), and then apply the TLS method to the resulting rank- L matrix. Since $\tilde{\mathbf{Y}}$ is of size $(m - L) \times (L + 1)$ its rank is upper-bounded by $\text{rank}(\tilde{\mathbf{Y}}) \leq \min(m - L, L + 1)$. If $m = 2L$, then $\text{rank}(\tilde{\mathbf{Y}}) \leq L$ so that the best rank- L approximation is the matrix itself. Therefore, this approach is beneficial only when $m > 2L$.

A further improvement was suggested by Cadzow [444]; in addition to the rank, Cadzow proposed incorporating the fact that \mathbf{Y} is a Hankel matrix as we saw in (15.38).

Algorithm 15.3 Cadzow denoising

```

Input: Noisy measurement matrix  $\tilde{\mathbf{Y}}$ 
Output: Denoised matrix  $\mathbf{Y}$  (which can then be used in Prony's method)
Initialize:  $\mathbf{Y}_0 = \tilde{\mathbf{Y}}, \ell = 0$ 
while halting criterion false do
     $\ell \leftarrow \ell + 1$ 
    Compute the SVD  $\mathbf{Y}_\ell = \mathbf{U}\mathbf{S}\mathbf{V}^*$ , where  $\mathbf{U}$  and  $\mathbf{V}$  are unitary and  $\mathbf{S}$  is diagonal
    Build the diagonal matrix  $\mathbf{S}'$  consisting of the  $L$  largest elements in  $\mathbf{S}$ , and zero
        elsewhere
     $\mathbf{B} = \mathbf{U}\mathbf{S}'\mathbf{V}^*$  {construct best rank- $L$  approximation}
     $\mathbf{A} = \text{Hankel}(\mathbf{B})$  {construct best Hankel approximation}
     $\mathbf{Y}_\ell \leftarrow \mathbf{A}$ 
end while
return  $\mathbf{Y} \leftarrow \mathbf{Y}_\ell$ 

```

Cadzow denoising consists of first finding a rank- L Hankel matrix that is as close as possible to $\tilde{\mathbf{Y}}$ by solving

$$\min_{\mathbf{Y}'} \|\tilde{\mathbf{Y}} - \mathbf{Y}'\|_F^2 \quad \text{s. t. rank}(\mathbf{Y}') \leq L \text{ and } \mathbf{Y}' \text{ is Hankel}, \quad (15.48)$$

and then using the resulting estimate with TLS. In the objective, $\|\mathbf{A}\|_F^2 = \text{Tr}(\mathbf{A}^*\mathbf{A})$ denotes the Frobenius norm. This approximation is meaningful even when m is equal to its minimal value $m = 2L$.

An approximate solution to (15.48) can be computed by alternating between finding the best rank- L estimate, and determining the optimal Hankel approximation. Thus, for a given target matrix \mathbf{C} , we independently solve the two optimization problems

$$\min_{\mathbf{B}} \|\mathbf{C} - \mathbf{B}\|_F^2 \quad \text{s. t. rank}(\mathbf{B}) = L \quad (15.49)$$

and

$$\min_{\mathbf{A}} \|\mathbf{B} - \mathbf{A}\|_F^2 \quad \text{s. t. } \mathbf{A} \text{ is Hankel}. \quad (15.50)$$

To solve (15.49), we compute the SVD $\mathbf{C} = \mathbf{U}\mathbf{S}\mathbf{V}^*$ of \mathbf{C} , where \mathbf{U} and \mathbf{V} are unitary and \mathbf{S} is a diagonal matrix whose diagonal entries are the singular values of \mathbf{C} . We then discard all but the L largest singular values in \mathbf{S} . In other words, we construct a diagonal matrix \mathbf{S}' whose diagonal contains the L largest entries in \mathbf{S} , and is zero elsewhere. The rank- L matrix closest to \mathbf{C} is then given by $\mathbf{B} = \mathbf{U}\mathbf{S}'\mathbf{V}^*$ (see Appendix A). The solution to (15.50) is easily obtained by averaging the skew-diagonals of \mathbf{B} (see Exercise 8). The resulting iterative algorithm is summarized in Algorithm 15.3. In the algorithm description, $\text{Hankel}(\mathbf{B})$ denotes the operation of replacing \mathbf{B} by a Hankel matrix obtained by averaging the skew-diagonals.

Applying even a small number of iterations of Cadzow's algorithm tends to yield a matrix whose error with respect to the true unknown data matrix is much lower than the

error of the original measurement matrix $\tilde{\mathbf{Y}}$. The denoised matrix \mathbf{Y} can then be used in conjunction with the TLS technique.

We note that from Proposition 15.2, the noise-free matrix $\mathbf{Y}_{s \times n}$ of (15.37) has rank equal to L , as long as $n, s \geq L$. Therefore, we can apply Cadzow iterations to the matrix $\mathbf{Y}_{s \times n}$ with any $n, s \geq L$. In order to sum over a large number of values when averaging the diagonals, in the simulations below we choose \mathbf{Y} to be a square matrix of dimensions $n = s = \lfloor m/2 \rfloor$. After denoising, we reshape the data matrix to have dimensions $(m - L) \times (L + 1)$ and then use TLS and Prony's method. As the number of samples m and/or delays L increase, the superiority of choosing \mathbf{Y} to be square for denoising is more noticeable.

Example 15.3 In this example we examine Prony's method combined with the TLS approach and Cadzow denoising. In particular, we demonstrate the benefits of using Cadzow denoising and its effects on estimation accuracy. We will also highlight some drawbacks of this approach.

The signal we consider is the same as in Example 15.2: $x(t) = \sum_{\ell=1}^L \sum_{n \in \mathbb{Z}} a_\ell h(t - t_\ell - n\tau)$ along the period $\tau = 1$ where $a_\ell = 1$, $t_\ell = \ell\Delta$, and $\Delta = 0.025$. The samples are corrupted by noise (in the frequency domain) so that we are given $m \geq 2L$ noisy versions of the coefficients $Y[k]$, $k \in \mathcal{K}$ where \mathcal{K} is a consecutive index set of size m . The additive noise is complex white Gaussian with variance chosen to match the required SNR. The noisy matrix coefficients (which we earlier denoted by $\tilde{\mathbf{Y}}$) are denoised using Cadzow's algorithm. The delays are then estimated using Prony's method combined with the TLS approach. Finally the amplitudes are given by (15.31).

To evaluate the performance we computed the MSE in estimating the delays and amplitudes by performing 1000 simulations for each SNR value and for different numbers of Cadzow iterations, denoted by J . One of the drawbacks of Cadzow's algorithm is that in some cases it leads to missed detections: two of the zeros become identical so that one (or more) of the delays is completely missed. In calculating the error, missed detections were not taken into account. Thus, we chose 1000 simulations in which no missed detections occurred.

We begin by considering $L = 6$ delays and $m = 81$ samples. Note that as explained in Example 15.2, this corresponds to taking samples at the Nyquist rate of $x(t)$. In Fig. 15.6 we plot the MSE (in log scale) in estimating the delays and amplitudes as a function of the SNR for different numbers of Cadzow iterations: $J = 0, 10, 1000$. Choosing $J = 0$ results in Prony's method. The figure illustrates that even a small number of Cadzow iterations produces a significant improvement in MSE. It can also be observed that for high enough SNR, proper estimation of the delays and amplitudes is attainable. On the other hand, Prony's method combined with TLS without performing Cadzow denoising is unreliable. In comparison with Fig. 15.5(c) and (d), we see that the Cadzow algorithm is more effective than the MF, even at the Nyquist rate.

When we increase the number of delays, the MSE deteriorates. Figure 15.7 shows the performance with $L = 12$. Although good performance can still be achieved,

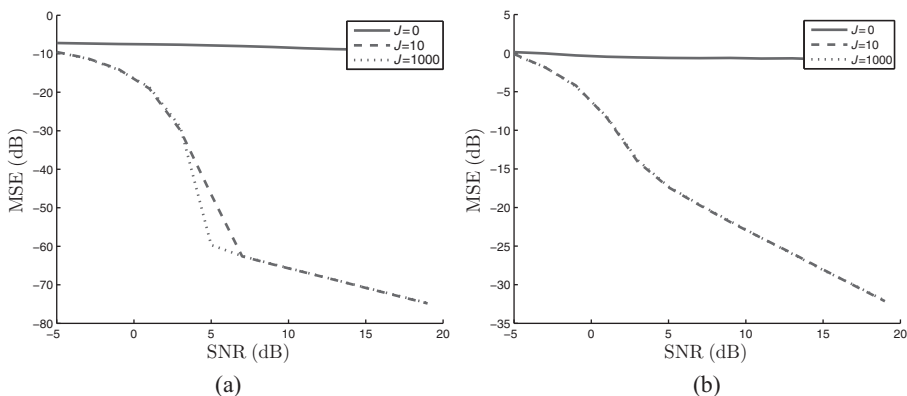


Figure 15.6 Delay and amplitude estimation using Cazdow denoising for $L = 6$ delays and $m = 81$ samples. (a) MSE in estimating the delays. (b) MSE in estimating the amplitudes.

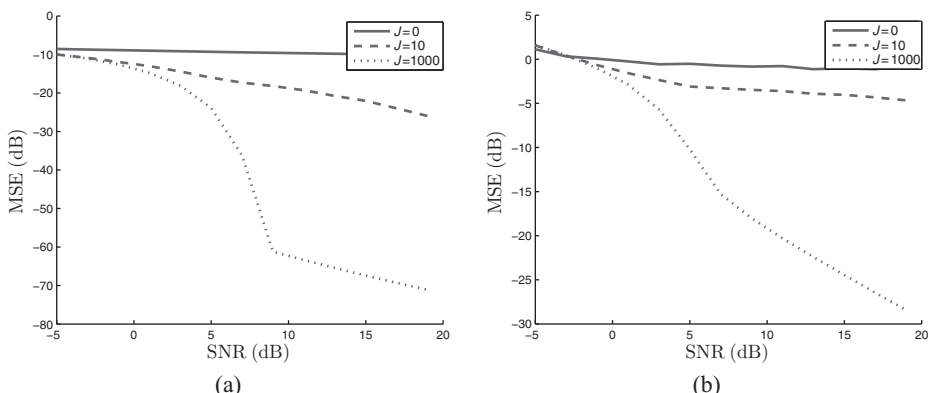


Figure 15.7 Delay and amplitude estimation using Cadzow denoising for $L = 12$ delays and $m = 81$ samples. (a) MSE in estimating the delays. (b) MSE in estimating the amplitudes.

it requires increasing the number of Cadzow iterations markedly. In Fig. 15.8 we plot the performance for different values of L , using 1000 Cadzow iterations. As the number of delays increases, the performance of Cadzow denoising worsens.

The main drawback of using a large number of Cadzow iterations is the missed detection (MD) rate. To illustrate this, we calculated the number of MDs in the simulations performed above, and plotted the MD rate in Fig. 15.9 as a function of SNR. The rate was calculated as the number of iterations with MDs divided by the total number of iterations.

To conclude, we introduced Prony's method and its extensions to the noisy setting (TLS and Cadzow denoising). These are two-step approaches for evaluating the frequencies ω_ℓ in (15.26), or zeros u_ℓ in (15.32): first, we seek the coefficients of the annihilating filter, and then we find roots of a polynomial. These techniques are therefore also referred to as *polynomial methods*. A drawback of this approach is that finding the

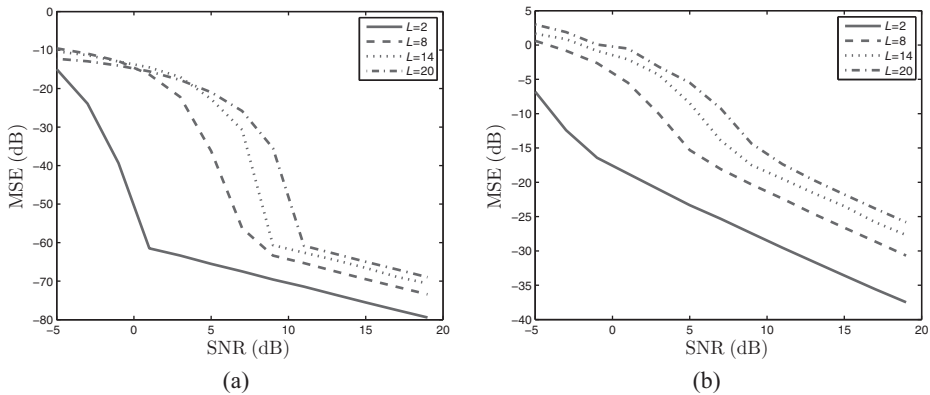


Figure 15.8 Delay and amplitude estimation using 1000 Cadzow iterations for varying values of L and $m = 81$ samples. (a) MSE in estimating the delays. (b) MSE in estimating the amplitudes.

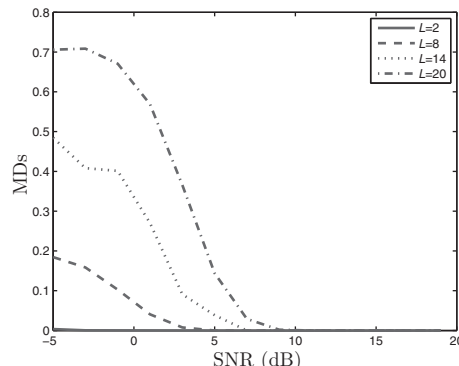


Figure 15.9 Missed detection rates for different number of delays.

roots of a polynomial becomes difficult for large values of L and tends to be sensitive to noise. Alternative algorithms that do not require polynomial rooting include matrix pencil and subspace methods which we discuss next.

15.2.5 Matrix pencil

Matrix pencil algorithm

The matrix pencil [445, 446] algorithm is a one-step process of solving a generalized eigenvalue problem that directly yields the values u_ℓ . This approach is not only more computationally efficient, but it can be shown to lead to better statistical properties than polynomial based techniques.

We begin by constructing a data matrix $\mathbf{Y}_{(m-M) \times (M+1)}$ from the m measurements where

$$L \leq M \leq m - L \quad (15.51)$$

is the *pencil parameter* and is very useful in eliminating noise in the data as we show below. (In Prony's method and its extensions M was set equal to the number of exponents L .) The condition on M will be made clear in Proposition 15.4. In particular, it implies that we must have $m \geq 2L$. We next create two matrices \mathbf{Y}_1 and \mathbf{Y}_2 of size $m - M \times M$ by choosing the first and last M columns of $\mathbf{Y}_{(m-M) \times (M+1)}$ respectively. Writing out the matrices explicitly, we have

$$\mathbf{Y}_1 = \begin{pmatrix} Y[0] & Y[1] & \cdots & Y[M-1] \\ Y[1] & Y[2] & \cdots & Y[M] \\ \vdots & \vdots & \ddots & \vdots \\ Y[m-M-1] & Y[m-M] & \cdots & Y[m-2] \end{pmatrix},$$

$$\mathbf{Y}_2 = \begin{pmatrix} Y[1] & Y[2] & \cdots & Y[M] \\ Y[2] & Y[3] & \cdots & Y[M+1] \\ \vdots & \vdots & \ddots & \vdots \\ Y[m-M] & Y[m-M+1] & \cdots & Y[m-1] \end{pmatrix}. \quad (15.52)$$

Note that the k th element of \mathbf{Y}_i is given by

$$\mathbf{Y}_i(k, n) = Y[k + n + i - 1], \quad k = 0, \dots, m - M - 1 \text{ and } n = 0, \dots, M - 1. \quad (15.53)$$

The matrix pencil approach exploits the fact that the data matrices \mathbf{Y}_i have a simple decomposition in terms of the Vandermonde matrices $\mathbf{V}(\{\omega_\ell\})_{m-M \times L}$ of (15.30):

Proposition 15.3. *Let $Y[k]$ satisfy (15.26). Then the matrices $\mathbf{Y}_1, \mathbf{Y}_2$ defined by (15.52) can be written as*

$$\mathbf{Y}_1 = \mathbf{V}(\{\omega_\ell\})_{m-M \times L} \operatorname{diag}(\mathbf{a}) \mathbf{V}^T(\{\omega_\ell\})_{M \times L}$$

$$\mathbf{Y}_2 = \mathbf{V}(\{\omega_\ell\})_{m-M \times L} \operatorname{diag}(\mathbf{a}) \operatorname{diag}(\mathbf{u}) \mathbf{V}^T(\{\omega_\ell\})_{M \times L}, \quad (15.54)$$

where \mathbf{a} is the length- L vector of coefficients a_ℓ , and \mathbf{u} is the length- L vector with elements $u_\ell = e^{-j\omega_\ell}$.

Proof: The result for \mathbf{Y}_1 follows immediately from Proposition 15.2. To prove the result for \mathbf{Y}_2 , let $\mathbf{C} = \mathbf{V}(\{\omega_\ell\})_{m-M \times L} \operatorname{diag}(\mathbf{a}) \operatorname{diag}(\mathbf{u}) \mathbf{V}^T(\{\omega_\ell\})_{M \times L}$. Using (15.40) we can write

$$\mathbf{C} = \sum_{\ell=1}^L a_\ell u_\ell \mathbf{e}(\omega_\ell)_{m-M} \mathbf{e}^T(\omega_\ell)_M, \quad (15.55)$$

where $\mathbf{e}(\omega_\ell)_s$ is defined by (15.42). Therefore, the k th value of \mathbf{C} for $k = 0, \dots, m - M - 1$ and $n = 0, \dots, M - 1$ is equal to

$$c_{kn} = \sum_{\ell=1}^L a_\ell u_\ell u_\ell^k u_\ell^n = \sum_{\ell=1}^L a_\ell u_\ell^{k+n+1} = Y[k + n + 1], \quad (15.56)$$

where we applied (15.26). From (15.53), $\mathbf{C} = \mathbf{Y}_2$. □

Based on Proposition 15.3 we consider the matrix pencil

$$\mathbf{Q}(\lambda) = \mathbf{Y}_2 - \lambda \mathbf{Y}_1 = \mathbf{V}(\{\omega_\ell\})_{m-M \times L} \text{diag}(\mathbf{a})(\text{diag}(\mathbf{u}) - \lambda \mathbf{I}) \mathbf{V}^T(\{\omega_\ell\})_{M \times L}. \quad (15.57)$$

In Proposition 15.4 below we show that when λ is equal to one of the roots u_ℓ , $\mathbf{Q}(\lambda)$ loses rank. This property can be used to efficiently find the values of u_ℓ by a generalized eigendecomposition.

Proposition 15.4. *Let $\mathbf{Q}(\lambda)$ be the matrix pencil defined by (15.57) with $\mathbf{Y}_1, \mathbf{Y}_2$ given by (15.52), and let $L \leq M \leq m - L$. Define $r = \text{rank}(\mathbf{Q}(\lambda))$. Then*

- If $\lambda \neq u_\ell$ then $r = L$;
- If $\lambda = u_\ell$ for some ℓ then $r = L - 1$.

In addition, if $\mathbf{Q}(\lambda)\mathbf{x} = \mathbf{0}$ for a nonzero vector \mathbf{x} in $\mathcal{N}(\mathbf{Y}_2)^\perp$, then $\lambda = u_\ell$ for some ℓ .

Proof: The proof of the proposition is similar to that of Proposition 15.2. Specifically, using Proposition 15.1 we conclude that $\mathbf{V}(\{\omega_\ell\})_{m-M \times L}$ has rank L (since $m - M \geq L$) and $\mathbf{V}^T(\{\omega_\ell\})_{M \times L}$ has rank L (since $M \geq L$).

Denote $\mathbf{Z}(\lambda) = \text{diag}(\mathbf{a})(\text{diag}(\mathbf{u}) - \lambda \mathbf{I})$. Since $\mathbf{Z}(\lambda)$ is an $L \times L$ diagonal matrix and $a_\ell \neq 0$, its rank is equal to L for $\lambda \neq u_\ell$, and $L - 1$ for $\lambda = u_\ell$. From Lemma 15.1 (see the proof of Proposition 15.2) it follows immediately that the rank of $\mathbf{Q}(\lambda)$ is equal to that of $\mathbf{Z}(\lambda)$.

Finally, from the decomposition (15.54) of \mathbf{Y}_2 and the fact that $\mathbf{V}(\{\omega_\ell\})_{m-M \times L}$ has full column-rank, we conclude that $\mathcal{N}(\mathbf{Y}_2) = \mathcal{N}(\mathbf{V}^T(\{\omega_\ell\})_{M \times L})$. Suppose that \mathbf{x} is a nonzero vector in $\mathcal{N}(\mathbf{Y}_2)^\perp$. Then, $\mathbf{z} = \mathbf{V}^T(\{\omega_\ell\})_{M \times L} \mathbf{x} \neq \mathbf{0}$ so that $\mathbf{Q}(\lambda)\mathbf{x} = \mathbf{0}$ only if $\mathbf{Z}(\lambda)\mathbf{z} = \mathbf{0}$. This can only happen if \mathbf{Z} does not have full rank, so that $\lambda = u_\ell$ for some ℓ . \square

Note that from the proof of the proposition condition (15.51) on M is needed in order to ensure that $\mathbf{Q}(\lambda)$ has rank L for all $\lambda \neq u_\ell$.

Proposition 15.4 can be used to establish that the values of u_ℓ are simply the nonzero eigenvalues of $\mathbf{C} = \mathbf{Y}_1^\dagger \mathbf{Y}_2$.

Corollary 15.2. *Let \mathbf{C} be the $M \times M$ matrix defined by $\mathbf{C} = \mathbf{Y}_1^\dagger \mathbf{Y}_2$. Then the M eigenvalues of \mathbf{C} are equal to $\lambda_\ell = u_\ell$ for $\ell = 1, \dots, L$ and $\lambda_\ell = 0$ for $\ell = L + 1, \dots, M$.*

Proof: From (15.54), $\mathcal{R}(\mathbf{Y}_1) = \mathcal{R}(\mathbf{Y}_2)$ and $\dim(\mathcal{N}(\mathbf{Y}_2)) = M - L$. Since $\mathcal{N}(\mathbf{Y}_1^\dagger) = \mathcal{R}(\mathbf{Y}_1)^\perp = \mathcal{R}(\mathbf{Y}_2)^\perp$, we conclude that $\mathcal{N}(\mathbf{C}) = \mathcal{N}(\mathbf{Y}_2)$. Indeed, for any $\mathbf{x} \in \mathcal{N}(\mathbf{Y}_2)^\perp$, the nonzero vector $\mathbf{Y}_2 \mathbf{x}$ is in $\mathcal{R}(\mathbf{Y}_2) = \mathcal{N}(\mathbf{Y}_1^\dagger)^\perp$ and consequently $\mathbf{C}\mathbf{x} \neq \mathbf{0}$. We conclude that $\mathcal{N}(\mathbf{C})$ has dimension $M - L$ so that \mathbf{C} has $M - L$ eigenvalues equal to 0.

Consider now an eigenvector of \mathbf{C} corresponding to a nonzero eigenvalue λ such that $\mathbf{C}\mathbf{x} = \lambda\mathbf{x}$ with $\mathbf{x} \in \mathcal{N}(\mathbf{C})^\perp = \mathcal{N}(\mathbf{Y}_2)^\perp$. This then implies that

$$\mathbf{Y}_1^\dagger \mathbf{Y}_2 \mathbf{x} = \lambda \mathbf{x}. \quad (15.58)$$

Multiplying the equation on both sides by \mathbf{Y}_1 we have

$$\mathbf{Y}_1 \mathbf{Y}_1^\dagger \mathbf{Y}_2 \mathbf{x} = \lambda \mathbf{Y}_1 \mathbf{x}. \quad (15.59)$$

Algorithm 15.4 Matrix pencil

Input: $m \geq 2L$ measurements $Y[k], k = 0, \dots, m - 1$, number of delays L

Output: Time delays $t_\ell, \ell = 1, \dots, L$

Build the measurement matrix $\mathbf{Y}_{(m-M) \times (M+1)}$ of (15.37) for $L \leq M \leq m - L$

Construct the matrices \mathbf{Y}_1 and \mathbf{Y}_2 as the first and last M columns of \mathbf{Y} respectively

Compute the L nonzero eigenvalues $\{u_\ell\}$ of $\mathbf{C} = \mathbf{Y}_1^\dagger \mathbf{Y}_2$

Determine t_ℓ via $u_\ell = e^{-j\omega_\ell}$ and $\omega_\ell = 2\pi t_\ell / \tau$

Noting that $\mathbf{Y}_1 \mathbf{Y}_1^\dagger = P_{\mathcal{R}(\mathbf{Y}_1)} = P_{\mathcal{R}(\mathbf{Y}_2)}$ it follows that $\mathbf{Y}_1 \mathbf{Y}_1^\dagger \mathbf{Y}_2 = \mathbf{Y}_2$. Therefore, (15.59) can be written as

$$(\mathbf{Y}_2 - \lambda \mathbf{Y}_1) \mathbf{x} = \mathbf{Q}(\lambda) \mathbf{x} = \mathbf{0}. \quad (15.60)$$

Since $\mathbf{x} \in \mathcal{N}(\mathbf{Y}_2)^\perp$ it follows from Proposition 15.4 that (15.60) has a nonzero solution \mathbf{x} only if $\lambda = u_\ell$. \square

The matrix pencil method is summarized in Algorithm 15.4. When the data are noisy we can first apply the Cadzow denoising approach to $\mathbf{Y}_{(m-M) \times (M+1)}$ of (15.37) and then use the denoised matrix to construct \mathbf{Y}_1 and \mathbf{Y}_2 by taking the appropriate columns. For efficient noise filtering, it has been observed empirically that a good choice of M is $m/3 \leq M \leq m/2$.

Example 15.4 We now evaluate the performance of matrix pencil and compare it with Prony's method using the same setting as Example 15.3.

In Fig. 15.10, we plot the MSE (in log scale) as a function of SNR for different choices of the pencil parameter M , where the results are averaged over 4000 simulations. We choose $L = 6$ delays and $m = 81$ samples. In each simulation the matrices \mathbf{Y}_1 and \mathbf{Y}_2 are calculated and denoised by taking only the L largest entries in their SVD. The values of $\{u_\ell\}_{\ell=1}^L$ are determined by the L largest eigenvalues of $\mathbf{C} = \mathbf{Y}_1^\dagger \mathbf{Y}_2$. Finally the amplitudes are given by (15.31). The figure illustrates the importance of choosing M correctly. A popular rule of thumb is to select M approximately in the range $m/3 \leq M \leq m/2$, which is consistent with the results in the figure.

We next compare matrix pencil to Prony's method (where in order to prevent missed detections no Cadzow iterations are performed) for $M = 35$, $L = 12$ and $m = 81$. The results can be seen in Fig. 15.11 from which it is clear that the matrix pencil approach achieves much lower MSE in comparison with Prony's algorithm. Comparing with Fig. 15.7, at high SNR matrix pencil outperforms Cadzow denoising followed by Prony, and does not result in missed detections.

Unknown number of delays

Until now we have assumed that the number of delays L is known. When L is unknown in advance, its value can be estimated using the matrix pencil approach by considering the singular values of $\mathbf{Y} = \mathbf{Y}_{(m-M) \times (M+1)}$ or equivalently by examining the

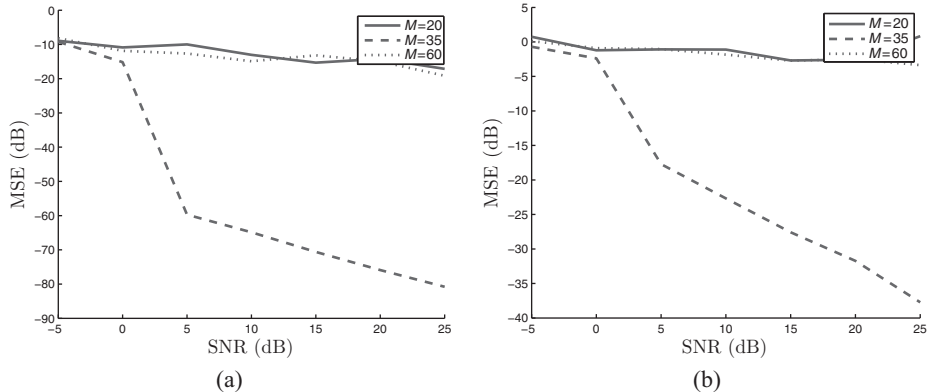


Figure 15.10 Delay and amplitude estimation using matrix pencil for $L = 6$ delays and $m = 81$ samples for various values of the pencil parameter M . (a) MSE in estimating the delays. (b) MSE in estimating the amplitudes.

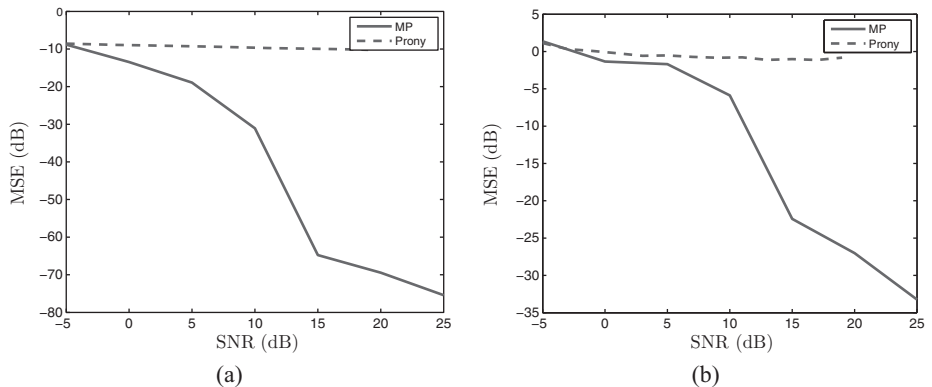


Figure 15.11 Delay and amplitude estimation using Prony's method and matrix pencil with pencil parameter $M = 35$ for $L = 12$ delays and $m = 81$ samples. (a) MSE in estimating the delays. (b) MSE in estimating the amplitudes.

eigenvalues of $\mathbf{C} = \mathbf{Y}_1^\dagger \mathbf{Y}_2$. As we have seen in Corollary 15.2, \mathbf{C} should consist of L nonzero eigenvalues. In the presence of noise, these L values will be noisy, and in addition the other $M - L$ zero eigenvalues will contain noise as well. Assuming that the noise is smaller than the signal, we choose L as the number of singular values that are beyond a threshold. The remaining singular values are assumed to be due to noise and are therefore set to zero.

Example 15.5 Suppose that number of delays L is unknown. We illustrate some considerations in choosing a proper threshold in order to estimate its value from the eigenvalues of \mathbf{C} defined in Corollary 15.2.

We again choose $x(t)$ to be the same as in Example 15.2: $x(t) = \sum_{\ell=1}^L \sum_{n \in \mathbb{Z}} a_\ell h(t - t_\ell - n\tau)$ along the period $\tau = 1$ where $a_\ell = 1, t_\ell = \ell\Delta$ for a chosen Δ . The samples are corrupted by noise (in the frequency domain) so that we are given $m \geq$

$2L$ noisy measurements of the coefficients $Y[k], k \in \mathcal{K}$ where \mathcal{K} is a consecutive index set of size m . The noise is complex white Gaussian with variance chosen to match the required SNR. When no information about L is available, the only choice of pencil parameter M satisfying (15.51) for any $L \leq m/2$ is $M = m/2$. We therefore use this value throughout the simulations.

In each simulation the eigenvalues of $\mathbf{C} = \mathbf{Y}_1^\dagger \mathbf{Y}_2$ are sorted according to their absolute values, and then normalized by the largest eigenvalue. We denote the normalized and sorted absolute eigenvalues by $\lambda_\ell \geq 0$. From Corollary 15.2, in the absence of noise, \mathbf{C} should have L nonzero eigenvalues and $M - L$ zero eigenvalues. When noise is present in the measurements we expect to have L larger eigenvalues due to the delayed pulses and $M - L$ smaller eigenvalues corresponding to noise.

In order to set a proper threshold we examine the probability density function (pdf) of the smallest absolute eigenvalue due to the delayed pulses, λ_L , and of the largest absolute eigenvalue caused by the noise, λ_{L+1} . We approximate the pdfs empirically from 100 000 simulations for different number of delays, choices of Δ and SNR levels. The pdfs of λ_L and λ_{L+1} are depicted in Fig. 15.12 (in the figure we see the sum of the pdfs) for $L = 2, \Delta = 0.5$ and two different levels of SNR. These results can be used to set an appropriate threshold, together with any prior information on the desired miss detect or false alarm rates. From the figure, it can be seen that as the SNR decreases the peaks widen so that separating them using a threshold becomes harder.

In Fig. 15.13 we plot the pdfs for $L = 4$, SNR = 10 (dB) and two different values of Δ . Decreasing the distance Δ between pulses results in the same effect of peak widening. Similar behavior occurs when the number of delays increases, as demonstrated in Fig. 15.14. Here we plot the pdfs for SNR = 10 (dB), $\Delta = 0.1$ and three different numbers of delays. When more delays are added, the peaks widen and become closer, leading to a more noticeable tradeoff between false alarms and miss detects.

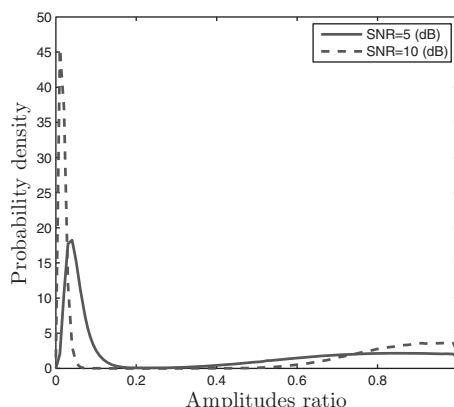


Figure 15.12 Probability density function of λ_2 and λ_3 for two different SNR levels, with $L = 2$ and $\Delta = 0.5$. The left peak corresponds to the pdf of λ_3 , while the right peak is the pdf of λ_2 .

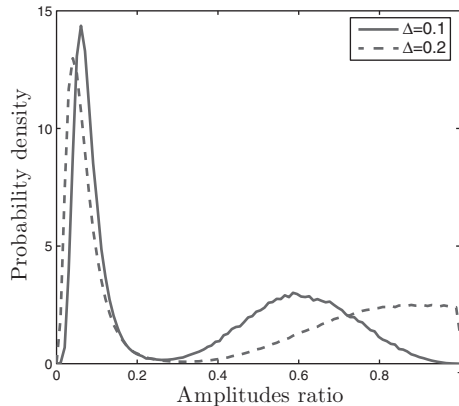


Figure 15.13 Probability density function of λ_4 and λ_5 for two different values of Δ , with $L = 4$ and SNR = 10 dB. The left peak corresponds to the pdf of λ_5 , while the right peak is the pdf of λ_4 .

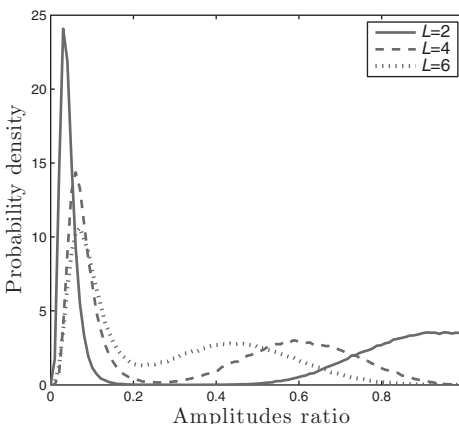


Figure 15.14 Probability density function of λ_L and λ_{L+1} for three different numbers of delays, with $\Delta = 0.1$ and SNR = 10 dB. The left peak corresponds to the pdf of λ_{L+1} , while the right peak is the pdf of λ_L .

15.2.6 Subspace methods

Pisarenko algorithm

Another class of techniques for finding the frequencies in (15.26) is *subspace algorithms*. The first example of this approach is the Pisarenko method [447] which was later generalized to the popular MULTiple SIgnal Classification (MUSIC) algorithm. This class of techniques is based on the fact that any vector in the null space of an appropriate data matrix is orthogonal to the frequency vectors $e(-\omega_\ell)$ defined in (15.42). The desired frequencies can therefore be found by exploiting this subspace orthogonality.

As in the Prony and TLS methods, we first find a vector in the null space of $\mathbf{Y}_{(m-L) \times (L+1)}$. When the data are noisy, this vector, denoted \mathbf{v}_{\min} , is chosen according to the TLS approach as the right-singular vector corresponding to the smallest singular

value of $\mathbf{Y}_{(m-L) \times (L+1)}$. But then, instead of using \mathbf{v}_{\min} to construct the annihilating filter (15.34) and finding its zeros, we build a *pseudospectrum*

$$S(e^{j\omega}) = \frac{1}{|\mathbf{e}^*(-\omega)_{L+1} \mathbf{v}_{\min}|^2} \quad (15.61)$$

where $\mathbf{e}(-\omega)_{L+1}$ is defined in (15.42). The values of ω_ℓ are then chosen by looking for the peaks in $S(e^{j\omega})$.

The motivation behind the Pisarenko algorithm is that any vector in the null space of $\mathbf{Y} = \mathbf{Y}_{(m-L) \times (L+1)}$ is orthogonal to any vector in the range space of \mathbf{Y}^* (since $\mathcal{N}(\mathbf{Y}) = \mathcal{R}(\mathbf{Y}^*)^\perp$). Furthermore, any vector of the form $\mathbf{e}(-\omega_\ell)_{L+1}$ is in the range of \mathbf{Y}^* , as incorporated in the following proposition.

Proposition 15.5. *Let $\mathbf{e}(-\omega)_{M+1}$ be defined by (15.42) and let $\mathbf{Y} = \mathbf{Y}_{(m-M) \times (M+1)}$ be defined by (15.37) for $L \leq M \leq m - L$. Then any vector of the form $\mathbf{e}(-\omega_\ell)_{M+1}$ is in $\mathcal{R}(\mathbf{Y}^*)$ for $m - M \geq L$.*

Proof: From (15.39),

$$\mathbf{Y}_{(m-M) \times (M+1)}^* = \overline{\mathbf{V}(\{\omega_\ell\})_{M+1 \times L} \text{diag}(\mathbf{a}) \mathbf{V}^*(\{\omega_\ell\})_{m-M \times L}}. \quad (15.62)$$

Since $m - M \geq L$, the range of $\mathbf{V}^*(\{\omega_\ell\})_{m-M \times L}$ is equal to \mathbb{C}^L (i.e. $\mathbf{V}^*(\{\omega_\ell\})_{m-M \times L}$ is of full row-rank). Together with the fact that $\text{diag}(\mathbf{a})$ is invertible, this implies that $\mathcal{R}(\mathbf{Y}_{(m-M) \times (M+1)}^*)$ is equal to $\mathcal{R}(\overline{\mathbf{V}(\{\omega_\ell\})_{M+1 \times L}})$. The result then follows from noting that the columns of $\overline{\mathbf{V}(\{\omega_\ell\})_{M+1 \times L}}$ are equal to $\mathbf{e}(-\omega_\ell)_{M+1}$. \square

For noise free data, Proposition 15.5 implies that at $\omega = \omega_\ell$ we will see very strong peaks in the pseudospectrum (15.61). When the data are noisy, the peaks will be less evident, as seen in the following example.

Example 15.6 Consider the pseudospectrum (15.61) using the same settings as in Example 15.2 with delays $t_\ell = \ell\Delta$ and $a_\ell = 1$.

In Fig. 15.15 we plot $S(e^{j\omega})$ for different choices of Δ and varying SNR with $L = 5$. The figure illustrates that decreasing Δ results in erroneous peak locations as well as miss detects. This phenomenon is more pronounced as the SNR decreases. Robustness to noise can be achieved by applying Cadzow denoising on $\mathbf{Y}_{(m-L) \times (L+1)}$ prior to computing its required singular vector, as can be seen in Fig. 15.16. In this example, 100 iterations of Cadzow were taken although in practice, after about 25 iterations, no significant improvement was observed.

MUSIC algorithm

Pisarenko's algorithm can be extended by noting that from Proposition 15.5, $\mathbf{e}(-\omega_\ell)_{M+1}$ is orthogonal to any vector in the null space of $\mathbf{Y} = \mathbf{Y}_{(m-M) \times (M+1)}$ where $L \leq M \leq m - L$. When $M = L$, the null space has dimension equal to 1 leading to Pisarenko's method. However, for larger values of M , the null space dimension grows, and is equal

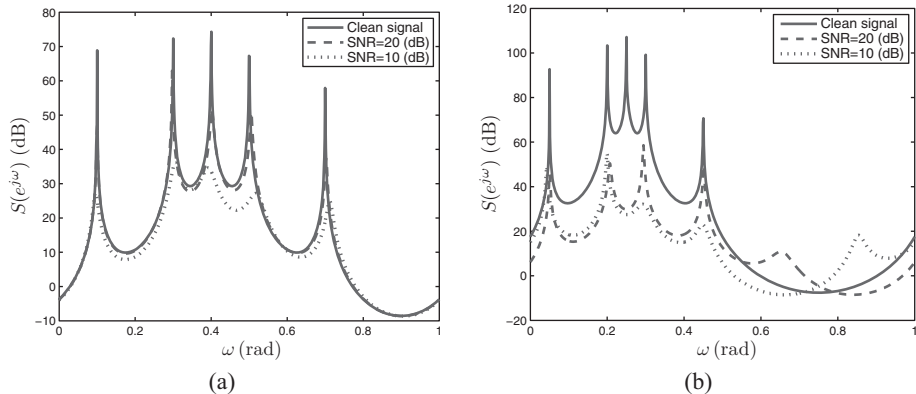


Figure 15.15 Pseudospectrum using Pisarenko’s algorithm for different delays. (a) $\Delta = 0.1$. (b) $\Delta = 0.05$.

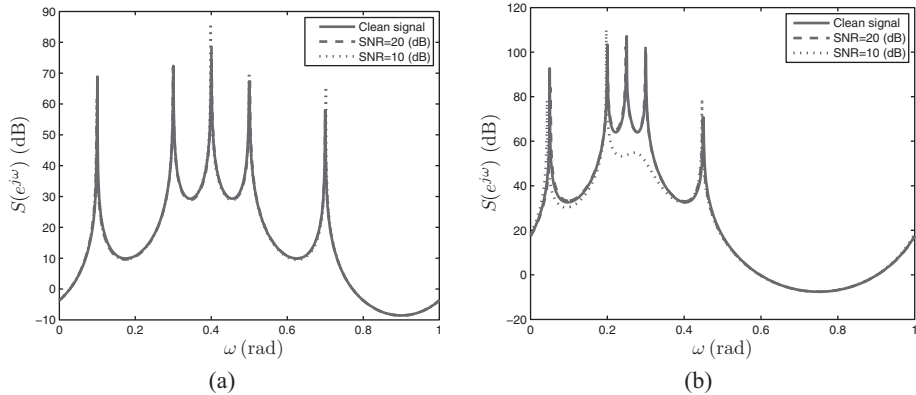


Figure 15.16 Pseudospectrum using Pisarenko’s algorithm combined with Cadzow denoising for different delays. (a) $\Delta = 0.1$. (b) $\Delta = 0.05$.

to $M - L + 1$. Therefore, there are $M - L + 1$ orthonormal vectors in the null space that can be used.

Let $\{\mathbf{v}_i, 1 \leq i \leq M - L + 1\}$ be an orthonormal basis for $\mathcal{N}(\mathbf{Y})$. Then, in the absence of noise,

$$\sum_{i=1}^{M-L+1} |\mathbf{e}^*(-\omega_\ell) \mathbf{v}_i|^2 = 0, \quad \ell = 1, \dots, L. \quad (15.63)$$

When the data are noisy, (15.63) will not be satisfied with equality; however, we still expect the left-hand side to be small. This leads to the *multiple signal classification (MUSIC)* [15] approach in which the values of ω_ℓ are found by searching for the peaks in the pseudospectrum

$$S(e^{j\omega}) = \frac{1}{\sum_{i=1}^{M-L+1} |\mathbf{e}^*(-\omega) \mathbf{v}_{M+1} \mathbf{v}_i|^2}. \quad (15.64)$$

Algorithm 15.5 MUSIC algorithm

Input: $m \geq 2L$ measurements $Y[k], k = 0, \dots, m - 1$, number of delays L

Output: Time delays $t_\ell, \ell = 1, \dots, L$

Build the measurement matrix $\mathbf{Y}_{(m-M) \times (M+1)}$ of (15.37) for $L \leq M \leq m - L$

Compute the SVD of \mathbf{Y} and denote by $\{\mathbf{v}_i\}$ the right singular vectors corresponding to the $M - L + 1$ smallest singular values

Search for the L peaks ω_ℓ in the pseudospectrum $S(e^{j\omega})$ of (15.64) where $e(\omega)$ is defined by (15.42)

Determine t_ℓ via $\omega_\ell = 2\pi t_\ell / \tau$

The vectors $\{\mathbf{v}_i\}$ can be determined by computing the SVD of \mathbf{Y} . Let \mathbf{Y} have an SVD $\mathbf{Y} = \mathbf{U}\Sigma\mathbf{V}^*$, and let $\sigma_i, 1 \leq i \leq M + 1$ denote its sorted singular values. Then the vectors $\{\mathbf{v}_i\}$ are the right-singular vectors corresponding to the $M - L + 1$ smallest singular values. When L is unknown, it can be estimated e.g., as the number of singular values above a threshold.

We summarize the MUSIC approach in Algorithm 15.4. For $M = L$, MUSIC coincides with Pisarenko's method. However, in MUSIC, we average the denominator over all basis vectors in the null space and in that way improve the estimator's performance.

Example 15.7 We compare the MUSIC pseudospectrum (15.64) with that of (15.61) by repeating the setting in Example 15.6.

In Fig. 15.17 we examine the pseudospectrum for different choices of the parameter M and the delay separation Δ with an SNR of 15 (dB) and $L = 5$. The number of samples is equal to 81. As expected, averaging the denominator over all basis vectors in the null space improves the estimator's robustness to noise. Choosing $M = 5$ is equivalent to Pisarenko's method. When M is increased, the performance improves. However, a decrease in Δ still results in erroneous locations and missed detections.

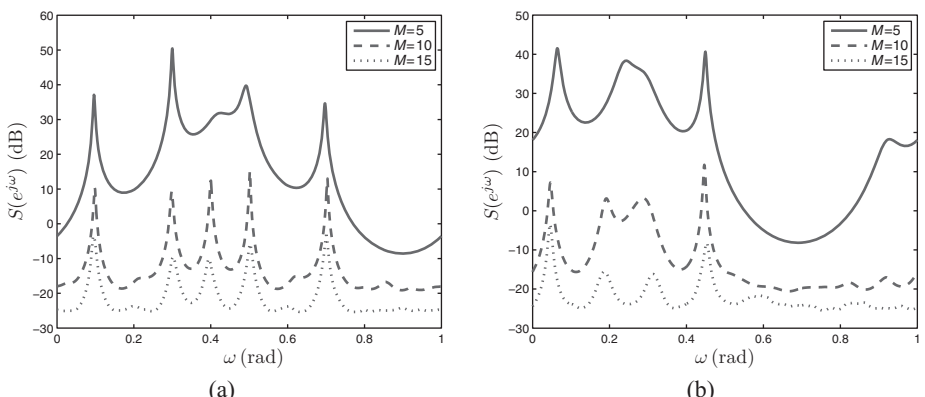


Figure 15.17 Pseudospectrum using MUSIC for varying choices of M and different delays. (a) $\Delta = 0.1$. (b) $\Delta = 0.05$.

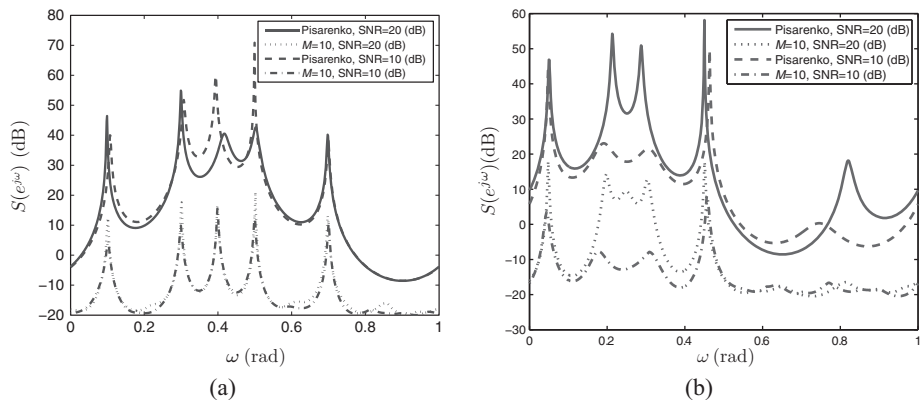


Figure 15.18 Pseudospectrum using Pisarenko and MUSIC for varying choices of SNR and different delays with $M = 10$ in MUSIC. (a) $\Delta = 0.1$. (b) $\Delta = 0.05$.

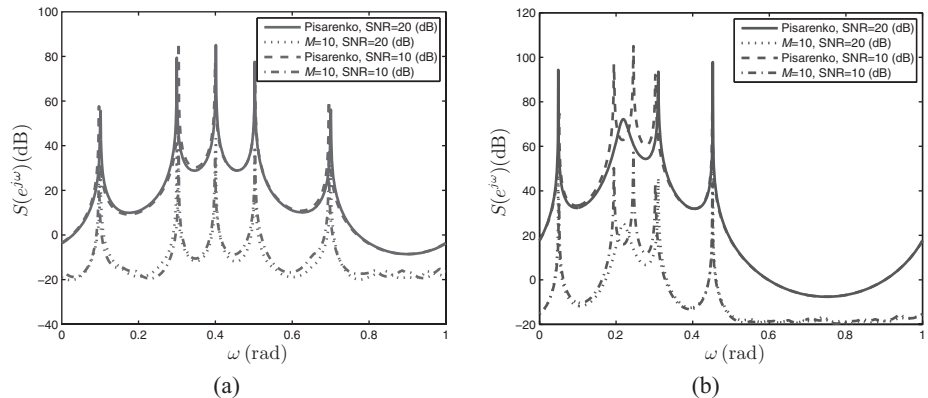


Figure 15.19 Pseudospectrum combined with Cadzow denoising using Pisarenko and MUSIC for varying choices of SNR and different delays with $M = 10$ in MUSIC. (a) $\Delta = 0.1$. (b) $\Delta = 0.05$.

In Fig. 15.18 the pseudospectrum using the Pisarenko and MUSIC algorithms is depicted for different choices of Δ and varying SNR. We set $M = 10$ in computing the MUSIC spectrum. The superiority of MUSIC over Pisarenko's method in low SNR is clearly evident.

Finally, in Fig. 15.19 we repeat the previous simulations where we first apply Cadzow denoising to the data matrix $\mathbf{Y}_{(m-L) \times (L+1)}$. We performed 100 Cadzow iterations, although after the 30th iteration there was no significant improvement. The differences between the Pisarenko and MUSIC spectra are now much less pronounced.

Root-MUSIC algorithm

A popular variation on MUSIC is the *root-MUSIC algorithm* [448]. This method begins as the standard MUSIC technique by constructing the denominator in (15.64). However,

instead of looking for the peaks of its inverse, we express the denominator as a polynomial $D(z)$ of the form:

$$D(z) = \sum_{k=-L}^L b_k z^k, \quad (15.65)$$

and then search for its zeros, which leads to the desired values ω_ℓ .

Note that when $M = L$ root-MUSIC is the same as TLS Prony.

15.2.7 Covariance-based methods

The methods we have reviewed until now directly used the data matrix \mathbf{Y} defined in (15.37) with appropriate dimensions. The same techniques can be applied where we replace the data matrix by a correlation matrix

$$\mathbf{R} = \begin{pmatrix} r[0] & r[1] & \cdots & r[M] \\ r[1] & r[2] & \cdots & r[M+1] \\ \vdots & \vdots & \ddots & \vdots \\ r[m-M-1] & r[m-M] & \cdots & r[m-1] \end{pmatrix}. \quad (15.66)$$

Covariance-based approaches can be derived by assuming that in (15.26), the amplitudes a_ℓ are zero-mean iid random variables with variance σ_ℓ^2 . In this case, the correlation sequence $r[k]$ satisfies a sum-of-sinusoids equation as well. Indeed,

$$r[p] = E \left\{ Y[k] \overline{Y[k-p]} \right\} = \sum_{i=1}^L \sum_{\ell=1}^L E \{ a_\ell \overline{a_i} \} e^{-j\omega_\ell k} e^{j\omega_i(k-p)} = \sum_{\ell=1}^L \sigma_\ell^2 e^{-j\omega_\ell p}, \quad (15.67)$$

which has the same form as (15.26) with new amplitudes σ_ℓ^2 . Here we used the fact that $E \{ a_\ell \overline{a_i} \} = \sigma_\ell^2 \delta_{\ell i}$. Therefore, instead of applying the methods detailed in the previous subsections to \mathbf{Y} of (15.37), we can apply them to the correlation matrix \mathbf{R} with the same dimensions. For example, using the matrix pencil approach with the correlation matrix leads to the well-known *estimation of signal parameters by rotational invariance (ESPRIT)* algorithm [189]. We discuss this method in more detail below.

Stochastic MUSIC

Both MUSIC and ESPRIT can be formulated for more general stochastic models, in which the coefficients $\{a_\ell\}$ do not have to be iid. Specifically, let

$$\mathbf{y} = \mathbf{V}(\{\omega_\ell\})_{m \times L} \mathbf{a} + \mathbf{w}, \quad (15.68)$$

where $\mathbf{V}(\{\omega_\ell\})_{m \times L}$ is the Vandermonde matrix defined by (15.30), \mathbf{a} is a random vector representing the desired signal with zero mean and covariance $\mathbf{R}_a = E\{\mathbf{a}\mathbf{a}^*\}$, and \mathbf{w} is a zero-mean iid noise vector with correlation $\sigma^2 \mathbf{I}$, independent of \mathbf{a} . From (15.68), the covariance of \mathbf{y} is given by:

$$\mathbf{R}_y = \mathbf{V}(\{\omega_\ell\}) \mathbf{R}_a \mathbf{V}^*(\{\omega_\ell\}) + \sigma^2 \mathbf{I}, \quad (15.69)$$

where we have omitted the indices in $\mathbf{V}(\{\omega_\ell\})$. Assuming that $m \geq L$ and that \mathbf{R}_a is invertible, the matrix $\mathbf{T} = \mathbf{V}(\{\omega_\ell\}) \mathbf{R}_a \mathbf{V}^*(\{\omega_\ell\})$ has rank equal to L and its range

space is equivalent to that of $\mathbf{V}(\{\omega_\ell\})$. Therefore, the sorted eigenvalues of \mathbf{T} satisfy $\lambda_\ell > 0, \ell = 1, \dots, L$ and $\lambda_\ell = 0, \ell = L + 1, \dots, m$. The sorted eigenvalues of \mathbf{R}_y are then equal to

$$\lambda'_\ell = \begin{cases} \lambda_\ell + \sigma^2, & \ell = 1, \dots, L \\ \sigma^2, & \ell = L + 1, \dots, m. \end{cases} \quad (15.70)$$

Consider now a matrix \mathbf{U} of size $m \times m - L$ that consists of the eigenvectors of \mathbf{R}_y corresponding to the $m - L$ smallest eigenvalues, with $m \geq L + 1$. These eigenvectors span the *noise space* since they are a result of noise only. Furthermore, they are orthogonal to the *signal space* determined by the range of $\mathbf{V}(\{\omega_\ell\})$. To see this, note that since \mathbf{U} consists of eigenvectors with eigenvalues $\lambda'_\ell, \ell = L + 1, \dots, m$:

$$\mathbf{R}_y \mathbf{U} = \mathbf{U} \operatorname{diag}([\lambda'_{L+1}, \dots, \lambda'_m]) = \sigma^2 \mathbf{U}. \quad (15.71)$$

On the other hand,

$$\mathbf{R}_y \mathbf{U} = \mathbf{V}(\{\omega_\ell\}) \mathbf{R}_a \mathbf{V}^*(\{\omega_\ell\}) \mathbf{U} + \sigma^2 \mathbf{U}, \quad (15.72)$$

from which we conclude that

$$\mathbf{V}(\{\omega_\ell\}) \mathbf{R}_a \mathbf{V}^*(\{\omega_\ell\}) \mathbf{U} = \mathbf{0}. \quad (15.73)$$

Since \mathbf{R}_a is invertible and $\mathbf{V}(\{\omega_\ell\})$ has full column-rank, (15.73) implies that

$$\mathbf{V}^*(\{\omega_\ell\}) \mathbf{U} = \mathbf{0}, \quad (15.74)$$

and \mathbf{U} is orthogonal to the columns of $\mathbf{V}(\{\omega_\ell\})$. Note that (15.74) is identical to (15.63), where now we are considering the eigenvectors of the data covariance rather than the data itself.

As before, we can determine the frequencies ω_ℓ by searching for peaks in the pseudospectrum

$$S(e^{j\omega}) = \frac{1}{\mathbf{e}^*(\omega)_m \mathbf{U} \mathbf{U}^* \mathbf{e}(\omega)_m} \quad (15.75)$$

where $\mathbf{e}(\omega)_m$ is defined in (15.42). Alternatively, we may use root MUSIC and search for roots of the polynomial $\mathbf{e}^*(\omega)_m \mathbf{U} \mathbf{U}^* \mathbf{e}(\omega)_m$.

In practice, the correlation matrix \mathbf{R}_y is estimated from the data, for example by using the sample correlation matrix

$$\mathbf{R}_y = \frac{1}{N} \sum_{i=0}^{N-1} \mathbf{y}_i \mathbf{y}_i^*, \quad (15.76)$$

where N is the number of snapshots available and $\mathbf{y}_i = \mathbf{V}\mathbf{a}_i + \mathbf{w}_i$ with \mathbf{a}_i and \mathbf{w}_i denoting iid realizations of the signal and noise respectively. This approach is summarized in Algorithm 15.6.

ESPRIT algorithm

The ESPRIT algorithm [189] exploits the special structure of the correlation matrix (15.69).

Algorithm 15.6 Stochastic MUSIC

Input: N vectors $\mathbf{y}_i = \mathbf{V}(\{\omega_\ell\})_{m \times L} \mathbf{a}_i + \mathbf{w}_i$ with $m \geq L + 1$; number of delays L
 Output: Time delays $t_\ell, \ell = 1, \dots, L$
 Build the correlation matrix $\mathbf{R}_y = \sum_{i=0}^{N-1} \mathbf{y}_i \mathbf{y}_i^*$
 Perform an eigendecomposition of \mathbf{R}_y and construct the matrix \mathbf{U} consisting of the $m - L$ eigenvectors associated with the smallest eigenvalues in its columns
 Search for the L peaks ω_ℓ in the pseudospectrum $S(e^{j\omega})$ of (15.75) where $e(\omega)$ is defined by (15.42)
 Determine t_ℓ via $\omega_\ell = 2\pi t_\ell / \tau$

From (15.69) it follows that in the absence of noise, the range space of \mathbf{R}_y is identical to that of $\mathbf{V} = \mathbf{V}(\{\omega_\ell\})$. As we noted earlier, this space is referred to as the *signal subspace* and can be determined by choosing the eigenvectors of \mathbf{R}_y corresponding to its L largest eigenvalues. We now show that we can use the structure of \mathbf{V} to extract the desired frequencies from the eigendecomposition of an appropriate matrix constructed from these eigenvectors.

Proposition 15.6. *Let \mathbf{R}_y be the $m \times m$ covariance matrix given by (15.69), and let \mathbf{E} denote the matrix of size $m \times L$ consisting of the eigenvectors corresponding to the L largest eigenvalues of \mathbf{R}_y . Let \mathbf{E}_1 be equal to the first $m - 1$ rows of \mathbf{E} , and let \mathbf{E}_2 be equal to the last $m - 1$ rows of \mathbf{E} . We assume that $m \geq L + 1$. Then the eigenvalues of $\mathbf{E}_1^\dagger \mathbf{E}_2$ are equal to $\lambda_\ell = u_\ell = e^{-j\omega_\ell}$.*

Proof: Let \mathbf{V}_1 be the $m - 1 \times L$ matrix equal to the first $m - 1$ rows of $\mathbf{V} = \mathbf{V}(\{\omega_\ell\})$, and let \mathbf{V}_2 be the $m - 1 \times L$ matrix equal to the last $m - 1$ rows of \mathbf{V} . From the structure of \mathbf{V} ,

$$\mathbf{V}_2 = \mathbf{V}_1 \operatorname{diag}(\mathbf{u}), \quad (15.77)$$

where \mathbf{u} is the length- L vector with elements $u_\ell = e^{-j\omega_\ell}$. Since the matrices \mathbf{V} and \mathbf{E} span the same space, there exists an invertible $L \times L$ matrix \mathbf{T} such that

$$\mathbf{V} = \mathbf{E}\mathbf{T}. \quad (15.78)$$

By deleting the last row in (15.78) we have

$$\mathbf{V}_1 = \mathbf{E}_1 \mathbf{T}. \quad (15.79)$$

Similarly, deleting the first row in (15.78) and using the rotational invariance property (15.77), we have

$$\mathbf{V}_1 \operatorname{diag}(\mathbf{u}) = \mathbf{E}_2 \mathbf{T}. \quad (15.80)$$

Combining (15.79) and (15.80) leads to the following relation between the matrices \mathbf{E}_1 and \mathbf{E}_2 :

$$\mathbf{E}_2 = \mathbf{E}_1 \mathbf{T} \operatorname{diag}(\mathbf{u}) \mathbf{T}^{-1}. \quad (15.81)$$

Algorithm 15.7 ESPRIT algorithm

Input: N vectors $\mathbf{y}_i = \mathbf{V}(\{\omega_\ell\})_{m \times L} \mathbf{a}_i + \mathbf{w}_i$ with $m \geq L + 1$; number of delays L
 Output: Time delays $t_\ell, \ell = 1, \dots, L$
 Build the correlation matrix $\mathbf{R}_y = \sum_{i=0}^{N-1} \mathbf{y}_i \mathbf{y}_i^*$
 Perform an eigendecomposition of \mathbf{R}_y and construct the matrix \mathbf{E} consisting of the L eigenvectors associated with the largest eigenvalues in its columns
 Compute the matrix $\mathbf{C} = \mathbf{E}_1^\dagger \mathbf{E}_2$ where \mathbf{E}_1 and \mathbf{E}_2 consist of the first and last $m - 1$ rows of \mathbf{E} respectively
 Compute the L eigenvalues $\lambda_\ell = u_\ell$ of \mathbf{C}
 Determine t_ℓ via $u_\ell = e^{-j\omega_\ell}$ and $\omega_\ell = 2\pi t_\ell / \tau$

The matrix \mathbf{E}_1 is an $m - 1 \times L$ matrix with full column-rank ($m - 1 \geq L$ by our assumption on m). Therefore, $\mathbf{E}_1^\dagger \mathbf{E}_1 = \mathbf{I}$. Multiplying (15.81) on the left by \mathbf{E}_1^\dagger leads to

$$\mathbf{E}_1^\dagger \mathbf{E}_2 = \mathbf{T} \operatorname{diag}(\mathbf{u}) \mathbf{T}^{-1}. \quad (15.82)$$

From (15.82), the eigenvalues of $\mathbf{E}_1^\dagger \mathbf{E}_2$ are $\lambda_\ell = u_\ell$, completing the proof. \square

In practice, \mathbf{R}_y is estimated from the given measurements, as in the MUSIC method. The resulting ESPRIT algorithm is summarized in Algorithm 15.7.

We note that in both MUSIC and ESPRIT we assumed that the correlation matrix \mathbf{R}_a is invertible. In practice, this requirement can be relaxed by performing an additional spatial smoothing stage before applying the algorithms. For details, the reader is referred to [449].

In summary, MUSIC and ESPRIT are subspace methods, which are based on separating the space containing the measurements into signal and noise subspaces. Estimating the unknown set of parameters using MUSIC involves a continuous one-dimensional search over the parameter range. The ESPRIT approach estimates the parameters by solving an eigendecomposition problem and exploiting the structure of the correlation matrices.

15.2.8 Compressed sensing formulation

The deterministic methods we have reviewed until now assumed we are given consecutive values of $Y[k]$ in (15.26). In turn, they allowed for recovery of the frequencies ω_ℓ on a continuous grid (in the noise-free setting). As the noise increases, estimating ω_ℓ becomes more difficult so that in practice it can only be found up to a certain error, limiting the resulting resolution. CS offers an alternative approach to recovery of ω_ℓ . On the one hand, it requires discretizing the possible frequency values. On the other hand, CS-based methods do not require consecutive Fourier measurements, and are often more robust to noise especially when the noise is large.

To formulate (15.26) within the CS framework, we begin by quantizing the analog time axis with a resolution step of Δ , so that $t_\ell = s_\ell \Delta$ for some integer value s_ℓ . We then approximate (15.26) as

$$Y[k] \approx \sum_{\ell=1}^L a_\ell e^{-j \frac{2\pi}{\tau} k s_\ell \Delta}, \quad s_\ell = 0, 1, \dots, N-1, \quad (15.83)$$

where we recall that $\omega_\ell = 2\pi t_\ell / \tau$, and $N = \tau / \Delta$ is the number of possible time steps in the period τ . For simplicity, we assume that N is an integer. Selecting a finite subset of m measurements, namely, choosing k from $\mathcal{K} = \{k_1, k_2, \dots, k_m\} \subset \mathbb{Z}$, (15.83) may be written as

$$\mathbf{y} = \mathbf{Ax}, \quad (15.84)$$

where \mathbf{A} is an $m \times N$ matrix, formed by taking the set \mathcal{K} of rows from a scaled $N \times N$ Fourier matrix, and \mathbf{x} is an L -sparse vector with nonzero entries $\{a_\ell\}$ at indices $\{s_\ell\}$. CS-based techniques allow flexibility in choosing the Fourier coefficients, or the set \mathcal{K} .

Our goal is to find the nonzero entries of \mathbf{x} from the measurements \mathbf{y} . This is a standard CS problem, with \mathbf{A} being a partial Fourier matrix. Therefore, any of the methods for CS recovery detailed in Chapter 11 can be used to determine \mathbf{x} . Note that the properties of the matrix \mathbf{A} are affected by two main variables: the grid resolution manifested in the number of columns N , and the choice of frequencies which affects which rows of the Fourier matrix are used.

From the results of Chapter 11 we know that high recovery performance of CS algorithms is guaranteed, provided that the sensing matrix \mathbf{A} satisfies desired properties such as the coherence or RIP. These values are affected both by the number of columns N , and by the choice of frequency set \mathcal{K} . Selecting the frequency samples uniformly at random, it is known that if $m \geq CL(\log N)^4$, for some positive constant C , then \mathbf{A} obeys the RIP with high probability (See Section 11.3.5). Since N is determined by the chosen grid resolution, trying to obtain higher resolution by using a fine grid leads to an increase in the number of measurements needed to obtain good recovery. For consecutive frequency selection the RIP is not generally satisfied, unless the cardinality of \mathcal{K} is significantly increased.

These tradeoffs can also be seen through the coherence of the columns of \mathbf{A} . Recall from Chapter 11 that low coherence ensures high recovery probability. In Fig. 15.20 we

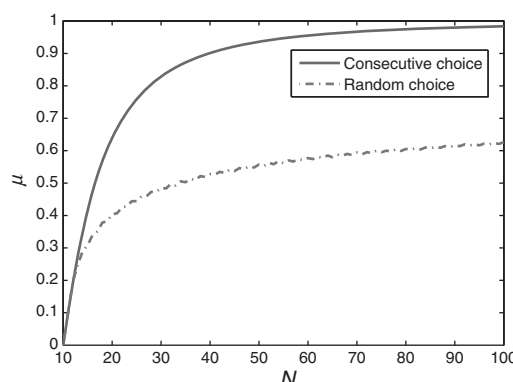


Figure 15.20 Coherence of the matrix \mathbf{A} in (15.84) as a function of N .

plot the coherence of \mathbf{A} as a function of the length N of \mathbf{x} (which determines the resolution), where the coherence is defined as $\mu(\mathbf{A}) = \max_{i \neq j} |\langle \mathbf{a}_i, \mathbf{a}_j \rangle| / (\|\mathbf{a}_i\| \|\mathbf{a}_j\|)$. The coherence is plotted for two selections of the set \mathcal{K} : A consecutive set of $m = 10$ values, and random selection of m frequency values from $[0, N - 1]$. In the latter case we plot the average coherence over 1000 random choices. The figure illustrates two important aspects of CS recovery in our context. The first is that spreading out the frequency values leads to lower coherence and therefore to improved recovery performance. The second is that as the time resolution increases for a fixed number of samples, the coherence increases, which degrades performance.

Unfortunately, applying random frequency sampling is not always realistic from a hardware perspective. In Section 15.4 we discuss practical methods for choosing the desired frequency values in combination with CS recovery.

In Examples 15.8 and 15.9 below we examine the performance of CS in several settings, and compare the MSE in delay estimation with that resulting from matrix pencil. As expected, we will see that CS with spread-out frequency values is more robust to noise, and is therefore preferable in the low SNR regime. This will also be demonstrated in Example 15.15. However, owing to discretization and the coherence of the matrix columns, obtaining high-resolution requires many samples. Thus, in the high SNR regime, matrix pencil is preferable to CS, especially when the number of measurements is small.

There are several more recent approaches to frequency estimation based on convex optimization techniques that do not require discretization and offer improved performance over both CS and matrix pencil type algorithms. The tradeoff is that they are computationally more intensive. The interested reader is referred to [450, 451] and the references therein.

15.2.9 Sub-Nyquist sampling

Until now we have assumed that the number of samples in time, or the number of frequency values in the set \mathcal{K} , was chosen equal to that obtained when sampling at the Nyquist rate. In the following examples we illustrate the use of MF, matrix pencil and CS with a number of Fourier coefficients m that is smaller than that corresponding to the Nyquist rate. As we will see, while the performance of the MF deteriorates significantly with small values of m , the behavior of matrix pencil is not heavily influenced by the number of measurements, as long as $m \geq 2L$. CS also leads to good performance as long as m is large enough and the frequency values in \mathcal{K} are properly spread. This shows the value of frequency-based methods in the presence of subsampling. In Sections 15.3 and 15.4 we will discuss how to obtain the desired Fourier coefficients directly from low-rate samples of $x(t)$.

Example 15.8 Consider the setting of Example 15.2, used in previous examples as well. The waveform $h(t)$ has bandwidth equal to 81 Hz so that sampling at the Nyquist rate results in $m = 81$ samples. We compare the performance achieved

using $m = 36$ and 81 samples where in the MF we use local interpolation. In matrix pencil, the pencil parameter is chosen at the middle of the recommended range $m/3 \leq M \leq m/2$ so that $M = 15, 35$ for $m = 36, 81$ respectively. We used the OMP algorithm (Algorithm 11.1) for CS recovery, and consider two choices of the frequency set \mathcal{K} : a consecutive choice and a random choice where the m frequencies are chosen uniformly at random in the range $[0, 10m]$. The grid in time was chosen to have a resolution of $1/10\,000$, i.e. we used $10\,000$ points over the interval $[0, 1]$. The results were averaged over 1000 simulations (for fixed frequency set in the case of random \mathcal{K}).

In Fig. 15.21 we plot the MSE (in log scale) as a function of SNR using matrix pencil and MF for $L = 6$. We compare matrix pencil and CS under the same settings in Figs. 15.22 and 15.23. In Fig. 15.22 we sample consecutive frequency values, while the CS results in Fig. 15.23 are based on random frequency locations.

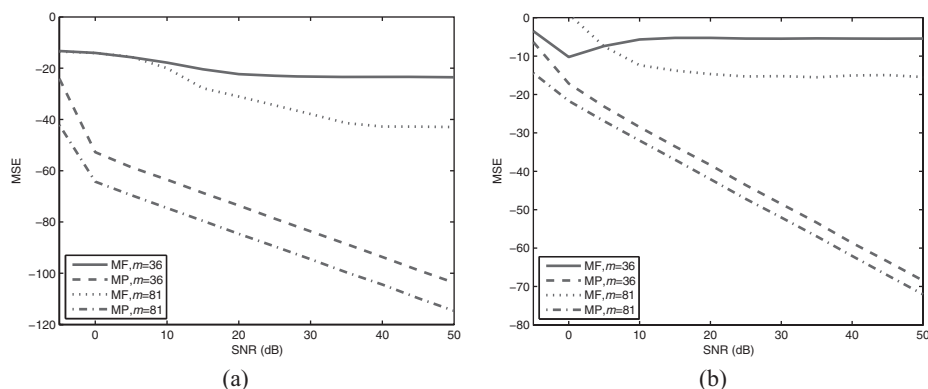


Figure 15.21 Delay and amplitude estimation using matrix pencil (MP) and MF for $L = 6$ with $m = 36$ or 81 samples. (a) MSE in estimating the delays. (b) MSE in estimating the amplitudes.

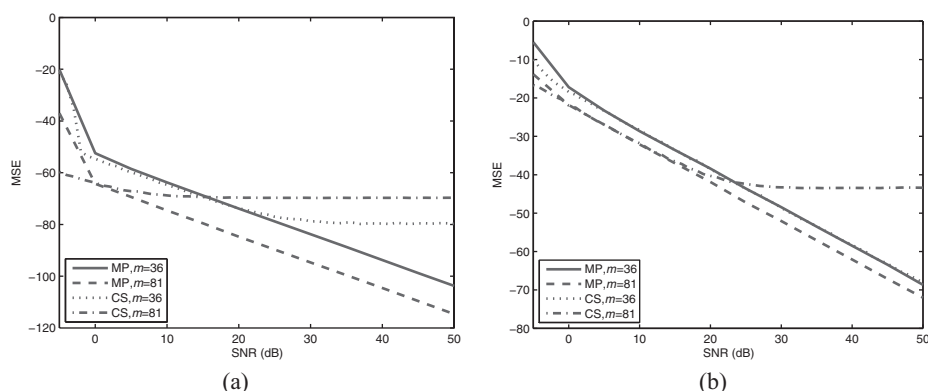


Figure 15.22 Delay and amplitude estimation using matrix pencil (MP) and CS with consecutive frequency values for $L = 6$ using $m = 36$ or 81 samples. (a) MSE in estimating the delays. (b) MSE in estimating the amplitudes.

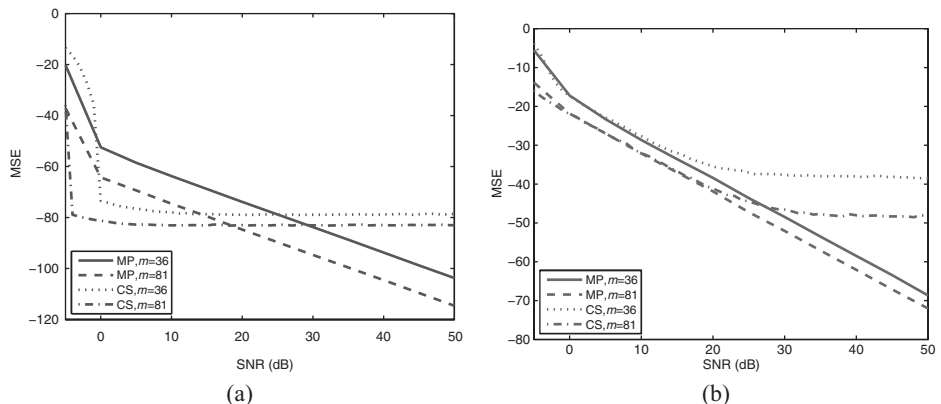


Figure 15.23 Delay and amplitude estimation using matrix pencil (MP) and CS with random frequency values spread over a wide aperture, for $L = 6$ using $m = 36$ or 81 samples. (a) MSE in estimating the delays. (b) MSE in estimating the amplitudes.

These simulations show that when sampling below Nyquist, matrix pencil and CS achieve much lower MSE in comparison with MF. It is also evident that when using CS methods, spreading out the frequency values is important to ensure good recovery, and leads to superior performance over consecutive frequency measurements. Comparing CS and matrix pencil shows that the former is advantageous in the low SNR regime, where the performance is noise-limited. However, at high SNR values, matrix pencil leads to improved performance and allows for finer resolution.

Example 15.9 We next consider the behavior of matrix pencil, CS and MF as a function of the number of samples m . In particular, we demonstrate the degradation caused by sub-Nyquist sampling when using the MF even at very high SNR. In contrast, we show that the performance of matrix pencil and CS is not heavily influenced by the value of m .

We use the same settings as in the previous example for $m = 20, 40, 60, 80$ samples. The pencil parameter for each choice of m is again set as the middle of the recommended range resulting in $M = 8, 17, 25, 33$. Figure 15.24 shows the MSE (in log scale) using the MF for $L = 6$ pulses. The performance of matrix pencil is illustrated in Fig. 15.25. In Fig. 15.26 we plot the results using CS with consecutive frequency values, while a random frequency set is chosen in Fig. 15.27.

Evidently, the performance of MF degrades quite rapidly. When $m < 60$ the MSE is very poor even at high SNR. On the other hand, matrix pencil leads to reliable results even when $m = 20$ and is only slightly affected by the reduction in the number of samples. CS also provides good performance as long as $m > 20$ and random frequency values are chosen. The figures demonstrate once again the superiority of CS over matrix pencil in the low SNR regime, and the advantage of matrix pencil in the high SNR region. The importance of using random spread out frequencies in conjunction with CS is also nicely illustrated.

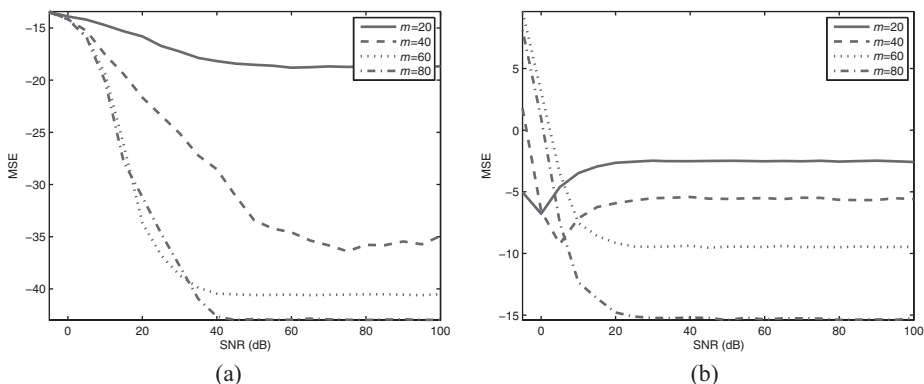


Figure 15.24 Delay and amplitude estimation using the MF with $m = 20, 40, 60, 80$ samples for $L = 6$. (a) MSE in estimating the delays. (b) MSE in estimating the amplitudes.

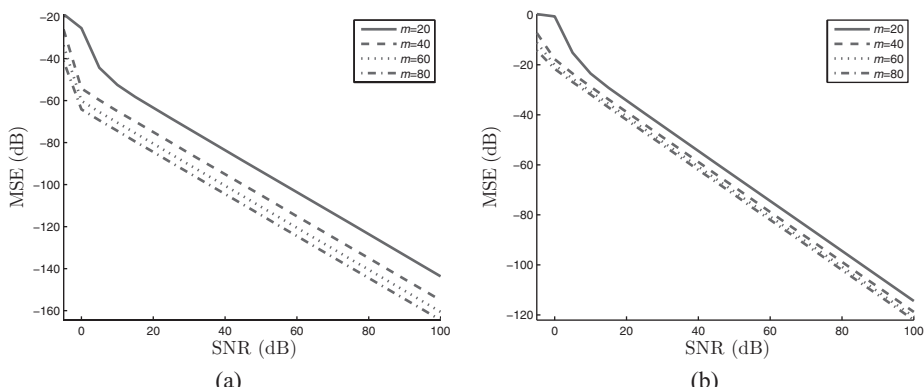


Figure 15.25 Delay and amplitude estimation using matrix pencil (MP) with $m = 20, 40, 60, 80$ samples for $L = 6$. (a) MSE in estimating the delays. (b) MSE in estimating the amplitudes.

Example 15.9 demonstrates the potential of sub-Nyquist methods. However, to allow for low-rate samples we must replace the MF by a more sophisticated recovery process. In addition, the sampling scheme needs to be designed such that the required frequency samples can be determined from the resulting low-rate samples. We discuss this topic next.

15.3 Sub-Nyquist sampling with a single channel

In the previous section we introduced a variety of methods for recovering the delays and amplitudes in a pulse stream of the form (15.7), given a set $m \geq 2L$ of Fourier coefficients $X[k]$, $k \in \mathcal{K}$. In practice, however, the signal is sampled in the time domain, and therefore we do not have direct access to samples of $X[k]$. We now show how these coefficients can be obtained conveniently by sampling $x(t)$ at a low rate. In this section we consider the simplest form of sampling: a single filter, followed by uniform low-rate

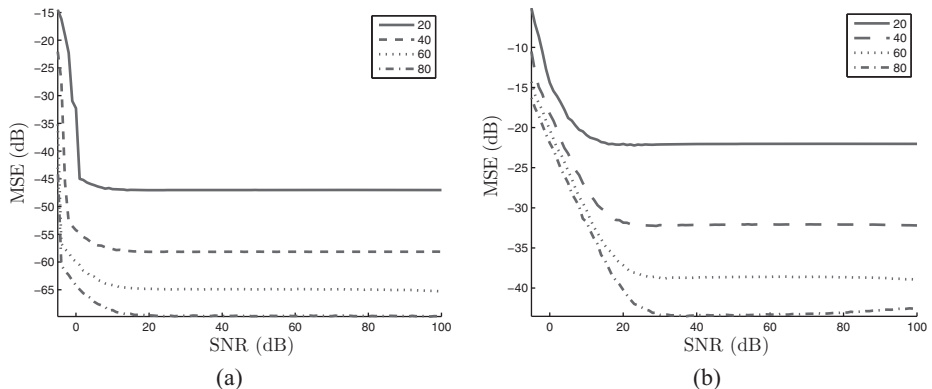


Figure 15.26 Delay and amplitude estimation using CS with consecutive frequency values with $m = 20, 40, 60, 80$ samples for $L = 6$. (a) MSE in estimating the delays. (b) MSE in estimating the amplitudes.

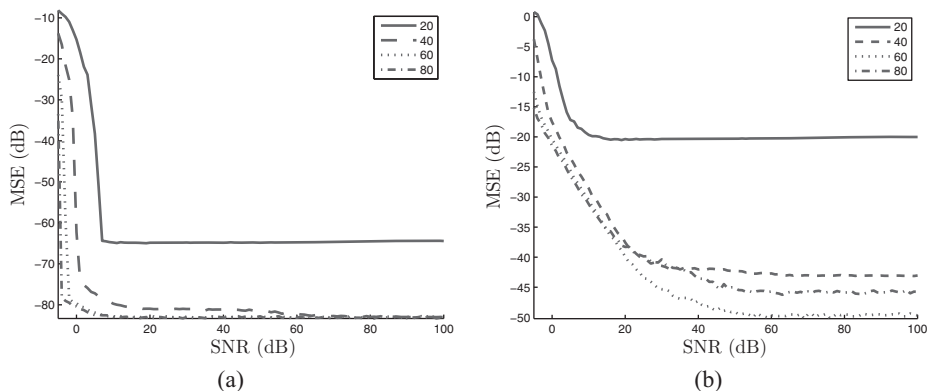


Figure 15.27 Delay and amplitude estimation using CS with random (spread) frequency values with $m = 20, 40, 60, 80$ samples for $L = 6$. (a) MSE in estimating the delays. (b) MSE in estimating the amplitudes.

sampling, which leads to the notion of *coset sampling*. In Section 15.4 we treat multichannel structures that consist of a bank of modulators and integrators, and filterbank systems that contain multiple sampling filters. Although multichannel schemes require more hardware, they often result in simpler filters and lower average sampling rates (in the nonperiodic setting).

We begin by focusing on periodic pulse streams of the form (15.18), which is the easiest case to analyze. We will then see how the results generalize to the finite and infinite pulse stream settings.

15.3.1 Coset sampling

The most straightforward approach to reduce the sampling rate is to filter the periodic pulse stream $x(t)$ with a filter $\overline{s(-t)}$, and then sample the output with period T , as

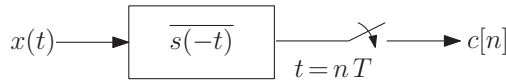


Figure 15.28 Single-channel sampling scheme with $T = \tau/m$.

illustrated in Fig. 15.28. In order to obtain m samples per period τ , we choose $T = \tau/m$. Below we derive conditions on the filter $s(t)$ and the set of Fourier coefficients \mathcal{K} such that the required values $X[k], k \in \mathcal{K}$ can be determined from the samples. As we will see, the constraints on \mathcal{K} lead to sampling over cosets, where \mathcal{K} can contain only one value from each coset. Each coset includes frequencies that are aliased together when sampling at the given reduced rate. Requiring that \mathcal{K} consists of only one value from each coset ensures that no aliasing occurs, as explained further below. For clarity, we confine ourselves to uniform sampling of the filter output, although the results extend in a straightforward manner to nonuniform sampling as well.

Using the general scheme of Fig. 15.28, the samples are given by

$$c[n] = \int_{-\infty}^{\infty} x(t) \overline{s(t - nT)} dt = \langle s(t - nT), x(t) \rangle. \quad (15.85)$$

Substituting (15.24) into (15.85) we have

$$\begin{aligned} c[n] &= \sum_{k \in \mathbb{Z}} X[k] \int_{-\infty}^{\infty} e^{j \frac{2\pi k}{\tau} t} \overline{s(t - nT)} dt \\ &= \sum_{k \in \mathbb{Z}} X[k] e^{j \frac{2\pi k}{\tau} nT} \int_{-\infty}^{\infty} e^{j \frac{2\pi k}{\tau} t} \overline{s(t)} dt \\ &= \sum_{k \in \mathbb{Z}} X[k] e^{j \frac{2\pi k}{\tau} nT} \overline{S(2\pi k/\tau)}, \end{aligned} \quad (15.86)$$

where $S(\omega)$ is the CTFT of $s(t)$. Choosing any filter $s(t)$ which satisfies

$$S(\omega) = \begin{cases} 0, & \omega = 2\pi k/\tau, k \notin \mathcal{K} \\ \text{nonzero}, & \omega = 2\pi k/\tau, k \in \mathcal{K} \\ \text{arbitrary}, & \text{otherwise}, \end{cases} \quad (15.87)$$

we can rewrite (15.86) as

$$c[n] = \sum_{k \in \mathcal{K}} X[k] e^{j \frac{2\pi k}{\tau} nT} \overline{S(2\pi k/\tau)} = \sum_{k \in \mathcal{K}} X[k] e^{j \frac{2\pi k}{m} n} \overline{S(2\pi k/\tau)}, \quad (15.88)$$

where we used the fact that $T = \tau/m$. In contrast to (15.86), the sum in (15.88) is finite. Note that (15.87) implies that any real filter meeting this condition will satisfy $k \in \mathcal{K} \Rightarrow -k \in \mathcal{K}$, and in addition $S(2\pi k/\tau) = \overline{S(-2\pi k/\tau)}$, owing to the conjugate symmetry of real filters.

Define the $m \times m$ diagonal matrix \mathbf{S} with k th entry $\overline{S(2\pi k/\tau)}$ for all $k \in \mathcal{K}$, and the length- m vector \mathbf{c} with n th element $c[n]$. We may then write (15.88) as

$$\mathbf{c} = \mathbf{V}(\{-2\pi\ell/m\})_{m \times m} \mathbf{S} \mathbf{x}, \quad (15.89)$$

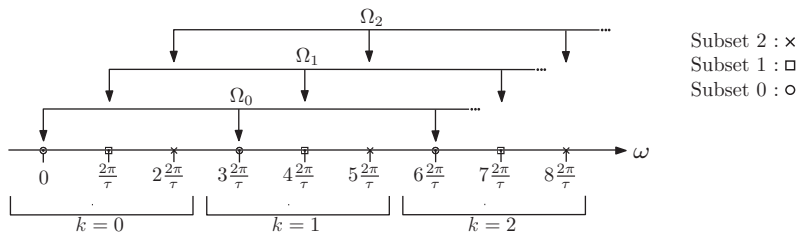


Figure 15.29 Coset sampling for $m = 3$.

where \mathbf{V} is defined by (15.30) with $\omega_\ell = -2\pi\ell/m$ for $\ell \in \mathcal{K}$ and \mathbf{x} is the length- m vector with elements $X[k]$, $k \in \mathcal{K}$. Thus, we need to choose \mathcal{K} and $S(\omega)$ such that $\mathbf{V}(\{-2\pi\ell/m\})_{m \times m}\mathbf{S}$ is left-invertible, so that \mathbf{x} can be determined from (15.89).

The matrix \mathbf{S} is invertible by construction. To ensure invertibility of \mathbf{V} , the values of $\ell \in \mathcal{K}$ must be distinct modulo m . Otherwise, we will have two columns that are identical. This condition on the frequencies in \mathcal{K} can be understood as follows. Let \mathcal{I} denote the set of frequencies $\omega_k = 2\pi k/\tau$ for which $X[k] \neq 0$. We divide \mathcal{I} into m subsets where the ℓ th group, $\ell = 0, \dots, m-1$, contains the frequencies $\Omega_\ell = \{2\pi(\ell + km)/\tau\}$ for all values of k such that Ω_ℓ is in \mathcal{I} . These sets, which we refer to as *cosets*, are illustrated in Fig. 15.29. In order to construct a valid \mathcal{K} we must choose one element from each group Ω_ℓ . This type of sampling is therefore referred to as coset sampling. Under this requirement on \mathcal{K} , and assuming that $S(\omega)$ satisfies (15.87), the coefficients \mathbf{x} can be found from (15.89).

Example 15.10 Consider the case illustrated in Fig. 15.29, corresponding to $m = 3$.

In this case the three subsets (circles, squares, and stars, respectively) are:

$$\Omega_0 = \{\dots, -6\frac{2\pi}{\tau}, -3\frac{2\pi}{\tau}, 0, 3\frac{2\pi}{\tau}, 6\frac{2\pi}{\tau}, \dots\}$$

$$\Omega_1 = \{\dots, -5\frac{2\pi}{\tau}, -2\frac{2\pi}{\tau}, \frac{2\pi}{\tau}, 4\frac{2\pi}{\tau}, 7\frac{2\pi}{\tau}, \dots\}$$

$$\Omega_2 = \{\dots, -4\frac{2\pi}{\tau}, -1\frac{2\pi}{\tau}, 2\frac{2\pi}{\tau}, 5\frac{2\pi}{\tau}, 8\frac{2\pi}{\tau}, \dots\}.$$

A valid sampling scheme will include one element from each subset. As an example, one possible choice is $\mathcal{K} = \{0, 1, 2\}$. Another possibility is $\mathcal{K} = \{-6, -5, 8\}$. Both sets will lead to the same matrix \mathbf{V} since they are identical modulo 3.

Once \mathcal{K} is selected, we need to ensure that $S(\omega)$ is nonzero over the values $2\pi/\tau \cdot \mathcal{K}$ and zero for all other values on the grid $2\pi k/\tau$.

When the frequencies are chosen as described above, the values of \mathcal{K} modulo m are always equal to $0, 1, \dots, m-1$. Thus, with appropriate rearrangement of the columns of \mathbf{V} (and correspondingly those of \mathbf{S} and \mathbf{x}), the matrix \mathbf{V} is equal to $\mathbf{V} = \sqrt{m}\mathbf{F}^*$ where \mathbf{F} is the $m \times m$ Fourier matrix (see Appendix A). We can then write

$$\mathbf{x} = \frac{1}{\sqrt{m}}\mathbf{S}^{-1}\mathbf{F}\mathbf{c}. \quad (15.90)$$

The vector \mathbf{x} is therefore obtained by applying the discrete Fourier transform (DFT) on the (possibly reordered) vector of samples, followed by a correction matrix related to

the sampling filter. Once $X[k], k \in \mathcal{K}$ are determined, we can apply the techniques in the earlier subsections in order to recover the time delays.

The idea behind this sampling scheme can be seen from (15.89): each sample is a linear combination of the elements of \mathbf{x} . The sampling kernel $s(t)$ is designed to pass the coefficients $X[k], k \in \mathcal{K}$ while suppressing all other elements $X[k], k \notin \mathcal{K}$. This operation creates smearing (or aliasing) in time, as illustrated in Fig. 15.3(b), but such that each sample combination is linearly independent of the others, as long as the values of \mathcal{K} are distinct modulo m . This guarantees an invertible system of equations in (15.89).

We summarize coset sampling in the following theorem.

Theorem 15.1. *Consider the τ -periodic stream of pulses of order L :*

$$x(t) = \sum_{\ell=1}^L \sum_{n \in \mathbb{Z}} a_\ell h(t - t_\ell - n\tau).$$

Choose a set \mathcal{K} of indices of size $m = |\mathcal{K}|$ for which $H(2\pi k/\tau) \neq 0, \forall k \in \mathcal{K}$ and such that all values in \mathcal{K} are distinct modulo m . Set $T = \tau/m$. Then the samples

$$c[n] = \langle s(t - nT), x(t) \rangle, \quad n = 0 \dots m - 1,$$

uniquely determine the signal $x(t)$ for any $s(t)$ satisfying condition (15.87), as long as $m \geq 2L$. The Fourier coefficients $X[k], k \in \mathcal{K}$ can be determined from the samples $c[n]$ via (15.90).

Example 15.11 A simple example of a filter satisfying the conditions of Theorem 15.1 is $s(t) = (1/T) \text{sinc}(t/T)$, with $T = \tau/m$ and $m \geq 2L$ [105]. In this case $s(t)$ is an ideal LPF with bandwidth π/T (see Example 3.12) so that $S(\omega) = 1$ for $|\omega| \leq \pi/T$. The condition in (15.87) is therefore satisfied with $\mathcal{K} = \{-\lfloor m/2 \rfloor, \dots, \lfloor m/2 \rfloor\}$. Note that because this filter is real-valued, $k \in \mathcal{K}$ implies $-k \in \mathcal{K}$, i.e., the indices come in pairs except for $k = 0$. Since $k = 0$ is part of the set \mathcal{K} , the cardinality $m = |\mathcal{K}|$ must be odd-valued leading to $m \geq 2L + 1$ samples, rather than the minimal rate $m \geq 2L$.

The previous example showed that we can sample pulse streams at a low rate by filtering the input with a LPF and uniformly sampling the output. This scheme is very simple to implement in practice. However, it has several drawbacks. First, the ideal LPF has infinite time-support, so that it cannot be extended to finite and nonperiodic infinite streams of pulses. Second, in many cases we can gain robustness to noise by spreading out the Fourier samples over the support of $X(\omega)$, rather than choosing consecutive values in \mathcal{K} .

We next propose a class of nonbandlimited sampling kernels, which exploit the additional degrees of freedom in condition (15.87). These filters have compact support in the time domain, and can be designed to pass any choice of frequencies \mathcal{K} . The compact support allows this class to be extended to finite and infinite streams, as we show in Section 15.3.4.

15.3.2 Sum-of-sincs filter

One possibility to obtain a filter satisfying (15.87) is by positioning a sinc function $\text{sinc}(\omega/(2\pi/\tau) - k)$ at every value $k \in \mathcal{K}$. Each such sinc will contribute a value of one at k , and zero at other multiples of $2\pi/\tau$. The resulting filter is referred to as a *sum-of-sincs (SoS) filter* [429], and can be written as

$$G(\omega) = \tau \sum_{k \in \mathcal{K}} b_k \text{sinc}\left(\frac{\omega}{2\pi/\tau} - k\right) \quad (15.91)$$

where $b_k \neq 0$, $k \in \mathcal{K}$ are arbitrary coefficients.

Since for each sinc in the sum

$$\text{sinc}\left(\frac{\omega}{2\pi/\tau} - k\right) = \begin{cases} 1, & \omega = 2\pi k'/\tau, k' = k \\ 0, & \omega = 2\pi k'/\tau, k' \neq k, \end{cases} \quad (15.92)$$

the filter $G(\omega)$ satisfies (15.87) by construction. Switching to the time domain

$$g(t) = \text{rect}\left(\frac{t}{\tau}\right) \sum_{k \in \mathcal{K}} b_k e^{j2\pi kt/\tau}, \quad (15.93)$$

which is clearly a time compact filter with support τ . Here

$$\text{rect}(t) = \begin{cases} 1, & |t| \leq \tau/2 \\ 0, & |t| > \tau/2. \end{cases} \quad (15.94)$$

Example 15.12 A simple example of a SoS filter $g(t)$ is when we choose $\mathcal{K} = \{-p, \dots, p\}$ and set all coefficients $\{b_k\}$ to one. This leads to

$$g(t) = \text{rect}\left(\frac{t}{\tau}\right) \sum_{k=-p}^p e^{j2\pi kt/\tau} = \text{rect}\left(\frac{t}{\tau}\right) D_p(2\pi t/\tau), \quad (15.95)$$

where $D_p(t)$ is the Dirichlet kernel defined by

$$D_p(t) = \sum_{k=-p}^p e^{jkt} = \frac{\sin((p + \frac{1}{2})t)}{\sin(t/2)}. \quad (15.96)$$

The resulting filter for $p = 10$ and $\tau = 1$, is depicted in Fig. 15.30. This filter is also optimal in a MSE sense for the case in which $H(\omega)$ is flat over its support, e.g., $h(t) = \delta(t)$, as we show in Theorem 15.2 below.

Example 15.13 As another example, suppose we choose $b_k, 1 \leq k \leq m$ to be a length- m symmetric Hamming window:

$$b_k = 0.54 - 0.46 \cos\left(2\pi \frac{k + m/2}{m}\right), \quad k \in \mathcal{K}, \quad (15.97)$$

with $\mathcal{K} = \{-10, 9, \dots, 9, 10\}$ and $m = |\mathcal{K}| = 21$. The resulting filter is depicted in Fig. 15.31.

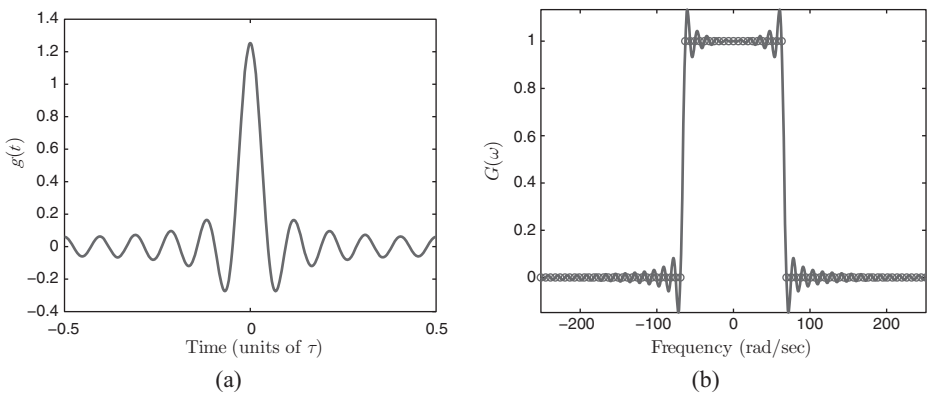


Figure 15.30 The filter $g(t)$ of (15.95) in the (a) time and (b) frequency domains. The values of $G(\omega)$ in $\{2\pi k/\tau\}$ for $k \in \mathbb{Z}$ are marked by circles, and are equal to one for $k \in \mathcal{K}$ and zero for $k \notin \mathcal{K}$.

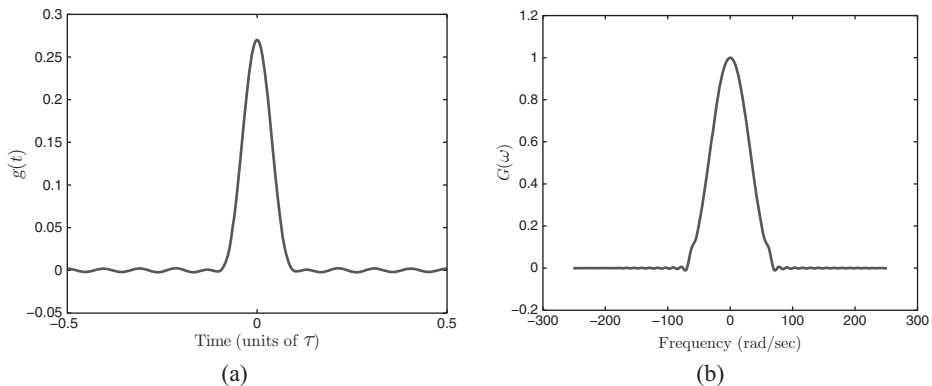


Figure 15.31 The filter $g(t)$ of (15.97) in the (a) time and (b) frequency domains.

Example 15.14 Our final example shows a case in which the $m = 5$ frequencies in \mathcal{K} are not consecutive. Specially, let $\mathcal{K} = \{11, 10, 2, 23, 4\}$, and choose the values b_k to be $\{1, 2, 3, 4, 5\}$. Modulo $m = 5$ the set \mathcal{K} becomes $\{1, 0, 2, 3, 4\}$ so that the values are all distinct, as required. The resulting SoS filter $G(\omega)$ is depicted in Fig. 15.32. Note that for $k \in \mathcal{K}$, the values of $G(2\pi k/\tau)$ are equal to b_k .

We now consider using this filter for sampling and recovery of $x(t)$, where $x(t) = \delta(t - 0.1) + \delta(t - 0.2)$ consists of $L = 2$ delayed delta pulses along the period $\tau = 1$. To sample $x(t)$ we filter it with $s(-t)$ and then sample the output uniformly $m = 5$ times with period $T = 1/5$. Given the samples \mathbf{c} , we use (15.89) to determine the vector \mathbf{x} with elements $X[k]$ for $k \in \mathcal{K}$.

First, we reorder the samples \mathbf{c} so that \mathbf{x} corresponds to $X[k]$ for values $k \bmod m = \{0, 1, 2, 3, 4\}$, namely $k = \{10, 11, 2, 23, 4\}$. This means that we swap the first two entries in \mathbf{c} and \mathbf{x} . In return, we also need to exchange these two values in \mathbf{S} , and the corresponding columns of \mathbf{V} . This leads to the matrix

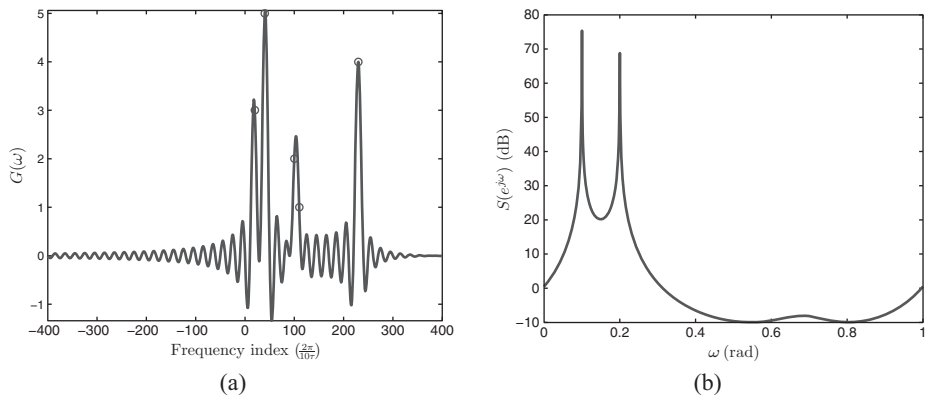


Figure 15.32 (a) The filter $g(t)$ of Example 15.14 in the frequency domain. The circles mark the values of $G(\omega)$ for $k \in \mathcal{K}$, which are equal to b_k in appropriate order. (b) The MUSIC pseudospectrum.

$\mathbf{S} = \text{diag}([2 \ 1 \ 3 \ 4 \ 5])$. We can then determine \mathbf{x} from (15.90). Given \mathbf{x} , we apply MUSIC to determine the delays. The resulting pseudospectrum is depicted in Fig. 15.32. As can be seen, there are two peaks at the correct values of the delays.

In this example we have recovered the signal $x(t)$, which is not bandlimited, from only five samples.

The SoS class in (15.93) may be extended to

$$G(\omega) = \tau \sum_{k \in \mathcal{K}} b_k \phi \left(\frac{\omega}{2\pi/\tau} - k \right) \quad (15.98)$$

where $b_k \neq 0$, $k \in \mathcal{K}$, and $\phi(\omega)$ is any function satisfying:

$$\phi(\omega) = \begin{cases} 1, & \omega = 0 \\ 0, & |\omega| \in \mathbb{Z} \\ \text{arbitrary}, & \text{otherwise.} \end{cases} \quad (15.99)$$

This more general structure allows for smooth versions of the rectangular function, which can be important when practically implementing analog filters.

The function $G(\omega)$ of (15.98) represents a class of filters determined by the parameters $\{b_k\}_{k \in \mathcal{K}}$. These degrees of freedom offer a filter design tool where the values $\{b_k\}_{k \in \mathcal{K}}$ may be optimized for different goals, e.g. parameters which will result in a feasible analog filter. In Theorem 15.2 below, we show how to choose $\{b_k\}$ to minimize the MSE in the presence of noise.

15.3.3 Noise effects

In the presence of noise, the choice of $\{b_k\}_{k \in \mathcal{K}}$ will affect the performance. Consider the case in which digital noise is added to the samples \mathbf{c} , so that $\mathbf{y} = \mathbf{c} + \mathbf{w}$, with \mathbf{w} denoting a white Gaussian noise vector with variance σ^2 . Using (15.89),

$$\mathbf{y} = \sqrt{m}\mathbf{F}^*\mathbf{B}\mathbf{x} + \mathbf{w} \quad (15.100)$$

where \mathbf{B} is a diagonal matrix, having $\{\tau b_k\}$ on its diagonal. Note here that b_k represents a nonzero coefficient which can be located at any frequency $2\pi(k + rm)/\tau$ for an arbitrary integer r . To choose the optimal \mathbf{B} we assume that the amplitudes $\{a_\ell\}$ are uncorrelated with variance σ_a^2 , independent of $\{t_\ell\}$, and that $\{t_\ell\}$ are uniformly distributed in $[0, \tau]$. Since the noise is added to the samples after filtering, increasing the filter's amplification will always reduce the MSE. Therefore, the filter's energy must be normalized, and we do so by adding the constraint $\text{Tr}(\mathbf{B}^*\mathbf{B}) = 1$. Under these assumptions, the following theorem was derived in [429]:

Theorem 15.2. *The minimal MSE of a linear estimator of \mathbf{x} from the noisy samples \mathbf{y} in (15.100) is achieved by choosing the coefficients*

$$b_i = \begin{cases} \frac{\sigma^2}{m\tau^2} \left(\sqrt{\frac{m}{\lambda\sigma^2}} - \frac{1}{|\tilde{h}_i|^2} \right), & \lambda \leq |\tilde{h}_i|^4 m / \sigma^2 \\ 0, & \lambda > |\tilde{h}_i|^4 m / \sigma^2, \end{cases} \quad (15.101)$$

where $\tilde{h}_k = H(2\pi(k + mr)/\tau)\sigma_a\sqrt{L}/\tau$ for the integer value of r that leads to the largest absolute value, and are arranged in an increasing order of $|\tilde{h}_k|$,

$$\sqrt{\lambda} = \frac{(|\mathcal{K}| - M)\sqrt{m/\sigma^2}}{|\mathcal{K}|}, \quad (15.102)$$

$$m/\sigma^2 + \sum_{i=M+1}^{|\mathcal{K}|} 1/|\tilde{h}_i|^2$$

and M is the smallest index for which $\lambda \leq |\tilde{h}_{M+1}|^4 m / \sigma^2$.

Note that the theorem derives the optimal filter coefficients under the assumption of linear recovery. In practice, however, all the methods we outlined for estimating the values of a_ℓ and t_ℓ are nonlinear. Nonetheless, this allows us to obtain some insight into the optimal choice of filter values. In particular, the coefficients b_k of (15.101) have the intuitive property that they are larger for larger values of h_k : We expect to give more emphasis to Fourier coefficients corresponding to high signal values.

In the case in which \tilde{h}_k are equal, we have the following corollary:

Corollary 15.3. *If \tilde{h}_k are all equal then the optimal coefficients are $\beta_k = 1/(m\tau)$ for all $k \in \mathcal{K}$.*

When $h(t) = \delta(t)$, or more generally, $H(\omega)$ is flat over its support, Corollary 15.3 implies that the filter coefficients should all be chosen equally. Following this result, we will set $b_k = b_j$ for all $k, j \in \mathcal{K}$ in noisy simulations in which $h(t) = \delta(t)$. Note, however, that this still leaves open the question of how to choose \mathcal{K} . Some practical guidelines for selecting the frequencies are suggested in [432, 452]. Roughly speaking, these recommendations amount to choosing at least two Fourier coefficients consecutively, but at the same time spreading out the frequencies in order to cover a wide aperture. The motivation behind these rules is that widening the frequency aperture results in finer resolution, while choosing consecutive coefficients helps avoid ambiguities. As an example, the sub-Nyquist radar prototype reported in [432] uses a constellation consisting

of four groups of consecutive coefficients, where the individual bands are spread randomly over the signal bandwidth. In practice, this type of sampling is achieved by using four bandpass filters and low-rate sampling of each filtered output. See Fig. 15.40 for an image of the prototype, as well as the discussion in that section for more details. On the other hand, in the context of ultrasound imaging, the authors of [453] consider a single bandpass filter centered around the high-energy portion of the spectrum, in accordance with Theorem 15.2.

Example 15.15 We now examine the importance of choosing the coefficients b_k optimally via Theorem 15.2.

Consider an input $x(t) = \delta(t - 0.2) + \delta(t - 0.4)$ consisting of $L = 2$ delayed delta pulses along the period $\tau = 1$. Note that this signal has infinite bandwidth. Nonetheless, we will use only 11 samples to recover it by choosing the frequency values corresponding to indices $\mathcal{K} = \{-5, \dots, 5\}$. To obtain the desired coefficients, we filter $x(t)$ with $g(t)$ of (15.91). The filter output is sampled uniformly $m = 11$ times, with sampling period $T = 1/m$. White Gaussian noise with variance σ^2 to achieve the desired SNR is added to the samples.

In Fig. 15.33 we examine the MSE between the frequency coefficients resulting from (15.90) and the real frequency coefficients (15.26) for two different choices of the filter $s(t)$. The first is the optimal filter according to Corollary 15.3, which is depicted in Fig. 15.30. The second is the length- m symmetric Hamming window of Fig. 15.31. Clearly the optimal choice of b_k results in improved MSE.

The performance of matrix pencil using the estimated frequency coefficients is demonstrated in Fig. 15.34. We next consider the performance of CS using the estimated frequency coefficients with a grid of 1000 points and consecutive frequency values (as used in matrix pencil). The results are depicted in Fig. 15.35. Here again the advantage of the optimal choice is evident.

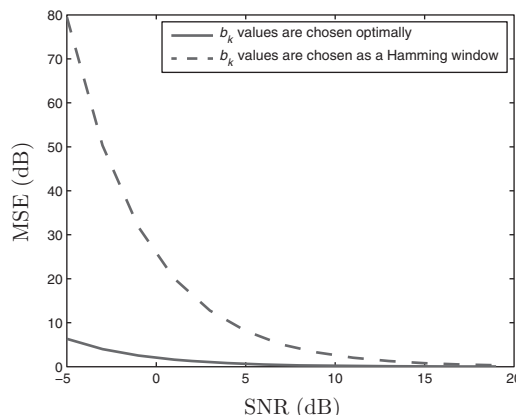


Figure 15.33 MSE in estimating the Fourier coefficients using the optimal values of b_k and using a Hamming window.

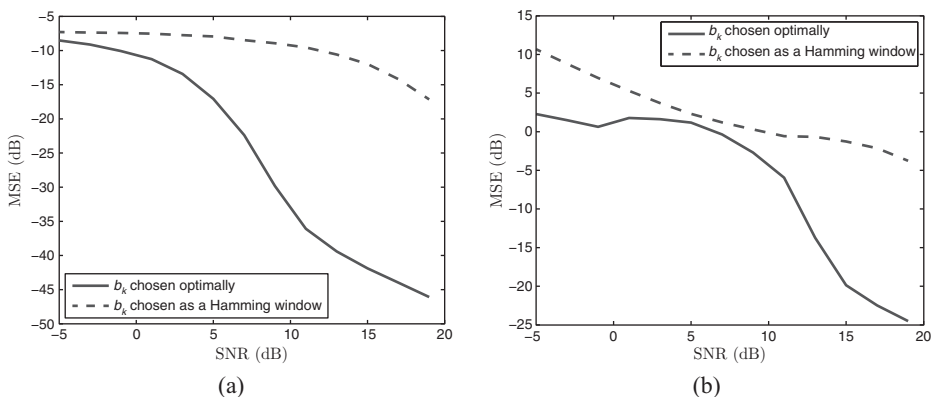


Figure 15.34 Delay and amplitude estimation using matrix pencil (MP) with the optimal values of b_k and with a Hamming window. (a) MSE in estimating the delays. (b) MSE in estimating the amplitudes.

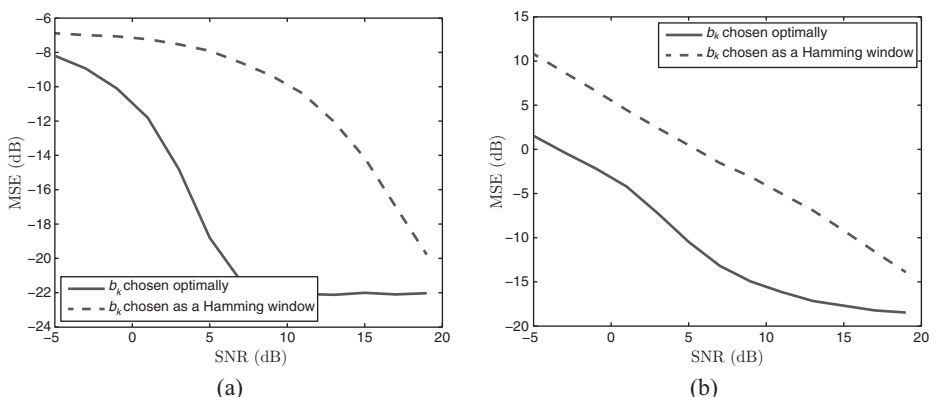


Figure 15.35 Delay and amplitude estimation using CS with consecutive frequencies with optimal values of b_k and with a Hamming window. (a) MSE in estimating the delays. (b) MSE in estimating the amplitudes.

Finally, it is interesting to compare different optimal choices of b_k . While Theorem 15.2 implies that the values should be set to $b_k = 1$, it leaves open the question of how to select the frequencies $k \in \mathcal{K}$. In Fig. 15.36 we plot the results using a random choice of frequencies from the range $[0, 110]$. As we have seen in Examples 15.8 and 15.9, spreading out the frequency values improves the performance considerably.

15.3.4 Finite and infinite pulse streams

Relying on the compact support property of the SoS kernels, we now show how they can be used for sampling of finite and infinite pulse streams.

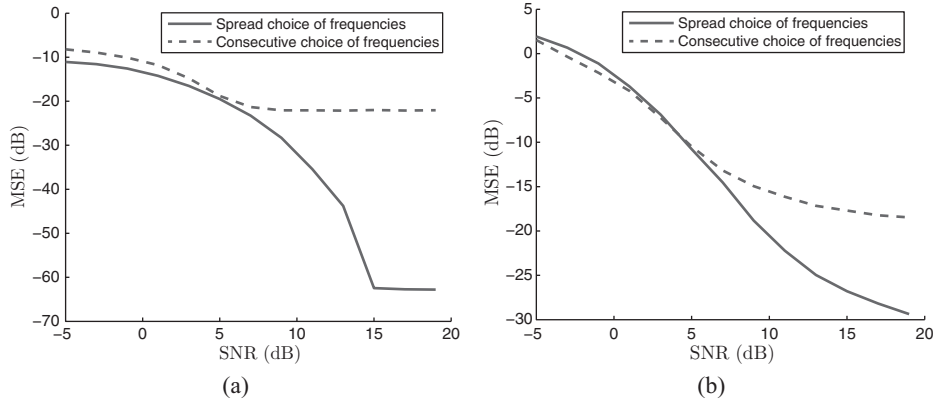


Figure 15.36 Delay and amplitude estimation using CS with consecutive frequencies and with a random choice of frequencies, and optimal values of b_k . (a) MSE in estimating the delays. (b) MSE in estimating the amplitudes.

Finite streams

Consider a finite stream of pulses, defined by

$$x(t) = \sum_{\ell=1}^L a_\ell h(t - t_\ell), \quad t_\ell \in [0, \tau], \quad (15.103)$$

where $h(t)$ is a known pulse shape, and $\{t_\ell, a_\ell\}_{\ell=1}^L$ are the unknown delays and amplitudes. The time-delays $\{t_\ell\}_{\ell=1}^L$ are restricted to lie in a finite time interval $[0, \tau]$, and we assume that the pulse $h(t)$ has finite support R , namely

$$h(t) = 0, \quad |t| \geq R/2. \quad (15.104)$$

Recall that our primary interest is in very short pulses which have wide, or even infinite, frequency support, and therefore cannot be sampled efficiently using classical sampling results for bandlimited signals.

In the case of a periodic pulse stream, the samples $c[n]$ in Fig. 15.28 are given by

$$c[n] = \sum_{i \in \mathbb{Z}} \sum_{\ell=1}^L a_\ell \int_{-\infty}^{\infty} h(t - t_\ell - i\tau) \overline{s(t - nT)} dt = \sum_{i \in \mathbb{Z}} \sum_{\ell=1}^L a_\ell \varphi(nT - t_\ell - i\tau), \quad (15.105)$$

where we defined

$$\varphi(\vartheta) = \langle s(t - \vartheta), h(t) \rangle. \quad (15.106)$$

Choosing $s(t)$ as a compactly supported filter that vanishes for all $|t| > \tau/2$, the support of $\varphi(t)$ is $R + \tau$:

$$\varphi(t) = 0, \quad |t| \geq (R + \tau)/2. \quad (15.107)$$

Using this property, the summation in (15.105) will be over nonzero values for indices i satisfying

$$|nT - t_\ell - i\tau| < (R + \tau)/2. \quad (15.108)$$

Sampling within the window $[0, \tau]$, and noting that the time delays lie in the interval $t_\ell \in [0, \tau)$, $\ell = 1 \dots L$, (15.108) implies that

$$(R + \tau)/2 > |nT - t_\ell - i\tau| \geq |i|\tau - |nT - t_\ell| > (|i| - 1)\tau. \quad (15.109)$$

Here we used the triangle inequality and the fact that $|nT - t_\ell| < \tau$ in our setting. Therefore,

$$|i| < \frac{R/\tau + 3}{2} \Rightarrow |i| \leq \left\lceil \frac{R/\tau + 3}{2} \right\rceil - 1 \stackrel{\Delta}{=} r, \quad (15.110)$$

i.e. the elements of the sum in (15.105) vanish for all i but the values in (15.110). Consequently, the infinite sum in (15.105) reduces to a finite sum over $i \leq |r|$ leading to

$$\begin{aligned} c[n] &= \sum_{i=-r}^r \sum_{\ell=1}^L a_\ell \int_{-\infty}^{\infty} h(t - t_\ell) \overline{s(t - nT + i\tau)} dt \\ &= \left\langle \sum_{i=-r}^r s(t - nT + i\tau), \sum_{\ell=1}^L a_\ell h(t - t_\ell) \right\rangle. \end{aligned} \quad (15.111)$$

Defining a function which consists of $2r + 1$ periods of $s(t)$:

$$s_r(t) = \sum_{i=-r}^r s(t + i\tau), \quad (15.112)$$

we conclude that

$$c[n] = \langle s_r(t - nT), x(t) \rangle. \quad (15.113)$$

Therefore, the samples $c[n]$ can be obtained by filtering $x(t)$ with the filter $\overline{s_r(-t)}$ prior to sampling. This filter has compact support equal to $(2r + 1)\tau$.

Suppose, for example, that the support R of $h(t)$ satisfies $R \leq \tau$. We then obtain from (15.110) that $r = 1$. Therefore, the filter $s_r(t)$ consists of three periods of $s(t)$:

$$s_1(t) = s(t - \tau) + s(t) + s(t + \tau). \quad (15.114)$$

Example 15.16 Consider sampling the finite signal $x(t) = \sum_{\ell=1}^L a_\ell \delta(t - t_\ell)$ for $t \in [0, 1]$, where $a_\ell = 1$, $t_\ell = \ell\Delta$, and $\Delta = 0.025$. The samples are corrupted by zero-mean white Gaussian noise with variance chosen to meet the required SNR. We choose the frequency set $K = -L, \dots, L$, so that $m = |K| = 2L + 1$. Thus, our sampling rate is very close to its minimal rate of $2L$ samples.

Since the support of $h(t) = \delta(t)$ satisfies $R \leq \tau = 1$ the parameter r in (15.110) equals one, and therefore we filter $x(t)$ with $s_1(t)$ of (15.114). For $s(t)$, we use an SoS filter with coefficients b_k all set to 1. The output of the filter is sampled uniformly m times, with sampling period $T = 1/m$. The frequency coefficients are obtained from (15.90).

In Fig. 15.37 we plot the MSE as a function of SNR using the matrix pencil method. Evidently, the results are quite robust even for large values of L .

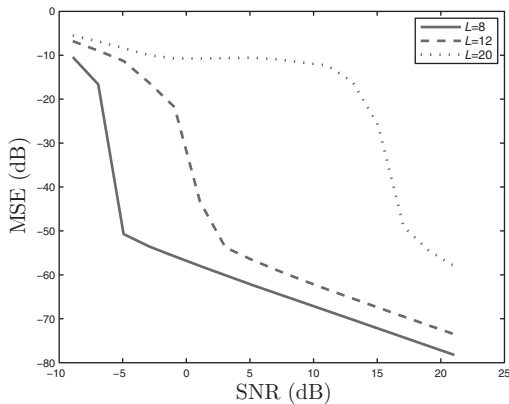


Figure 15.37 The MSE in estimating L delays in a finite pulse stream, for different choices of L , as a function of the SNR.

Infinite streams

A similar technique can also be used to sample and recover infinite-length FRI pulse streams of the form

$$x(t) = \sum_{\ell \in \mathbb{Z}} a_\ell h(t - t_\ell). \quad (15.115)$$

We assume that the infinite signal has a “bursty” character, i.e. the signal has two distinct phases: (a) bursts of maximal duration τ containing at most L pulses, and (b) quiet phases between bursts, in which there is no signal. For simplicity, we begin with the case $h(t) = \delta(t)$. For this choice the filter $s_r(-t)$ in (15.112) reduces to $\overline{s_1(-t)}$ of (15.114).

Since the filter $s_1(-t)$ has compact support 3τ we are assured that the current burst cannot influence samples taken $3\tau/2$ seconds before or after it. In the finite setting, we confined ourselves to sampling within the interval $[0, \tau)$. Similarly, here, we assume that the samples are taken during the burst duration. Therefore, if the minimal spacing between any two consecutive bursts is $3\tau/2$, then we are guaranteed that each sample is influenced by one burst only. The infinite problem then reduces to sequential local distinct finite order problems.

Extending this result to a general pulse $h(t)$ is straightforward, as long as $h(t)$ is compactly supported with support R , and we filter with $\overline{s_r(-t)}$ as defined in (15.112) with the appropriate r from (15.110). In this case we require that the minimal spacing between two adjacent bursts is greater than $((2r + 1)\tau + R)/2$.

An alternative approach to sample finite and infinite pulse streams without having to assume separation between bursts is by using a multichannel system, which we discuss in Section 15.4. This allows to avoid forming a delayed pulse as in $s_r(t)$, which may be difficult to implement in hardware.

Sampling with exponential reproducing kernels

Another class of compact support kernels that can be used to sample finite-length FRI signals is given by the family of exponential reproducing kernels [454, 455].

An exponential reproducing kernel is any function $\varphi(t)$ that, together with its shifted versions, can generate complex exponentials of the form $e^{\alpha_m t}$. Specifically,

$$\sum_{n \in \mathbb{Z}} c_{k,n} \varphi(t - n) = e^{\alpha_k t} \quad (15.116)$$

where $k = 0, 1, \dots, m - 1$. The coefficients are given by $c_{k,n} = \langle e^{\alpha_k t}, \tilde{\varphi}(t - n) \rangle$, where $\tilde{\varphi}(t)$ is the biorthogonal function of $\varphi(t)$, that is, $\langle \varphi(t - n), \tilde{\varphi}(t - k) \rangle = \delta_{nk}$. When sampling pulse streams, it is suggested in [454] to choose $\alpha_k = \alpha_0 + k\lambda$ for some $\alpha_0, \lambda \in \mathbb{C}$.

To see how we can use $\varphi(t)$ to sample finite pulse streams, suppose for simplicity that $h(t) = \delta(t)$ so that

$$x(t) = \sum_{\ell=1}^L a_\ell \delta(t - t_\ell). \quad (15.117)$$

We filter $x(t)$ with $(1/T)\varphi(-t/T)$ where $T = \tau/m$, and sample the output at times nT . This results in measurements

$$y[n] = \sum_{\ell=1}^L a_\ell \varphi\left(\frac{t_\ell}{T} - n\right). \quad (15.118)$$

We now linearly combine the samples with the coefficients $c_{k,n}$ of (15.116) to obtain the new measurements

$$s[k] = \sum_n c_{k,n} y[n], \quad k = 0, 1, \dots, m - 1. \quad (15.119)$$

Using (15.118),

$$s[k] = \sum_{\ell=1}^L a_\ell \sum_n c_{k,n} \varphi\left(\frac{t_\ell}{T} - n\right) = \sum_{\ell=1}^L a_\ell e^{\frac{\alpha_0 t_\ell}{T}} e^{\frac{\lambda t_\ell k}{T}} = \sum_{\ell=1}^L \tilde{a}_\ell u_\ell^k, \quad (15.120)$$

where $\tilde{a}_\ell = a_\ell e^{\frac{\alpha_0 t_\ell}{T}}$ and $u_\ell = e^{\frac{\lambda t_\ell k}{T}}$. These measurements have the form of a power series as we studied in (15.32), and therefore can be solved using the same class of methods.

15.4 Multichannel sampling

The techniques discussed so far were based on uniform sampling of the signal $x(t)$ after filtering with a single filter $\overline{s(-t)}$ (see Fig. 15.28). Lower sampling rates for the finite and infinite settings and more practical hardware devices can often be achieved at the cost of using several channels. In this section we consider multichannel sampling architectures for sub-Nyquist sampling of pulse streams [432, 434, 435, 456, 457]. In particular, we focus on two different systems: modulation and integration channels, and filterbanks.

The first architecture we treat consists of p channels of modulators and integrators. The output of each branch is given by

$$c_\ell[n] = \int_{(n-1)T}^{nT} x(t) s_\ell(t), \quad \ell = 1, \dots, p, \quad n \in \mathbb{Z}, \quad (15.121)$$

where $s_\ell(t)$ is the modulating function on the ℓ th branch. Thus, in every period T we obtain p outputs, resulting in a total sampling rate of p/T . This scheme is particularly simple, and as we show below, can be used to treat all classes of FRI signals: periodic, finite, infinite, and semiperiodic, under the assumption that the pulse $h(t)$ is compactly supported.

An alternative approach is to use filterbanks, where the signal $x(t)$ is convolved with p kernels $\overline{s_1(-t)}, \dots, \overline{s_p(-t)}$, and the output of each channel is sampled at a rate $1/T$. The set of samples in this case is given by

$$c_\ell[n] = \langle s_\ell(t - nT), x(t) \rangle, \quad \ell = 1, \dots, p, \quad n \in \mathbb{Z}. \quad (15.122)$$

Since there are p channels, the total sampling rate is again p/T . We illustrate the filterbank approach for the semiperiodic setting and show that it can accommodate arbitrary pulse shapes $h(t)$, including infinite length. In certain cases, this structure can be implemented as a single sampling channel followed by a serial to parallel converter, leading to hardware savings while still retaining the benefits of multichannel structures.

15.4.1 Modulation-based multichannel systems

We begin by discussing the modulator-based multichannel structure and focus first on periodic pulse streams.

Periodic pulse streams

Consider a τ -periodic stream of L pulses, as in (15.18). Recall from Section 15.2 that if the Fourier coefficients of this signal are available, then standard techniques of spectral analysis or compressed sensing can be used to recover the unknown pulse shifts and amplitudes. The multichannel setup provides a simple and intuitive method for obtaining these Fourier coefficients by correlating the signal $x(t)$ with the Fourier basis functions

$$s_k(t) = \begin{cases} e^{-j\frac{2\pi}{\tau}kt}, & t \in [0, \tau] \\ 0, & \text{elsewhere,} \end{cases} \quad (15.123)$$

for $k \in \mathcal{K}$, where \mathcal{K} are the desired Fourier coefficients and $|\mathcal{K}| = m \geq 2L$. We set the sampling interval T to be equal to the signal period τ , resulting in a total sampling rate of m/τ for all channels. We thus have a sampling system functioning at the rate of innovation when $m = 2L$, and yielding the desired Fourier coefficients of $x(t)$. An additional advantage of this approach is that the kernels have compact support – their support corresponds to one period of the FRI signal, which is smaller than the support of the kernel proposed in Section 15.3.2. This property will facilitate the extension of this scheme to infinite FRI signals.

In principle, we can use the system of Fig. 15.38 to obtain any desired set of frequencies. However, when m is large, this requires implementing many modulators in parallel, which tends to be difficult. A practical alternative, suggested in [432], is to select the frequencies to consist of several bands of consecutive values, spread over a wide aperture. This offers a compromise between the bandwidth of the chosen values (which

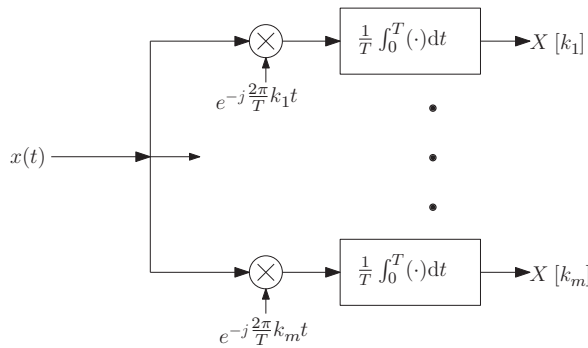


Figure 15.38 Modulation-based multichannel sampling for periodic FRI signals. The resulting samples are the Fourier series coefficients of $x(t)$ at the required frequencies. Note that we only sample once every period, thus $T = \tau$.

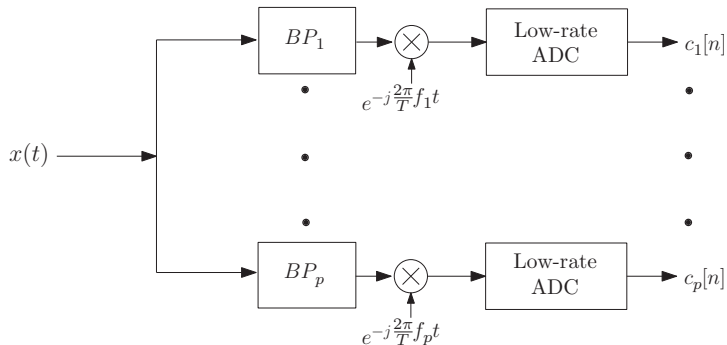


Figure 15.39 Multichannel receiver choosing bands of Fourier coefficients.

we often would like to be large), the minimal separation between the points (which we want to be small enough to avoid ambiguities), and the number of required channels. In this case, instead of acquiring each frequency separately as in Fig. 15.38, we aggregate consecutive values and obtain them jointly by filtering the input with a bandpass filter that encompasses the required values, followed by demodulation to baseband and lowrate sampling of the desired band. This idea is illustrated schematically in Fig. 15.39 and forms the basis for the sampling prototype we discuss next.

Hardware design

A board-level hardware prototype of the multichannel receiver of Fig. 15.39 was developed in [432] for radar detection, and is shown in Fig. 15.40. The board consists of four parallel channels which sample distinct bands of the signal spectrum. Each channel comprises a bandpass crystal filter with an effective random carrier frequency that filters the desired band, demodulates it to baseband, and then samples the band at its Nyquist rate. In this scheme, instead of sampling isolated Fourier coefficients, we acquire four sets of consecutive values. This allows to trade off between the theoretical algorithmic

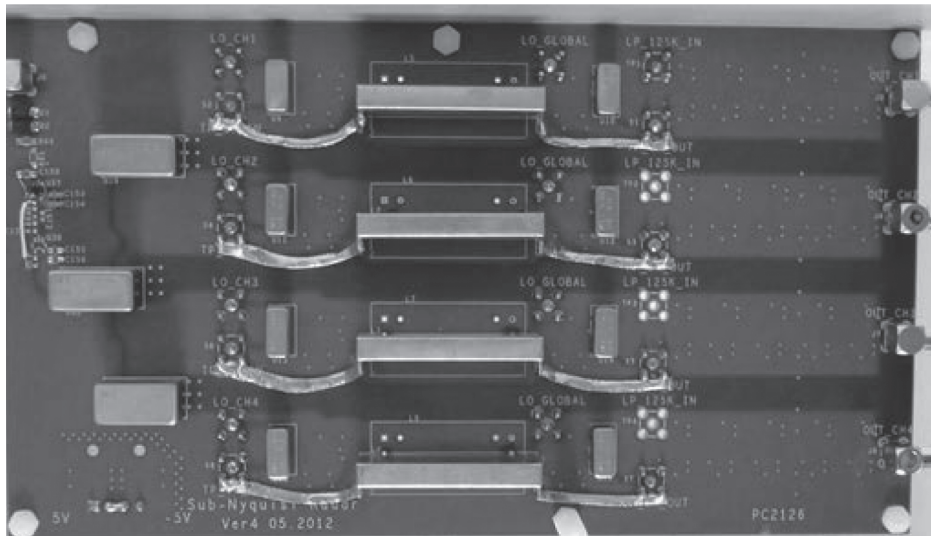


Figure 15.40 The four-channel sub-Nyquist board.

requirements, which may benefit from a fully distributed selection, and the constraints of practical analog filters.

The advantage of crystal filters is that they have an extremely narrow transition band which allows low-rate sampling to be achieved, while extracting a sufficient number of Fourier coefficients. Since crystal filters are standard, off-the-shelf components, the channel design must be adapted to their properties, in order to maximize their efficiency. The prototype developed in [432] therefore includes appropriate filtering and modulation stages. A detailed description of the board and its properties can be found in [432].

In the context of radar, it has been shown that this prototype can lead to a 30-fold reduction in sampling rate while maintaining reasonable target location and velocity estimation even at very low SNR values [431, 432]. The application to radar along with simulation results using this prototype are discussed in more detail in Section 15.7.1.

Periodic waveforms

Instead of functions of the form (15.123), one can use sampling kernels which are a linear combination of these sinusoids, as in Fig. 15.41. In each channel, we modulate the signal using a weighted sum of exponentials given by

$$s_\ell(t) = \sum_{k \in \mathcal{K}} s_{\ell k} e^{-j \frac{2\pi}{T} kt}, \quad (15.124)$$

where the weights $s_{\ell k}$ vary from channel to channel. The samples on the ℓ th channel are then

$$c_\ell = \frac{1}{T} \int_0^T x(t) \sum_{k \in \mathcal{K}} s_{\ell k} e^{-j \frac{2\pi}{T} kt} dt = \sum_{k \in \mathcal{K}} s_{\ell k} X[k]. \quad (15.125)$$

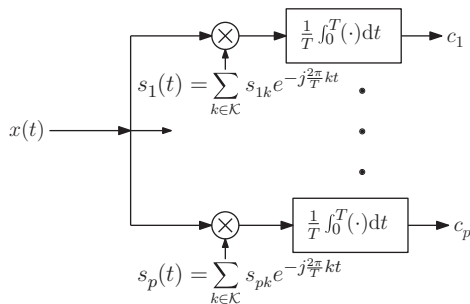


Figure 15.41 Mixing the Fourier coefficients differently in each channel.

This choice can be advantageous from a hardware point of view. If we appropriately choose the linear combinations, the resulting modulating functions $s_\ell(t)$ may have a simple form, such as low-pass versions of binary sequences [457]. In fact, we can use similar sequences to those suggested in the context of the MWC in Chapter 14. In particular, this allows to reduce hardware complexity by using a small number of binary sequences and their shifts. In addition, in real-life scenarios one or more channels might fail, owing to malfunction or noise corruption, leading to loss of information stored in that branch. By mixing the coefficients we distribute the information about each Fourier coefficient among several sampling channels. Consequently, when one or more branches fail, the required Fourier coefficients may still be recovered from the remaining samples [457].

To relate the samples and the Fourier coefficients, we define the $p \times m$ matrix \mathbf{S} with $s_{\ell k}$ as its ℓk th element, and by \mathbf{c} the length- p sample vector with ℓ th element c_ℓ . We then write (15.125) in matrix form as $\mathbf{c} = \mathbf{S}\mathbf{x}$. As long as \mathbf{S} has full column rank, where $p \geq m$ is a necessary condition, we can recover the length- m vector \mathbf{x} from the samples via $\mathbf{x} = \mathbf{S}^\dagger \mathbf{c}$.

We next discuss in more detail the use of periodic waveforms. Suppose that $p_i(t)$ is a periodic waveform with period T . We can expand $p_i(t)$ using a Fourier series as

$$p_i(t) = \sum_{k \in \mathbb{Z}} d_i[k] e^{j\frac{2\pi}{T} kt}, \quad (15.126)$$

where $d_i[k]$ are the Fourier series coefficients. The sum in (15.126) is generally infinite, in contrast to the finite sum in (15.124). Therefore, we filter $p_i(t)$ with a filter $g(t)$ which rejects the unwanted elements in (15.126). The filtered waveforms $\tilde{p}_i(t) = p_i(t) * g(t)$ are also periodic. It can be readily shown that their Fourier series coefficients are given by (see Exercise 5)

$$\tilde{d}_i[k] = d_i[k] G\left(\frac{2\pi}{T} k\right), \quad (15.127)$$

where $G(\omega)$ is the CTFT of $g(t)$. From (15.127), the shaping filter $g(t)$ has to satisfy

$$G(\omega) = \begin{cases} \text{nonzero,} & \omega = \frac{2\pi}{T} k, k \in \mathcal{K} \\ 0, & \omega = \frac{2\pi}{T} k, k \notin \mathcal{K} \\ \text{arbitrary,} & \text{otherwise,} \end{cases} \quad (15.128)$$

so that $\tilde{d}_i[k] = 0$ for $k \notin \mathcal{K}$. This condition is similar to (15.87) obtained for single channel sampling.

An important special case is when $p_i(t)$ consists of $N \geq m$ values, flipping at rate N/T :

$$s_i(t) = \sum_{\ell \in \mathbb{Z}} \sum_{n=0}^{N-1} \alpha_i[n] p(t - nT/N - \ell T), \quad (15.129)$$

where $p(t)$ is a unit-pulse of length T/N , and $\alpha_i[n]$ takes on the values ± 1 . These are precisely the sequences used in the implementation of the MWC discussed in Section 14.4.4. We can often choose the sequence such that one periodic stream is sufficient for all channels, where each channel uses a delayed version of this common waveform. Therefore, the requirement for multiple oscillators and the need for accurate multiples of the basic frequency are both removed. In addition, periodic streams are easily designed and implemented digitally.

Suppose that we use the filtered version of (15.129) as modulating waveforms. To compute the mixing matrix \mathbf{S} in this case we first note that the Fourier coefficients $d_i[k]$ of $s_i(t)$ are given by

$$\begin{aligned} d_i[k] &= \frac{1}{T} \sum_{n=0}^{N-1} \alpha_i[n] \sum_{\ell \in \mathbb{Z}} \int_{-\ell T}^{-(\ell-1)T} p(t - nT/N) e^{-j \frac{2\pi}{T} kt} dt \\ &= \frac{1}{T} \sum_{n=0}^{N-1} \alpha_i[n] P\left(\frac{2\pi}{T} k\right) e^{-j \frac{2\pi}{N} kn}, \end{aligned} \quad (15.130)$$

where $P(\omega)$ denotes the CTFT of $p(t)$. After filtering with $g(t)$, the resulting matrix \mathbf{S} can be decomposed as

$$\mathbf{S} = \mathbf{A}\mathbf{W}\Phi, \quad (15.131)$$

where \mathbf{A} is a $p \times N$ matrix with i th element equal to $\alpha_i[n]$, \mathbf{W} is an $N \times m$ matrix with nk th element equal to $e^{-j \frac{2\pi}{N} kn}$, and Φ is a $m \times m$ diagonal matrix with k th diagonal element

$$\Phi_{kk} = \frac{1}{T} P\left(\frac{2\pi}{T} k\right) G\left(\frac{2\pi}{T} k\right). \quad (15.132)$$

To guarantee left-invertibility of Φ we must have that $P\left(\frac{2\pi}{T} k\right) \neq 0$ for $k \in \mathcal{K}$. Left-invertibility of the $p \times m$ matrix \mathbf{AW} can be ensured by proper selection of the sequences $\alpha_i[n]$, where a necessary condition is that $p \geq m$.

Example 15.17 As an example consider creating all sequences by cyclic shifts of one common sequence $\alpha[n]$ so that

$$\alpha_i[n] = \alpha[n - i + 1 \bmod N], \quad (15.133)$$

where we assume $p = N = m$. This suggests that in contrast to the direct scheme in Fig. 15.38, which requires multiple frequency sources, here only one pulse generator is needed, which simplifies the hardware design.

It is easy to see that with this choice, \mathbf{A} will be a circulant matrix:

$$\mathbf{A} = \begin{bmatrix} \alpha[0] & \alpha[1] & \cdots & \alpha[N-1] \\ \alpha[N-1] & \alpha[0] & \cdots & \alpha[N-2] \\ \vdots & \ddots & \ddots & \vdots \\ \alpha[1] & \alpha[2] & \cdots & \alpha[0] \end{bmatrix}. \quad (15.134)$$

Such a matrix can be decomposed as [458]

$$\mathbf{A} = \mathbf{F}^* \operatorname{diag}(\mathbf{F}\boldsymbol{\alpha}) \mathbf{F}, \quad (15.135)$$

where \mathbf{F} is the $N \times N$ Fourier matrix, and $\boldsymbol{\alpha}$ is a length- N vector containing the elements of the sequence $\alpha[n]$. Therefore, for \mathbf{A} to be invertible the DFT of the sequence $\alpha[n]$ cannot take on the value 0. As the pulse $p(t)$ we choose

$$p(t) = \begin{cases} 1, & t \in [0, \frac{T}{N}] \\ 0, & t \notin [0, \frac{T}{N}] \end{cases}. \quad (15.136)$$

The frequency response of this pulse satisfies

$$P(\omega) = \frac{T}{N} e^{-j\frac{T}{2N}\omega} \operatorname{sinc}\left(\frac{T}{2\pi N}\omega\right). \quad (15.137)$$

In Fig. 15.42, we show a modulating waveform in the time and frequency domains, for $p = N = m = 7$. The original time-domain waveform comprises rectangular pulses, whereas low-pass filtering results in a smooth modulating waveform. Switching to the frequency domain, the Fourier series coefficients are shaped by $P(\omega)$, the CTFT of the pulse shape. The shaping filter frequency response, $G(\omega)$, is designed to transfer only the Fourier coefficients whose index is a member of the set $\mathcal{K} = \{-3, \dots, 3\}$, suppressing all other coefficients.

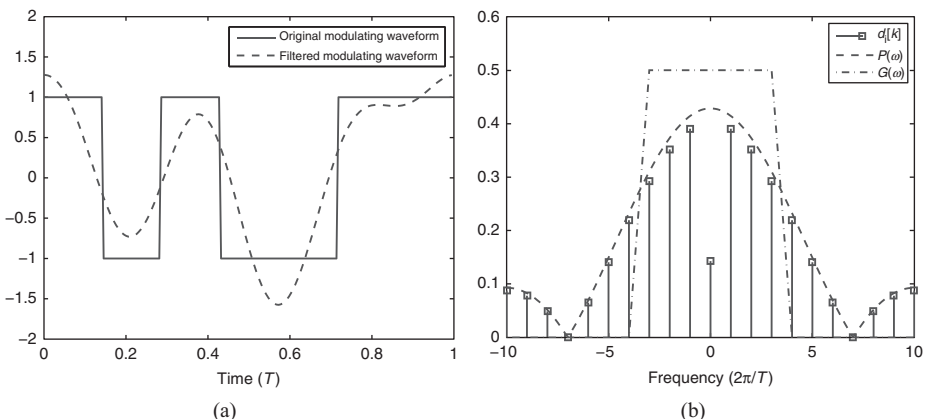


Figure 15.42 Modulating waveform before and after filtering. (a) Time domain. (b) Frequency domain.

Although the concept of using modulation waveforms is based on the MWC, there are some differences between the methods. First, following the mixing stage, here we use an integrator in contrast to the LPF used in the MWC. This is a result of the different signal quantities measured: Fourier coefficients here as opposed to the frequency band's content in the MWC. The second distinction is in the purpose of the mixing procedure. In the MWC mixing is performed in order to reduce the sampling rate relative to the Nyquist rate. In our setting, mixing is used to simplify hardware implementation and to improve robustness to failure in one of the sampling channels.

Infinite FRI signals

We now turn to treat infinite-duration FRI signals of the form (15.115). Suppose that the τ -local rate of innovation is $2L/\tau$, for some value τ . Thus, there are no more than L pulses in any interval $I_n = [(n-1)\tau, n\tau]$. Assume further that the pulses do not overlap interval boundaries, i.e., if $t_k \in I_n$ then $h(t - t_k) = 0$ for all $t \notin I_n$. Such a requirement automatically holds if $h(t)$ is a Dirac delta, and will hold as long as the support of $h(t)$ is substantially smaller than τ .

Under these assumptions, we may treat the signal parameters in each interval separately. Specifically, consider the τ -periodic signal obtained by periodic continuation of the values of $x(t)$ within a particular interval I_n . This periodic signal can be recovered by obtaining $2L$ of its Fourier coefficients using sampling kernels of the form (15.123). Since the support of these kernels is limited to the interval I_n (rather than its periodic continuation), this technique can be applied on the nonperiodic signal $x(t)$. This requires obtaining a sample from each of the channels once every τ seconds, and using $p \geq 2L$ branches, as illustrated in Fig. 15.43. The success of this technique hinges on the availability of sampling kernels whose support is limited to a single period of the periodic waveform.

Denoting by $\mathbf{c}[n]$ the vector containing the samples $c_1[n], \dots, c_p[n]$ at time n , we have

$$\mathbf{c}[n] = \mathbf{S}\mathbf{x}[n] \quad (15.138)$$

where \mathbf{S} is the matrix of elements $s_{\ell k}$, and $\mathbf{x}[n]$ are the desired Fourier coefficients of $x(t)$ over the interval I_n ($\mathbf{x}[n]$ is a length- m vector with $m \geq 2L$). Inverting \mathbf{S} we

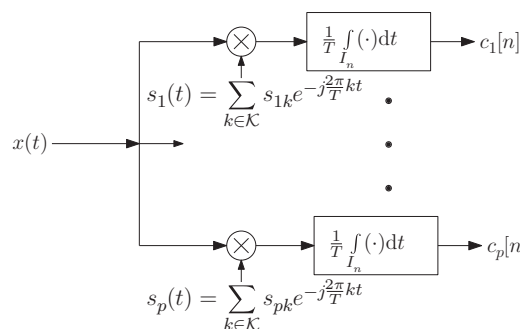


Figure 15.43 Multichannel modulation-based sampling scheme for infinite FRI signals.

obtain the Fourier coefficients over each interval, from which we can find the delays and amplitudes in the n th period. Indeed from (15.25),

$$\mathbf{x}[n] = \mathbf{HV}(\{\omega_\ell[n]\})\mathbf{a}[n], \quad (15.139)$$

where $\omega_\ell[n]$ are the frequencies defining the n th interval, \mathbf{H} is a diagonal matrix containing the Fourier coefficients of the pulse shape, and $\mathbf{a}[n]$ is the vector of amplitudes a_ℓ over the n th interval. Therefore, for each value of n , we may apply the methods studied in this chapter (such as Prony's method, matrix pencil etc.) to (15.139) in order to recover $\omega_\ell[n]$ and $\mathbf{a}[n]$.

Semiperiodic FRI signals

Finally, we consider semiperiodic FRI signals (15.8), which consist of L pulses occurring at repeated intervals τ , with amplitudes $a_\ell[n]$ that vary from one period to the next. The modulator approach of Fig. 15.43 can be used as in the infinite case, with the difference that now the samples from different periods may be jointly processed to improve performance.

Specifically, as before, we recover $\mathbf{x}[n]$ from the output of the modulator bank with $T = \tau$ using (15.138). Since the delays are constant, in the frequency domain (after normalizing the Fourier coefficients by the Fourier coefficients of the pulse if necessary) we have the relation

$$\mathbf{x}[n] = \mathbf{V}(\{\omega_\ell\})_{p \times L}\mathbf{a}[n], \quad n \in \mathbb{Z}, \quad (15.140)$$

where $\mathbf{a}[n]$ is the vector of amplitudes $a_\ell[n]$, and $\omega_\ell = 2\pi t_\ell/\tau$. When there are only a finite number of periods, the same reasoning holds where the set \mathbb{Z} is replaced by a finite set. The derivation is exactly the same as in (15.139) with the exception that here $\omega_\ell[n]$ are independent of n . When only one time instant n is available, we can solve (15.140) using the methods described in Section 15.2. However, now we have many vectors $\mathbf{x}[n]$ that share the same delays – that is, they are related to the Fourier coefficients via a shared matrix \mathbf{V} . This allows the use of robust methods that recover the delays more reliably, by jointly processing the samples for all n .

For example, we can use stochastic subspace algorithms, such as MUSIC and ESPRIT, described in Section 15.2.7. These approaches are based on computing the correlation matrix $\sum_{n \in \mathbb{Z}} \mathbf{x}[n]\mathbf{x}^*[n]$. An alternative is to use the CS formulation of Section 15.2.8, where we extend it to our scenario by solving an IMV (or MMV) problem (see Section 11.6) instead of a single measurement formulation.

Clearly, the condition for the general infinite model $p \geq 2L$ is a sufficient condition here as well in order to ensure recovery of $x(t)$. However, the additional prior on the signal's structure can help to reduce the number of sampling channels. In fact, it turns out that it is sufficient to use

$$p \geq 2L - \eta + 1 \quad (15.141)$$

channels, where η is the dimension of the minimal subspace containing the vector set $\{\mathbf{a}[n], n \in \mathbb{Z}\}$ [434]. Since each vector is of length L the dimension of the subspace spanned by all $\mathbf{a}[n]$ satisfies $\eta \leq L$. When there are a finite number of vectors, this result coincides with Theorem 11.22 which considers necessary and sufficient conditions for

MMV recovery. Noting that $\eta \geq 1$, the lower bound is bounded above by $2L$, resulting in a worst-case sampling rate of $2L/T$. However, when $\eta > 1$, the number of channels p can be reduced beyond the lower limit $2L$ for the periodic model. In Chapter 10 we saw that the minimum sampling rate required for perfect recovery of a union of SI subspaces with L generators is $2L/T$, which is consistent with our results here.

Note that standard MUSIC and ESPRIT methods require that $\eta = L$, namely that the coefficient vectors $\mathbf{a}[n]$ vary enough from period to period so that they span the entire space \mathbb{C}^L . This requirement ensures that the empirical correlation matrix is invertible. In this case, (15.141) implies that the delays can be recovered using only $L + 1$ sampling channels. When $\eta < L$, an additional smoothing stage is needed prior to applying subspace methods, as we explained in Section 15.2.7. Alternatively, rank-aware MMV methods, discussed in Section 11.6, can be used.

To conclude, when the pulse amplitudes vary sufficiently from period to period, which is expressed by the condition $\eta = L$, the common information about the delays can be utilized to reduce the sampling rate to $(L + 1)/T$ with $T = \tau$. Moreover, joint processing improves the estimation of delays in the presence of noise since it uses the mutual information between periods, rather than recovering the delays for each period separately.

Example 15.18 We now demonstrate the advantage of joint processing of semi-periodic FRI signals by comparing the MSE in time delay estimation when recovering the delays from each period separately versus joint recovery.

Consider the signal $x(t) = a_1\delta(t - 0.213) + a_2\delta(t - 0.452) + a_3\delta(t - 0.664) + a_4\delta(t - 0.7453)$, where a_i are Gaussian random variables with mean $\mu = 1$ and standard deviation $\sigma = 1$ which are drawn independently over several periods. The signal is sampled by directly obtaining $m = 9$ consecutive Fourier coefficients symmetric around zero using pure tones. Joint processing is performed using the ESPRIT algorithm (Algorithm 15.7) while recovering the delays from each period separately is obtained via matrix pencil (Algorithm 15.4) with pencil parameter $M = 4$.

The time delay MSE versus SNR for a varying number of periods is depicted in Fig. 15.44. The results are averaged over 1000 simulations. As expected, the use of the mutual information on the delays between periods improves the estimation performance significantly.

15.4.2 Filterbank sampling

An alternative scheme that can be used in the semiperiodic setting is a filterbank system [434]. The advantage of this technique is that one need not assume the existence of distinct pulse intervals, nor is it necessary for the pulse shape to have compact support. Here as well we will exploit the semiperiodicity to jointly process the samples by using subspace or MMV methods.

When the pulse shape $h(t)$ is arbitrary, the derivation departs somewhat from the modulation bank technique. This is a result of the fact that the signal is not periodic and

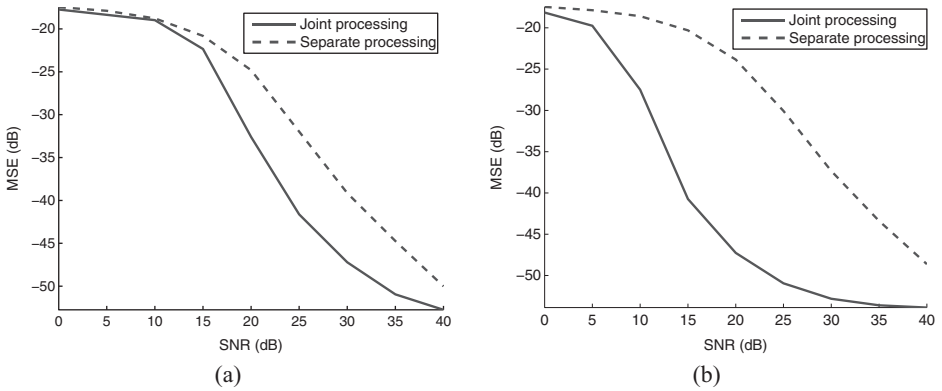


Figure 15.44 MSE in estimating the delays by joint processing versus individual processing.
(a) Joint processing over 10 periods. (b) Joint processing over 50 periods.

cannot be divided into distinct intervals, so that one can no longer speak of its Fourier series. Instead, in parallel to how we derived the Fourier series approach, we will begin by considering recovery given an appropriate transform of $x(t)$. We will then discuss how the required transform can be obtained from samples of the signal.

We begin by computing the Fourier transform of the semiperiodic signal $x(t)$ of (15.8):

$$\begin{aligned} X(\omega) &= \sum_{\ell=1}^L \sum_{n \in \mathbb{Z}} a_\ell[n] \int_{-\infty}^{\infty} h(t - t_\ell - n\tau) e^{-j\omega t} dt \\ &= H(\omega) \sum_{\ell=1}^L e^{-j\omega t_\ell} \sum_{n \in \mathbb{Z}} a_\ell[n] e^{-j\omega n\tau} \\ &= H(\omega) \sum_{\ell=1}^L A_\ell(e^{j\omega\tau}) e^{-j\omega t_\ell}. \end{aligned} \quad (15.142)$$

To recover t_ℓ we will consider slices of $X(\omega)$ of length $2\pi/\tau$, similarly to Chapter 14. Let the k th slice be defined by

$$X_k(e^{j\omega\tau}) = X\left(\omega + \frac{2\pi k}{\tau}\right), \quad 0 \leq \omega \leq \frac{2\pi}{\tau}. \quad (15.143)$$

That is, it is equal to the frequency content of $X(\omega)$ over $[2\pi k/\tau, 2\pi(k+1)/\tau]$. Using the fact that $A(e^{j\omega\tau})$ is $2\pi/\tau$ -periodic,

$$X_k(e^{j\omega\tau}) = \sum_{\ell=1}^L A_\ell(e^{j\omega\tau}) e^{-j\omega t_\ell} e^{-j2\pi k t_\ell / \tau} H\left(\omega + \frac{2\pi k}{\tau}\right). \quad (15.144)$$

We now show that we can recover the unknown variables from a small number of slices so that we do not need to know the entire CTFT $X(\omega)$. This, in turn, translates to a reduction in sampling rate. Let \mathcal{K} be a set of indices k such that $H(\omega + \frac{2\pi k}{\tau})$ is nonzero almost everywhere on $[0, 2\pi/\tau]$, and introduce the vector-valued function

$\mathbf{x}(e^{j\omega\tau})$, whose elements are given by $X_k(e^{j\omega\tau})$ with $k \in \mathcal{K}$. We can then express $\mathbf{x}(e^{j\omega\tau})$ in matrix form as

$$\mathbf{x}(e^{j\omega\tau}) = \mathbf{H}(e^{j\omega\tau})\mathbf{V}(\{\omega_\ell\})\mathbf{a}(e^{j\omega\tau}), \quad (15.145)$$

where $\omega_\ell = 2\pi t_\ell/\tau$, $\mathbf{H}(e^{j\omega\tau})$ is a diagonal matrix with diagonal elements $H(\omega + \frac{2\pi k}{\tau})$ for $k \in \mathcal{K}$ and $\mathbf{a}(e^{j\omega\tau})$ is the length- L vector of elements $e^{-j\omega t_\ell} A_\ell(e^{j\omega t_\ell})$. Since by definition $\mathbf{H}(e^{j\omega\tau})$ is invertible, we multiply (15.145) by $\mathbf{H}^{-1}(e^{j\omega\tau})$ to obtain

$$\mathbf{y}(e^{j\omega\tau}) = \mathbf{V}(\{\omega_\ell\})\mathbf{a}(e^{j\omega\tau}), \quad (15.146)$$

where $\mathbf{y}(e^{j\omega\tau}) = \mathbf{H}^{-1}(e^{j\omega\tau})\mathbf{x}(e^{j\omega\tau})$. Taking the inverse DTFT of both sides of the equation results in

$$\mathbf{y}[n] = \mathbf{V}(\{\omega_\ell\})\mathbf{a}[n], \quad n \in \mathbb{Z}, \quad (15.147)$$

which has the same structure as (15.140) and can therefore be treated in a similar fashion. Thus, given the set of vectors $\{\mathbf{y}[n]\}$ we can recover $\{t_\ell\}$ and $\{\mathbf{a}[n]\}$ by using, for example, MUSIC, ESPRIT, or MMV methods. The latter requires discretizing the delays, as described in Section 15.2.8.

It remains to discuss how to obtain $\mathbf{y}[n]$ from low-rate samples of $x(t)$. Since we do not need the entire $X(\omega)$, the rate will be lower than the Nyquist rate. Suppose we sample $x(t)$ with $p = |\mathcal{K}|$ sampling filters $s_\ell(-t)$. In this case the DTFT of the sample sequence (15.122) is given by

$$C_\ell(e^{j\omega T}) = \frac{1}{T} \sum_{m \in \mathbb{Z}} S_\ell\left(\omega - \frac{2\pi}{T}m\right) X\left(\omega - \frac{2\pi}{T}m\right), \quad 0 \leq \omega \leq \frac{2\pi}{T}. \quad (15.148)$$

To proceed, we choose $T = \tau$. Our goal then is to be able to recover $X_k(e^{j\omega T})$, $k \in \mathcal{K}$ from $C_\ell(e^{j\omega T})$, $1 \leq \ell \leq p$. To this end we choose $S_\ell(\omega)$ such that for every $0 \leq \omega \leq 2\pi/T$ we have

$$S_\ell\left(\omega - \frac{2\pi}{T}k\right) = \begin{cases} 0, & k \notin \mathcal{K} \\ \text{arbitrary nonzero,} & \text{otherwise.} \end{cases} \quad (15.149)$$

We can then express (15.148) as

$$\mathbf{c}(e^{j\omega T}) = \mathbf{S}(e^{j\omega T})\mathbf{x}(e^{j\omega T}), \quad (15.150)$$

where $\mathbf{S}(e^{j\omega T})$ is a matrix whose ℓ th element is given by $S_\ell(\omega - \frac{2\pi}{T}k)$, $k \in \mathcal{K}$. Thus, if $\mathbf{S}(e^{j\omega T})$ is invertible, then $\mathbf{x}(e^{j\omega T})$ can be recovered from $\mathbf{c}(e^{j\omega T})$.

Example 15.19 A simple example of a set of sampling kernels satisfying the requirements is the ideal bandpass filterbank given by

$$S_\ell(\omega) = \begin{cases} T, & \omega \in [(\ell-1)\frac{2\pi}{T}, \ell\frac{2\pi}{T}], \\ 0, & \text{otherwise,} \end{cases} \quad (15.151)$$

where \mathcal{K} is the set of indices $\ell = 0, \dots, p-1$. The resulting $\mathbf{S}(e^{j\omega T})$ is diagonal.

We can also consider sampling using a single filter followed by uniform sampling with rate p/T with $T = \tau$. In this case the sample sequence is given by

$$C\left(e^{j\omega T/p}\right) = \frac{1}{T} \sum_{k \in \mathbb{Z}} \overline{S\left(\omega - \frac{2\pi}{T} kp\right)} X\left(\omega - \frac{2\pi}{T} kp\right). \quad (15.152)$$

In order to recover $X_k(e^{j\omega T})$, $k \in \mathcal{K}$ we divide the bandwidth of $X(\omega)$ into intervals of length $2\pi/T$. We then define the ℓ th subset as the intervals starting at frequencies $\Omega_\ell = \{2\pi(\ell + km)/T\}$ for all values of k such that Ω_ℓ is still in the bandwidth of $X(\omega)$. To construct a valid set \mathcal{K} we must choose one element from each subset Ω_ℓ , as we did in coset sampling (see Section 15.3). The filter $S(\omega)$ is then chosen such that for every $0 \leq \omega \leq 2\pi/T$,

$$S\left(\omega - \frac{2\pi}{T} k\right) = \begin{cases} 0, & k \notin \mathcal{K} \\ \text{nonzero}, & \text{otherwise.} \end{cases} \quad (15.153)$$

Next we note that $C\left(e^{j\omega T/p}\right)$ is defined over $[0, 2\pi p/T]$. We may therefore represent $C\left(e^{j\omega T/p}\right)$ in terms of p consecutive bands $C_\ell(e^{j\omega T})$ of size $2\pi/T$. Formally, Let $C_\ell(e^{j\omega T}) = C(\omega + 2\pi\ell/T)$ for $\ell = 0, \dots, p-1$ and $\omega \in [0, 2\pi/T)$ and construct a vector $\mathbf{c}(e^{j\omega T})$ whose elements are $C_\ell(e^{j\omega T})$. With these choices we can express (15.152) as

$$\mathbf{c}(e^{j\omega T}) = \mathbf{S}(e^{j\omega T})\mathbf{x}(e^{j\omega T}), \quad (15.154)$$

where $\mathbf{S}(e^{j\omega T})$ is a diagonal matrix with diagonal elements $S\left(\omega - \frac{2\pi}{T} k\right)$, $k \in \mathcal{K}$. Thus, $\mathbf{x}(e^{j\omega T})$ can be recovered from $\mathbf{c}(e^{j\omega T})$ as $\mathbf{x}(e^{j\omega T}) = \mathbf{S}^{-1}(e^{j\omega T})\mathbf{c}(e^{j\omega T})$.

15.5 Noisy FRI recovery

Real-world signals are often contaminated by noise and thus do not conform precisely to the FRI assumptions. Furthermore, like any mathematical model, the FRI framework is an approximation which does not precisely hold in practical scenarios, an effect known as mismodelling error. We have seen in Section 15.2 how some of the techniques for FRI recovery can be adapted to account for noise. Noise may arise both in the analog and digital domains, namely before and after sampling, as illustrated in Fig. 15.45. When noise is present, it is no longer possible to recover the original signal perfectly from its samples. However, one can sometimes mitigate the effects of noise by oversampling, i.e. by increasing the sampling rate beyond the rate of innovation.

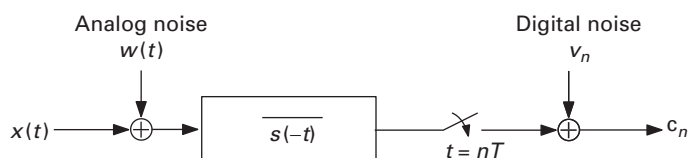


Figure 15.45 The continuous signal $x(t)$ can be corrupted in either the analog or digital paths.

In this section, we describe some results that allow one to analyze the effect of noise on the accuracy with which FRI signals can be recovered. A standard tool for accomplishing this is the Cramér–Rao bound (CRB), which is a lower bound on the MSE achievable by any unbiased estimator [460]. As such, it provides a measure of the difficulty of a given estimation problem, and indicates whether or not existing techniques come close to optimal. It is also useful in evaluating the relative merit of different types of measurements. In particular, we will see that for a large class of FRI signals, sampling with complex exponentials is in fact optimal in a certain MSE sense, justifying the approach we have been following in previous sections.

As our focus in this book is not on performance analysis which involves tools of random processes, we will not go into detailed derivations, but rather concentrate on the final results and conclusions that are relevant to our discussion. The results in this section are based on [314, 461].

15.5.1 MSE bounds

Consider a finite-duration FRI signal $x(t) = h(t, \theta)$, which is determined by a finite number k of parameters represented by the vector θ , over some time interval τ . Suppose we sample a noisy version of the signal

$$y(t) = x(t) + w(t), \quad t \in [0, \tau], \quad (15.155)$$

where $w(t)$ is continuous-time white Gaussian noise with variance σ^2 . The MSE of an estimator $\hat{x}(t)$ of $x(t)$ is defined as

$$\text{MSE}(\hat{x}, x) \triangleq E\{\|\hat{x} - x\|_2^2\} = E\left\{\int_0^\tau |\hat{x}(t) - x(t)|^2 dt\right\}. \quad (15.156)$$

An estimator $\hat{x}(t)$ is said to be unbiased if

$$E\{\hat{x}(t)\} = x(t) \text{ for all possible signals } x(t) \text{ and almost all } t \in [0, \tau]. \quad (15.157)$$

Sampling-indifferent bound

To find a bound on the MSE achievable by any sampling method, it is of interest to derive the CRB for estimating $x(t)$ directly from the continuous-time process $y(t)$. Clearly, no sampling mechanism can do better than exhausting all of the information contained in $y(t)$.

This bound turns out to have a particularly simple closed-form expression which depends on the rate of innovation, but not on the class of FRI signals being estimated. Indeed, under suitable regularity conditions (detailed in [314]) the MSE of any unbiased, finite-variance estimator $\hat{x}(t)$ of a signal $x(t)$ of duration τ , satisfies

$$\frac{1}{\tau} \text{MSE}(\hat{x}, x) \geq \rho_\tau \sigma^2 \quad (15.158)$$

where $\rho_\tau = k/\tau$ is the τ -local rate of innovation. Note that when $x(t)$ does not have structure, no finite-MSE unbiased estimators exist.

The bound in (15.158) offers a new interpretation of the rate of innovation in the noisy setting, as the ratio between the best achievable MSE and the noise variance σ^2 . This is to be contrasted with the characterization of the rate of innovation in the noise-free case as the lowest sampling rate allowing for perfect recovery of the signal; indeed, when noise is present, perfect recovery is no longer possible.

Bound for sampled measurements

We next present a lower bound on estimating $x(t)$ from samples of the signal $y(t)$ of (15.155). To keep the discussion general, we consider samples of the form

$$c_n = \langle \varphi_n(t), y(t) \rangle + v_n, \quad n = 0, \dots, N-1 \quad (15.159)$$

where $\{\varphi_n(t)\}$ is a set of sampling kernels and v_n is measurement noise, which we assume is a white-noise process with variance σ_d^2 . For example, pointwise sampling at the output of an anti-aliasing filter $\varphi(-t)$ corresponds to sampling kernels $\varphi_n(t) = \varphi(t - nT)$. We denote by Φ the subspace spanned by the sampling kernels. In this setting, the samples inherit the noise $w(t)$ embedded in the signal $y(t)$, and may suffer from additional discrete-time noise, for example due to quantization. Note that unless the sampling kernels $\{\varphi_n(t)\}$ happen to be orthogonal, the resulting measurements will not be statistically independent.

We assume that there exists a Fréchet derivative $\frac{\partial x}{\partial \theta}$ which quantifies the sensitivity of $x(t)$ to changes in θ . Informally, $\frac{\partial x}{\partial \theta}$ is an operator from \mathbb{R}^k to the space of square-integrable functions L_2 such that

$$x(t)|_{\theta+\delta} \approx x(t)|_\theta + \frac{\partial x}{\partial \theta}\delta. \quad (15.160)$$

More formally,

$$\lim_{\delta \rightarrow 0} \frac{\|x(\theta + \delta) - x(\theta) - \frac{\partial x}{\partial \theta}\delta\|_{\mathbb{R}^N}}{\|\delta\|_{\mathbb{R}^k}} = 0. \quad (15.161)$$

Suppose for a moment that there exist elements in the range space of $\frac{\partial x}{\partial \theta}$ which are orthogonal to Φ . This implies that one can perturb $x(t)$ without changing the distribution of the measurements c_0, \dots, c_{N-1} . This situation occurs, for example, when the number of measurements N is smaller than the number k of parameters defining $x(t)$. While it may still be possible to reconstruct some of the information concerning $x(t)$ from these measurements, this is an undesirable situation from an estimation point of view. Thus we will assume that

$$\frac{\partial x}{\partial \theta} \cap \Phi^\perp = \{\mathbf{0}\}. \quad (15.162)$$

Under these assumptions, it can be shown that any unbiased, finite-variance estimator $\hat{x}(t)$ of $x(t)$ from the samples (15.159) satisfies [314]

$$\text{MSE}(\hat{x}, x) \geq \text{Tr} \left[\left(\frac{\partial x}{\partial \theta} \right)^* \left(\frac{\partial x}{\partial \theta} \right) \left(\left(\frac{\partial x}{\partial \theta} \right)^* \mathbf{H}_\Phi \left(\frac{\partial x}{\partial \theta} \right) \right)^{-1} \right], \quad (15.163)$$

where \mathbf{H}_Φ is given by

$$\mathbf{H}_\Phi = \Phi (\sigma^2 \Phi^* \Phi + \sigma_d^2 \mathbf{I}_N)^{-1} \Phi^* \quad (15.164)$$

and Φ is the set transformation corresponding to the functions $\{\varphi_n(t)\}_{n=1}^N$. If $\sigma_d = 0$ so that there is only analog noise, then \mathbf{H}_Φ is proportional to the orthogonal projection onto the range space of Φ .

Note that despite the involvement of continuous-time operators, the expression within the trace in (15.163) is a $k \times k$ matrix and can therefore be computed numerically. Also observe that, in contrast to the continuous-time bound of (15.158), the sampled bound depends on the value of θ . Thus, for a specific sampling scheme, some signals can potentially be more difficult to estimate than others.

We now draw several conclusions from (15.163).

Discrete-time noise

Suppose first that $\sigma^2 = 0$, so that only digital noise is present. The effects of this noise can be surmounted either by increasing the gain of the sampling kernels, or by increasing the number of measurements. These intuitive conclusions are easily verified from (15.163). Consider the modified kernels $\tilde{\varphi}_n(t) = 2\varphi_n(t)$. The set transformation $\tilde{\Phi}$ corresponding to the modified kernels is $\tilde{\Phi} = 2\Phi$, and since $\sigma^2 = 0$, this implies that the expression within the trace is reduced by a factor of 4. Thus, a sufficient increase in sampling gain reduces the bound (15.163) arbitrarily close to zero. Similarly, it is possible to increase the number of samples, for example, by repeating each measurement twice. Let Φ and $\tilde{\Phi}$ denote the transformations corresponding to the original and doubled sets of measurements. It is then readily seen from the definition of the set transformation that $\tilde{\Phi}\tilde{\Phi}^* = 4\Phi\Phi^*$. Consequently, the same argument leads to the conclusion that in the absence of continuous-time noise one can achieve arbitrarily low error by repeated measurements. In practice, rather than repeating each measurement, an increase in sampling rate is often obtained by sampling on a denser grid.

Continuous-time noise

Consider next the situation in which $\sigma_d^2 = 0$, meaning that only continuous-time noise affects the samples. In this case, it is generally impossible to achieve arbitrarily low reconstruction error, regardless of the sampling kernels used. Indeed, it is never possible to outperform the continuous-time CRB of (15.158), which is typically nonzero.

The two bounds (15.163) and (15.158) may sometimes coincide. If this occurs, then at least in terms of the performance bounds, estimators based on the samples (15.159) will suffer no degradation compared with an estimator based on the entire continuous-time function. Such a situation occurs if $x(t) \in \Phi$ for any feasible value of $x(t)$, a situation which we refer to as ‘‘Nyquist-equivalent’’ sampling. In this case, $\mathbf{H}_\Phi \frac{\partial x}{\partial \theta} = \frac{1}{\sigma^2} \frac{\partial x}{\partial \theta}$, so that (15.163) reduces to

$$\frac{1}{\tau} \text{MSE}(\hat{x}, x) \geq \frac{\sigma^2}{\tau} \text{Tr}(\mathbf{I}_{k \times k}) = \sigma^2 \rho_\tau. \quad (15.165)$$

Many practical FRI signal models are not contained in any finite-dimensional subspace, and in these cases, any increase in the sampling rate can improve estimation performance. Even if there exists a subspace containing the entire family of FRI signals, its dimension is often much larger than the number of parameters k defining the signal. Consequently, fully exploiting the information in the signal requires sampling at the Nyquist-equivalent rate, which is potentially much higher than the rate of innovation. This fact provides an analytical explanation of the empirically observed phenomena that oversampling often provides improvement over sampling at the rate of innovation in the presence of noise.

It is interesting to examine this phenomenon from a UoS viewpoint. Denote the set of feasible signals by \mathcal{X} and suppose that it can be described as a union of an infinite number of subspaces $\{\mathcal{U}_\alpha\}$ indexed by the continuous parameter α , so that $\mathcal{X} = \bigcup_\alpha \mathcal{U}_\alpha$. In this case, a finite sampling rate captures all of the information present in the signal if and only if

$$\dim \left(\sum_\alpha \mathcal{U}_\alpha \right) < \infty \quad (15.166)$$

where $\dim(\mathcal{M})$ is the dimension of the subspace \mathcal{M} . By contrast, in the noise-free case, we have seen in Chapter 10 that the number of samples required to recover $x(t)$ is given by

$$\max_{\alpha_1, \alpha_2} \dim(\mathcal{U}_{\alpha_1} + \mathcal{U}_{\alpha_2}), \quad (15.167)$$

i.e. the largest dimension among sums of two subspaces belonging to the union. In general, the dimension of (15.166) will be much higher than (15.167), illustrating the qualitative difference between the noisy and noise-free settings. For example, if the subspaces \mathcal{U}_α are finite-dimensional, then (15.167) is also necessarily finite, whereas (15.166) need not be.

Nevertheless, one may hope that the structure embodied in \mathcal{X} will allow nearly optimal recovery using a sampling rate close to the rate of innovation. In general, the CRB for samples taken at the rate of innovation is substantially higher than the optimal, continuous-time bound. This demonstrates that the sensitivity to noise is a fundamental aspect of estimating FRI signals, rather than a limitation of existing algorithms. However, some specific FRI models, such as the semiperiodic pulse stream (15.8), exhibit considerable noise resilience, and indeed in these cases the CRB converges to the continuous-time value more rapidly. We discuss this phenomena in the next section.

15.5.2 Periodic versus semiperiodic FRI signals

The different levels of robustness to noise can be explained when the signal models are examined in a UoS context. In this case, the vector θ parameterizing $x(t)$ can be partitioned into parameters defining the subspace \mathcal{U}_α and parameters pinpointing the position within the subspace. The CRB analysis hints that estimation of the position within a subspace is often easier than estimation of the subspace itself. Thus, when

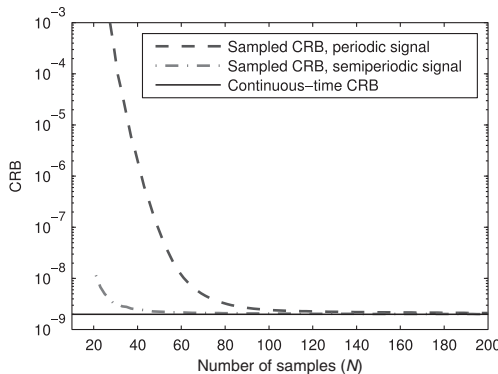


Figure 15.46 Comparison between the CRB for a periodic signal and a semiperiodic signal.

most parameters are used to select an intra-subspace position, estimation at the rate of innovation is successful, as occurs in the semi-periodic case (15.8). By contrast, when a large portion of the parameters define the subspace in use, a sampling rate higher than the rate of innovation is necessary; this is the situation in the nonperiodic pulse stream (15.5), wherein θ is evenly divided among subspace-selecting parameters $\{t_\ell\}$ and intra-subspace parameters $\{a_\ell\}$.

In Fig. 15.46 we compare the CRB for reconstructing a nonperiodic pulse stream and a semiperiodic pulse stream. Both signals consist of an identical pulse $h(t)$ and have the same local rate of innovation. The sampling kernels were chosen to measure the N lowest-frequency components of the signal. For the periodic signal, we choose $L = 10$ pulses with random delays and amplitudes and a period of $\tau = 1$. This implies that the signal of interest is determined by $k = 20$ parameters (L amplitudes and L time delays). To construct a semiperiodic signal with the same number of parameters, we chose a period of $1/9$ with $L = 2$ pulses. The segment $[0, \tau]$ then contains precisely $M = 9$ periods, for a total of 20 parameters: two unknown amplitudes per period plus two unknown delays.

Since the number of parameters to be estimated is identical in both signal models, the continuous-time CRB for the two settings coincides. Consequently, for a large number of measurements, the sampled bounds also converge to the same values. However, when the number of samples is closer to the rate of innovation, the bound on the reconstruction error for the semiperiodic signal is much lower than that of the periodic signal, as shown in Fig. 15.46.

In our setting, the periodic signal contains 10 parameters for selecting the subspace and 10 additional parameters determining the position within it; whereas for the semiperiodic signal, only two parameters determine the subspace while the remaining 18 parameters set the location in the subspace. Evidently, identification of the subspace is challenging, especially in the presence of noise, but once the subspace is determined, the remaining parameters can be estimated using a simple linear operation (a projection onto the chosen subspace). Consequently, if many of the unknown parameters identify the position within a subspace, estimation can be performed more accurately.

15.5.3 Choosing the sampling kernels

An interesting (and difficult) question is how to choose an optimal set of sampling kernels in some sense for a given allotted number of samples. This problem is considered in [314] by adopting a Bayesian framework, wherein the signal $x(t)$ is a random process with the parameters distributed according to a known prior distribution. The sampling and reconstruction techniques are further assumed to be linear. While nonlinear reconstruction methods are typically used for estimating FRI signals, this assumption is required for analytical tractability, and is used only for the purpose of identifying sampling kernels. Once these kernels are chosen, they can be used in conjunction with nonlinear reconstruction algorithms (though in this case no analytic optimality conditions can be provided). Given a budget of N samples, the optimal sampling kernels are given by the N eigenfunctions of the autocorrelation

$$R_X = R_X(t, T) = E\{x(t)x^*(T)\} \quad (15.168)$$

corresponding to the N largest eigenvalues.

A setting of particular interest is when the autocorrelation R_X is cyclic, in the sense that

$$R_X(t, T) = R_X((t - T) \bmod \tau) \quad (15.169)$$

for some τ . This scenario occurs, for example, in the periodic pulse stream (15.7) and the semiperiodic pulse stream (15.8) settings, assuming a reasonable prior distribution on the parameters. It is not difficult to show that the eigenfunctions of R_X are given, in this case, by the complex exponentials

$$\psi_n(t) = \frac{1}{\sqrt{\tau}} e^{j \frac{2\pi}{\tau} nt}, \quad n \in \mathbb{Z}. \quad (15.170)$$

Furthermore, the magnitudes of the eigenvalues of R_X are directly proportional to the magnitudes of the respective Fourier coefficients of the pulse shape $h(t)$. It follows that the optimal sampling kernels are the exponentials (15.170) corresponding to the largest Fourier coefficients of $h(t)$. Interestingly, this is precisely the class of sampling kernels that we have been advocating in our sub-Nyquist FRI sampling techniques.

15.6 General FRI sampling

Although we have focused primarily on sampling streams of pulses, the theory of FRI extends beyond this class of signals. In this section, we address the problem of reconstructing arbitrary FRI signals from possibly nonlinear measurements obtained at the rate of innovation following the ideas presented in [462]. The only assumption on the sampling mechanism and signal prior is that the parameters defining the signal can be stably recovered from the samples. This assumption must be made by any practical sampling theorem that attempts to recover the signal parameters. Whereas in the previous section we focused on explicit recovery techniques, here we take an iterative approach to treat the general setting.

Since we allow nonlinear sampling as well, we use algorithms similar to those introduced in the context of nonlinear sampling of subspace signals in Chapter 8. Specifically, our approach is based on a LS criterion which minimizes the error norm between the given set of samples and those of our signal estimate. Under the stability assumption, this LS criterion possesses a unique stationary point. Consequently, any optimization algorithm designed to trap a stationary point, will necessarily converge to the true parameters. In particular, we show that the steepest-descent and quasi-Newton methods, introduced in Chapter 8, can be used to recover the signal parameters in our setting as well. This approach provides a unified framework for recovering signals from samples taken at their rate of innovation without making any specific assumptions on the signal structure.

We focus on recovery of an arbitrary segment from an FRI signal of the form $x(t) = h(t, \theta)$ where $\theta \in \mathcal{A}$ is the length- k parameter vector defining $x(t)$ and \mathcal{A} is the set of possible vectors. We assume that h is Fréchet-differentiable with respect to θ . We denote the set of signals $x(t)$ by \mathcal{X} . In order to identify θ , we must ensure that there do not exist two vectors $\theta_1 \neq \theta_2$ such that $h(t, \theta_1) = h(t, \theta_2)$. For the recovery to be stable, we require the slightly stronger condition

$$\alpha_h \|\theta_1 - \theta_2\|_2 \leq \|h(t, \theta_1) - h(t, \theta_2)\|_2 \quad (15.171)$$

for some constant $\alpha_h > 0$ and for all $\theta_1, \theta_2 \in \mathcal{A}$. In the case of pulse streams, for example, (15.171) implies that $t_\ell - t_{\ell-1}$ has to be bounded above and below for every ℓ , and that $a_\ell > a > 0$.

15.6.1 Sampling method

Our goal is to recover x by observing N generalized samples $\mathbf{c} = (c_1, \dots, c_N)^T$ obtained as $\mathbf{c} = S(x)$, where $S : L_2(\mathbb{R}) \rightarrow \mathbb{R}^N$ is some (possibly nonlinear) Fréchet-differentiable operator. For example, S can represent the samples

$$c_n = f(\langle s_n, x \rangle), \quad n = 1, \dots, N, \quad (15.172)$$

where $f(\cdot)$ is a nonlinear sensor response and s_n are the linear sampling functions.

We say that a sampling operator S is *stable with respect to \mathcal{X}* if there exist constants $0 < \alpha_s \leq \beta_s < \infty$ such that

$$\alpha_s \|x_2 - x_1\|_{L_2} \leq \|S(x_1) - S(x_2)\|_{\mathbb{R}^N} \leq \beta_s \|x_2 - x_1\|_{L_2} \quad (15.173)$$

for all $x_1, x_2 \in \mathcal{X}$. This definition is the same as that used in Chapter 10 apart from the fact that here the set \mathcal{X} is not necessarily a UoS and the operator S is not required to be linear. The left-hand inequality ensures that if two signals x_1 and x_2 are sufficiently different from one another, then their samples $S(x_1)$ and $S(x_2)$ differ as well. In particular, it implies that two distinct signals $x_1, x_2 \in \mathcal{X}$ cannot produce the same set of samples, so that there is a unique recovery $x \in \mathcal{X}$ associated with every valid set of samples $\mathbf{c} = S(x) \in \mathbb{R}^N$.

Conditions (15.173) and (15.171) lie at the heart of any practical sampling theorem, whether implicitly or not. We do not discuss here in detail situations in which these conditions are satisfied, as this is rather problem-specific. The interested reader may refer to [463] and Chapter 8 for an analysis of SI signals with nonlinear samples, to [464] for linear sampling of several UoS models, and to [465] for a general theory of stability in FRI settings. In what follows, we show that conditions (15.173) and (15.171) dictate a minimal sampling rate below which perfect recovery cannot be guaranteed. More interestingly, we will also see that when these requirements are met, perfect recovery is possible at this minimal sampling rate by using a wide family of iterative algorithms.

15.6.2 Minimal sampling rate

To be able to devise a general reconstruction strategy for signals in \mathcal{X} that were sampled by S , we first determine the minimal number of samples N required for perfect recovery.

Proposition 15.7. *Suppose that the function $h : \mathcal{A} \rightarrow L_2$ satisfies (15.171) and that the operator $S : L_2 \rightarrow \mathbb{R}^N$ satisfies (15.173). Then*

$$N \geq k + \max_{x_1 \in \mathcal{X}} \dim \left(\mathcal{N} \left(\frac{\partial S}{\partial x} \Big|_{x_1} \right)^* \right), \quad (15.174)$$

where k is the rate of innovation.

Proof: For brevity, we use the shorthand notation $h(\boldsymbol{\theta})$ instead of $h(t, \boldsymbol{\theta})$. Since $h(\boldsymbol{\theta})$ and $S(x)$ are Fréchet-differentiable, it follows that the function $\hat{\mathbf{c}}(\boldsymbol{\theta}) = S(h(\boldsymbol{\theta}))$ is Fréchet-differentiable as well. We start by showing that its derivative $\partial \hat{\mathbf{c}} / \partial \boldsymbol{\theta}$, which is an $N \times k$ matrix, has an empty null space.

By definition (15.161), the Fréchet derivative $\partial \hat{\mathbf{c}} / \partial \boldsymbol{\theta}$ at $\boldsymbol{\theta}_1$ satisfies

$$\lim_{\boldsymbol{\delta} \rightarrow 0} \frac{\left\| \hat{\mathbf{c}}(\boldsymbol{\theta}_1 + \boldsymbol{\delta}) - \hat{\mathbf{c}}(\boldsymbol{\theta}_1) - \frac{\partial \hat{\mathbf{c}}}{\partial \boldsymbol{\theta}} \Big|_{\boldsymbol{\theta}_1} \boldsymbol{\delta} \right\|}{\|\boldsymbol{\delta}\|} = 0. \quad (15.175)$$

In particular, for any nonzero $\mathbf{a} \in \mathbb{R}^k$,

$$\lim_{t \rightarrow 0} \frac{\left\| \hat{\mathbf{c}}(\boldsymbol{\theta}_1 + t\mathbf{a}) - \hat{\mathbf{c}}(\boldsymbol{\theta}_1) - t \frac{\partial \hat{\mathbf{c}}}{\partial \boldsymbol{\theta}} \Big|_{\boldsymbol{\theta}_1} \mathbf{a} \right\|}{\|t\mathbf{a}\|} = 0, \quad (15.176)$$

where t is a scalar variable. Now, assume that $\mathbf{a} \in \mathcal{N}(\partial \hat{\mathbf{c}} / \partial \boldsymbol{\theta} |_{\boldsymbol{\theta}_1})$. Then (15.176) implies that

$$\lim_{t \rightarrow 0} \frac{\|\hat{\mathbf{c}}(\boldsymbol{\theta}_1 + t\mathbf{a}) - \hat{\mathbf{c}}(\boldsymbol{\theta}_1)\|}{\|t\mathbf{a}\|} = 0. \quad (15.177)$$

However, from (15.171) and (15.173),

$$\begin{aligned} \frac{\|\hat{\mathbf{c}}(\boldsymbol{\theta}_1 + t\mathbf{a}) - \hat{\mathbf{c}}(\boldsymbol{\theta}_1)\|}{\|t\mathbf{a}\|} &= \frac{\|S(h(\boldsymbol{\theta}_1 + t\mathbf{a})) - S(h(\boldsymbol{\theta}_1))\|}{\|t\mathbf{a}\|} \\ &\geq \alpha_s \frac{\|h(\boldsymbol{\theta}_1 + t\mathbf{a}) - h(\boldsymbol{\theta}_1)\|}{\|t\mathbf{a}\|} \\ &\geq \alpha_s \alpha_h > 0 \end{aligned} \quad (15.178)$$

for every $t \neq 0$. This contradicts (15.177) and therefore demonstrates that $\mathcal{N}(\partial\hat{\mathbf{c}}/\partial\boldsymbol{\theta}|_{\boldsymbol{\theta}_1}) = \{\mathbf{0}\}$, which implies that $\dim(\mathcal{R}(\partial\hat{\mathbf{c}}/\partial\boldsymbol{\theta}|_{\boldsymbol{\theta}_1})) = k$.

Next, note that $\partial\hat{\mathbf{c}}/\partial\boldsymbol{\theta}|_{\boldsymbol{\theta}_1} = (\partial S/\partial x|_{h(\boldsymbol{\theta}_1)})(\partial h/\partial\boldsymbol{\theta}|_{\boldsymbol{\theta}_1})$ so that $\mathcal{R}(\partial\hat{\mathbf{c}}/\partial\boldsymbol{\theta}|_{\boldsymbol{\theta}_1}) \subseteq \mathcal{R}(\partial S/\partial x|_{h(\boldsymbol{\theta}_1)}) = \mathcal{N}((\partial S/\partial x|_{h(\boldsymbol{\theta}_1)})^*)^\perp$. Therefore,

$$k \leq \dim \left(\mathcal{N} \left(\frac{\partial S}{\partial x} \Big|_{h(\boldsymbol{\theta}_1)} \right)^*{}^\perp \right) = N - \dim \left(\mathcal{N} \left(\frac{\partial S}{\partial x} \Big|_{h(\boldsymbol{\theta}_1)} \right)^* \right). \quad (15.179)$$

Since (15.179) holds for every $\boldsymbol{\theta}_1 \in \mathcal{A}$, it holds for the $\boldsymbol{\theta}_1$ minimizing the right-hand side, completing the proof. \square

Proposition 15.7 shows that stable recovery is impossible when sampling below the rate of innovation. It also implies that if the null space of $(\partial S/\partial x)^*$ is nonempty at some $x \in \mathcal{X}$, then sampling at the rate of innovation is insufficient. We consider some examples below.

Example 15.20 Suppose that $S(x) = S^*x$ is a linear sampling operator and \mathcal{X} is a subspace, spanned by vectors $\{x_\ell\}_{\ell=1}^k$. To compute the lower bound in the proposition we need to examine the dimension of $\mathcal{N}((\partial S/\partial x)^*)$. In this case, $\partial S/\partial x = S$ so that $\mathcal{N}((\partial S/\partial x)^*) = \mathcal{N}(S^*)$. To achieve the minimal rate of k we require that $\mathcal{N}(S^*)$ is 0 over \mathcal{X} . In other words, the $N \times k$ matrix whose (n, k) entry is $\langle s_n, x_k \rangle$ should have an empty null space, where $\{s_n\}_{n=1}^N$ are the sampling vectors.

If S is linear but \mathcal{X} is not contained in any finite-dimensional subspace, then sampling at the rate of innovation necessitates that the sampling vectors $\{s_n\}_{n=1}^N$ be linearly independent. Indeed, if $\{s_n\}_{n=1}^N$ are linearly dependent, then there exists an index j such that $s_j = \sum_{n \neq j} a_n s_n$ for some coefficients $\{a_n\}_{n \neq j}$. Consequently, the sample c_j can be expressed in terms of the other samples as $c_j = \langle x, s_j \rangle = \sum_{n \neq j} \bar{a}_n \langle x, s_n \rangle = \sum_{n \neq j} \bar{a}_n c_n$ and thus can be disregarded.

Example 15.21 Suppose that one of the measurements produced by the sensing device, say c_1 , is the energy $0.5\|x\|^2$ of x . In this case $(\partial c_1/\partial x)|_{x_1} = x_1$. Consequently, from Proposition 15.7, sampling at the minimal rate is impossible if the set of signals \mathcal{X} contains the signal $x_1 = 0$. The intuition here follows from the observation that small perturbations in x around the signal $x_1 = 0$ do not show in c_1 . Therefore, if the input to our sampling device happens to be $x = 0$ in this setting,

then sampling is unavoidably unstable, as the left-hand side of condition (15.173) cannot hold.

Throughout the rest of our derivations we focus on the case in which $N = k$ samples of $x(t)$ are obtained with an operator S satisfying

$$\mathcal{N}\left(\frac{\partial S}{\partial x}\Big|_{x_1}\right)^* = \{\mathbf{0}\}, \quad \forall x_1 \in \mathcal{X}. \quad (15.180)$$

This corresponds to sampling at the rate of innovation.

15.6.3 Least-squares recovery

Suppose we want to recover a signal $x = h(\boldsymbol{\theta}_0) \in L_2$ from its samples $\mathbf{c} = S(x)$, where $\boldsymbol{\theta}_0 \in \mathbb{R}^k$ is an unknown parameter vector and $S : L_2 \rightarrow \mathbb{R}^k$ is a given sampling operator. To address this problem, it is natural to seek the minimizer of the function

$$\varepsilon(\boldsymbol{\theta}) = \frac{1}{2} \|S(h(\boldsymbol{\theta})) - \mathbf{c}\|^2 = \frac{1}{2} \|\hat{\mathbf{c}}(\boldsymbol{\theta}) - \mathbf{c}\|^2, \quad (15.181)$$

where we defined $\hat{\mathbf{c}}(\boldsymbol{\theta}) = S(h(\boldsymbol{\theta}))$. The reasoning behind this choice follows from the following observation:

Proposition 15.8. *Suppose that the function $h : \mathbb{R}^k \rightarrow L_2$ satisfies (15.171) and that the operator $S : L_2 \rightarrow \mathbb{R}^k$ satisfies (15.173). Then $\boldsymbol{\theta}_0$ is the unique global minimizer of $\varepsilon(\boldsymbol{\theta})$.*

Proof: Clearly, $\varepsilon(\boldsymbol{\theta}) \geq 0$ for every $\boldsymbol{\theta} \in \mathbb{R}^k$ and $\varepsilon(\boldsymbol{\theta}_0) = 0$, so that $\boldsymbol{\theta}_0$ is a global minimizer of $\varepsilon(\boldsymbol{\theta})$. This minimizer is unique since, owing to (15.171) and (15.173), $\varepsilon(\boldsymbol{\theta}) \geq \alpha_s \alpha_h \|\boldsymbol{\theta} - \boldsymbol{\theta}_0\|$ so that $\varepsilon(\boldsymbol{\theta}) > 0$ for every $\boldsymbol{\theta} \neq \boldsymbol{\theta}_0$. \square

The LS criterion (15.181) is also plausible when the samples \mathbf{c} correspond to a perturbation of the true sample vector by white Gaussian noise. In this case, the minimizer of (15.181) is a maximum-likelihood estimate of $\boldsymbol{\theta}$ from \mathbf{c} .

Unfortunately, the function $\varepsilon(\boldsymbol{\theta})$ is generally nonconvex and might possess many local minima. It therefore seems that standard optimization techniques may fail in finding its global minimizer $\boldsymbol{\theta}_0$. However, as we show next, when sampling at the rate of innovation, assumptions (15.171) and (15.173) guarantee that $\boldsymbol{\theta}_0$ is the unique stationary point of $\varepsilon(\boldsymbol{\theta})$. Thus, any algorithm designed to trap a stationary point necessarily converges to the true parameter vector $\boldsymbol{\theta}_0$.

Theorem 15.3. *Suppose that the function $h : \mathbb{R}^k \rightarrow L_2$ satisfies (15.171), the operator $S : L_2 \rightarrow \mathbb{R}^k$ satisfies (15.173) and its Fréchet derivative $\partial S / \partial x$ satisfies (15.180). Then $\nabla \varepsilon(\boldsymbol{\theta}_1) = \mathbf{0}$ only if $\boldsymbol{\theta}_1 = \boldsymbol{\theta}_0$.*

Proof: The gradient $\nabla \varepsilon(\boldsymbol{\theta}_1)$ is given by

$$\nabla \varepsilon(\boldsymbol{\theta}_1) = \left(\frac{\partial \hat{\mathbf{c}}}{\partial \boldsymbol{\theta}} \Big|_{\boldsymbol{\theta}_1} \right)^* (\hat{\mathbf{c}}(\boldsymbol{\theta}_1) - \mathbf{c}). \quad (15.182)$$

We showed in the proof of Proposition 15.7 that $\mathcal{R}(\partial\hat{\mathbf{c}}/\partial\boldsymbol{\theta}|_{\boldsymbol{\theta}_1}) = \mathbb{R}^k$. Since here $\partial\hat{\mathbf{c}}/\partial\boldsymbol{\theta}|_{\boldsymbol{\theta}_1}$ is a $k \times k$ matrix, it follows that

$$\mathcal{N}\left(\frac{\partial\hat{\mathbf{c}}}{\partial\boldsymbol{\theta}}\Big|_{\boldsymbol{\theta}_1}\right)^* = \mathcal{R}\left(\frac{\partial\hat{\mathbf{c}}}{\partial\boldsymbol{\theta}}\Big|_{\boldsymbol{\theta}_1}\right)^\perp = \{\mathbf{0}\}, \quad (15.183)$$

so that $\nabla\varepsilon(\boldsymbol{\theta}_1) = \mathbf{0}$ only if $\hat{\mathbf{c}}(\boldsymbol{\theta}_1) - \mathbf{c} = \mathbf{0}$. This, by Proposition 15.8, happens only when $\boldsymbol{\theta}_1 = \boldsymbol{\theta}_0$, completing the proof. \square

The importance of Theorem 15.3 lies in the fact that it provides a unified mechanism for recovering FRI signals from samples taken at the rate of innovation. That is, rather than developing a different algorithm for every choice of signal family and sampling method, we can employ the same general-purpose optimization technique to find the stationary point of (15.181).

15.6.4 Iterative recovery

There are many optimization algorithms that can be used to find the stationary point of the objective function $\varepsilon(\boldsymbol{\theta})$ over \mathcal{A} . For simplicity, we focus here on unconstrained optimization methods that are designed for the case in which $\mathcal{A} = \mathbb{R}^k$. This does not limit the generality of the discussion since if $\mathcal{A} \neq \mathbb{R}^k$, then the constrained problem $\min_{\boldsymbol{\theta} \in \mathcal{A}} \varepsilon(\boldsymbol{\theta})$ can be transformed into the unconstrained problem $\min_{\tilde{\boldsymbol{\theta}} \in \mathbb{R}^k} \varepsilon(p(\tilde{\boldsymbol{\theta}}))$, where $p : \mathbb{R}^k \rightarrow \mathcal{A}$ is bijective. The latter problem possesses a unique stationary point $\tilde{\boldsymbol{\theta}}_0 = p^{-1}(\boldsymbol{\theta}_0)$. Therefore, once $\tilde{\boldsymbol{\theta}}_0$ is determined, the desired solution is $\boldsymbol{\theta}_0 = p(\tilde{\boldsymbol{\theta}}_0)$.

Example 15.22 To show how any constrained model can be converted into an unconstrained one, consider the stream of pulses (15.5) under the condition that $a_\ell > a > 0$ and $T_{\min} < t_\ell - t_{\ell-1} < T_{\max}$ with $0 < T_{\min} \leq T_{\max} < \infty$.

Define

$$\tilde{\theta}_m^{\text{Li}} = \ln(a_m - a_0), \quad \tilde{\theta}_m^{\text{N}} = \tan\left(\pi \frac{t_m - t_{m-1} - \bar{T}}{\Delta}\right), \quad (15.184)$$

where $\bar{T} = (T_{\max} + T_{\min})/2$ and $\Delta = T_{\max} - T_{\min}$. Here $\tilde{\theta}_m^{\text{Li}}$ denotes the linear parameters and $\tilde{\theta}_m^{\text{N}}$ the nonlinear parameters. Then,

$$a_m = e^{\tilde{\theta}_m^{\text{Li}}} + a_0, \quad t_m = t_0 + m\bar{T} + \frac{\Delta}{\pi} \sum_{i=1}^m \arctan\left(\tilde{\theta}_i^{\text{N}}\right). \quad (15.185)$$

With this choice, the set \mathcal{X} of all feasible signals is obtained by varying $\tilde{\boldsymbol{\theta}}^{\text{Li}}$ and $\tilde{\boldsymbol{\theta}}^{\text{N}}$ over the entire space \mathbb{R}^L and not over some subset of \mathbb{R}^L .

As we discussed in Section 8.4.4, many unconstrained optimization methods start with an initial guess $\boldsymbol{\theta}^0$ and perform iterations of the form

$$\boldsymbol{\theta}^{\ell+1} = \boldsymbol{\theta}^\ell - \gamma^\ell \mathbf{B}^\ell \nabla \varepsilon(\boldsymbol{\theta}^\ell), \quad (15.186)$$

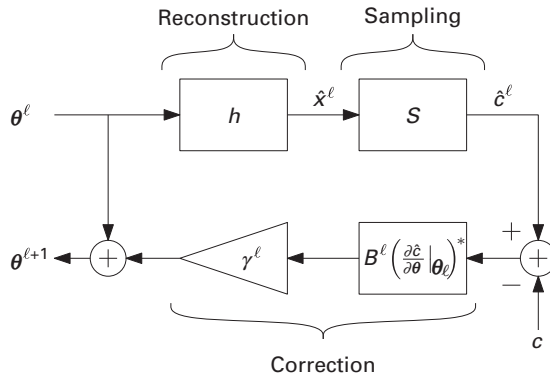


Figure 15.47 Schematic interpretation of one iteration of (15.186).

where γ^ℓ is a scalar step size obtained by means of a one dimensional search and \mathbf{B}^ℓ is a positive definite matrix. Owing to the structure of $\nabla \varepsilon(\theta^\ell)$ in our case (see (15.182)), the iterations (15.186) can be given a simple interpretation, as shown in Fig. 15.47. Specifically, at the ℓ th iteration, the current guess θ^ℓ of the parameters θ is used to construct our estimate \hat{x}^ℓ of the signal x by applying the function h . This approximation is then sampled using the operator S to obtain an estimated sample vector \hat{c}^ℓ . Finally, the difference between \hat{c}^ℓ and the samples c is multiplied by a correction matrix and added to θ^ℓ to yield the updated approximation $\theta^{\ell+1}$.

In our setting, the objective function $\varepsilon(\theta)$ is bounded from below. The iterations (15.186) are therefore guaranteed to converge to a stationary point of $\varepsilon(\theta)$ if the following conditions hold: γ^ℓ is chosen to satisfy the Wolfe conditions (see Section 8.4.4 for more details), \mathbf{B}^ℓ satisfies

$$\frac{\langle \mathbf{B}^\ell \nabla \varepsilon(\theta^\ell), \nabla \varepsilon(\theta^\ell) \rangle}{\| \mathbf{B}^\ell \nabla \varepsilon(\theta^\ell) \| \| \nabla \varepsilon(\theta^\ell) \|} > \delta \quad (15.187)$$

for some constant $\delta > 0$ independent of ℓ , and the gradient $\nabla \varepsilon(\theta)$ is Lipschitz-continuous in an environment of the level set $\mathcal{N} = \{ \theta : \varepsilon(\theta) \leq \varepsilon(\theta^0) \}$ [182].

A step size satisfying the Wolfe conditions can be found by using the backtracking method presented in Algorithm 15.8 (this algorithm is identical to Algorithm 8.3 introduced in the context of nonlinear sampling). Equation (15.187) is trivially satisfied with $\mathbf{B}^\ell = \mathbf{I}$, which corresponds to steepest-descent iterations. It can be shown (see [462] and Section 8.4.4) that this condition also holds for $\mathbf{B}^\ell = ((\partial \hat{c} / \partial \theta |_{\theta^\ell})^* (\partial \hat{c} / \partial \theta |_{\theta^\ell}))^{-1}$ if

$$\| h(\theta_1) - h(\theta_2) \|_{L_2} \leq \beta_h \| \theta_1 - \theta_2 \| \quad (15.188)$$

for some $\beta_h < \infty$ and for all $\theta_1, \theta_2 \in \mathcal{N}$. This choice belongs to the class of quasi-Newton methods, which typically converge much faster than steepest descent. Finally, it is shown in [462] that a sufficient condition for $\nabla \varepsilon(\theta)$ to be Lipschitz-continuous over \mathcal{N} is that the derivative of h is Lipschitz-continuous there.

Algorithm 15.8 Backtracking line search

```

set  $\mathbf{g}^\ell = \nabla \varepsilon(\boldsymbol{\theta}^\ell)$ ,  $\mathbf{d}^\ell = -\mathbf{B}^\ell \mathbf{g}^\ell$ ,  $\delta = 1$  and  $\rho, \eta \in (0, 1)$ 
while  $\varepsilon(\boldsymbol{\theta}^\ell + \delta \mathbf{d}^\ell) > \varepsilon(\boldsymbol{\theta}^\ell) + \eta \delta \langle \mathbf{d}^\ell, \mathbf{g}^\ell \rangle$  do
     $\delta \leftarrow \rho \delta$ 
end while
return  $\gamma^\ell = \delta$ 
```

To summarize, we have the following result.

Theorem 15.4. Suppose that the function $h : \mathbb{R}^k \rightarrow L_2$ satisfies (15.171), its Fréchet derivative $\partial h / \partial \boldsymbol{\theta}$ is Lipschitz-continuous over $\mathcal{N} = \{\boldsymbol{\theta} : \varepsilon(\boldsymbol{\theta}) \leq \varepsilon(\boldsymbol{\theta}^0)\}$, the operator $S : L_2 \rightarrow \mathbb{R}^k$ satisfies (15.173) and its Fréchet derivative $\partial S / \partial x$ satisfies (15.180). Consider the iterations (15.186), where the step size γ^ℓ is obtained via Algorithm 15.8 and let $\hat{\mathbf{c}}(\boldsymbol{\theta}) = S(h(\boldsymbol{\theta}))$. Then each of the following options guarantees that $\boldsymbol{\theta}^\ell \rightarrow \boldsymbol{\theta}_0$:

1. $\mathbf{B}^\ell = \mathbf{I}$.
2. $\mathbf{B}^\ell = ((\partial \hat{\mathbf{c}} / \partial \boldsymbol{\theta}|_{\boldsymbol{\theta}^\ell})^*)^{-1}$ and condition (15.188) holds.

We now consider an application of this approach to recovery of pulse streams from nonlinear samples. Further examples can be found in [462].

Example 15.23 Consider the case in which $x(t)$ is given by (15.5). We transform the parameters using the transformation defined by (15.184) in Example 15.22. The constraints we assume on the parameters correspond to $a = 0.1$, $T_{\min} = 0.3$, $T_{\max} = 0.7$ and $t_0 = -0.3$. Our goal is to recover the signal parameters from the samples (15.172), where $\{s_n(t)\}_{n=1}^N$ are sampling kernels in $L_2([0, \tau])$ and $f(\cdot)$ is a nonlinear response function. In this example, we choose $s_n(t) = s(t - T_0 - nT_s)$ with $T_0 = Ts/2$, $T_s = \tau/N$ so that the sampling functions span the entire observation segment $[0, \tau]$. The pulse shape $h(t)$ and the sampling filter $s(t)$ are taken to be Gaussian functions with variances $\sigma_g^2 = 0.05$ and $\sigma_s^2 = 0.1$, respectively. The nonlinear response curve was set to be $f(c) = 100 \arctan(0.01c)$.

To apply the quasi-Newton or steepest-decent methods, we note that, with the transformation $\boldsymbol{\theta} = p(\tilde{\boldsymbol{\theta}})$ of (15.185),

$$\frac{\partial \hat{\mathbf{c}}}{\partial \tilde{\boldsymbol{\theta}}} = \frac{\partial \hat{\mathbf{c}}}{\partial \boldsymbol{\theta}} \frac{\partial p}{\partial \tilde{\boldsymbol{\theta}}}. \quad (15.189)$$

Explicit computation shows that

$$\frac{\partial \hat{\mathbf{c}}}{\partial \boldsymbol{\theta}} = \mathbf{C} (\mathbf{A} \mathbf{B}) \quad (15.190)$$

with

$$\mathbf{A} = \begin{pmatrix} -a_1 \langle g'(t - t_1), s_1 \rangle & \cdots & -a_L \langle g'(t - t_L), s_1 \rangle \\ \vdots & & \vdots \\ -a_1 \langle g'(t - t_1), s_N \rangle & \cdots & -a_L \langle g'(t - t_L), s_N \rangle \end{pmatrix}, \quad (15.191)$$

$$\mathbf{B} = \begin{pmatrix} \langle g(t - t_1), s_1 \rangle & \cdots & \langle g(t - t_L), s_1 \rangle \\ \vdots & & \vdots \\ \langle g(t - t_1), s_N \rangle & \cdots & \langle g(t - t_L), s_N \rangle \end{pmatrix} \quad (15.192)$$

and

$$\mathbf{C} = \text{diag}(f'(\langle x, s_1 \rangle) \cdots f'(\langle x, s_N \rangle)). \quad (15.193)$$

Furthermore,

$$\frac{\partial p}{\partial \tilde{\boldsymbol{\theta}}} = \begin{pmatrix} \mathbf{D} & \mathbf{0} \\ \mathbf{0} & \mathbf{E} \end{pmatrix} \quad (15.194)$$

with

$$\mathbf{D} = \text{diag}\left(e^{\tilde{\theta}_1} \cdots e^{\tilde{\theta}_M}\right) \quad (15.195)$$

and

$$\mathbf{E} = \frac{\Delta}{\pi} \begin{pmatrix} \frac{1}{1+\tilde{\theta}_{M+1}^2} & 0 & \cdots & 0 \\ \frac{1}{1+\tilde{\theta}_{M+1}^2} & \frac{1}{1+\tilde{\theta}_{M+2}^2} & \cdots & 0 \\ \vdots & \vdots & \ddots & \vdots \\ \frac{1}{1+\tilde{\theta}_{M+1}^2} & \frac{1}{1+\tilde{\theta}_{M+2}^2} & \cdots & \frac{1}{1+\tilde{\theta}_{2M}^2} \end{pmatrix}. \quad (15.196)$$

Figure 15.48 demonstrates the convergence of the Newton iterations for recovering $L = 2$ pulses over the period $[0, 1]$ from $N = 4$ samples, which is equal to the rate of innovation. The solid lines represent the true pulses while the dashed lines denote the estimated pulses. Note that all inner products in (15.191) and (15.192) can be computed analytically at every iteration. The true parameters in this experiment were $t_1 = 0.2$, $t_2 = 0.8$, $a_1 = 1$ and $a_2 = 5$. As shown in Fig. 15.48(a), the iterations were initialized at $t_1 = 1/3$, $t_2 = 2/3$, and $a_1 = a_2 = 3$. The estimated samples at this point, shown in “ \times ”-marks, deviate substantially from the true samples, marked with circles. However, this gap decreases quickly in the first 15 iterations (see Fig 15.48(b)) and almost completely vanishes after 30 iterations (Fig 15.48(c)). Figure 15.48(d) shows the rapid decrease in the LS objective (15.181) as a function of the iterations.

Figure 15.49 demonstrates the behavior of the algorithm in the presence of noise. The setting here is the same as that of Fig. 15.48 with the distinction that white Gaussian noise is added to the samples prior to recovery. This figure depicts the MSE as a function of the SNR. The solid line corresponds to the CRB. As can be seen, the MSE of our method coincides with the CRB in high SNR scenarios and outperforms it at low SNR levels. This is a result of the fact that our technique is biased.

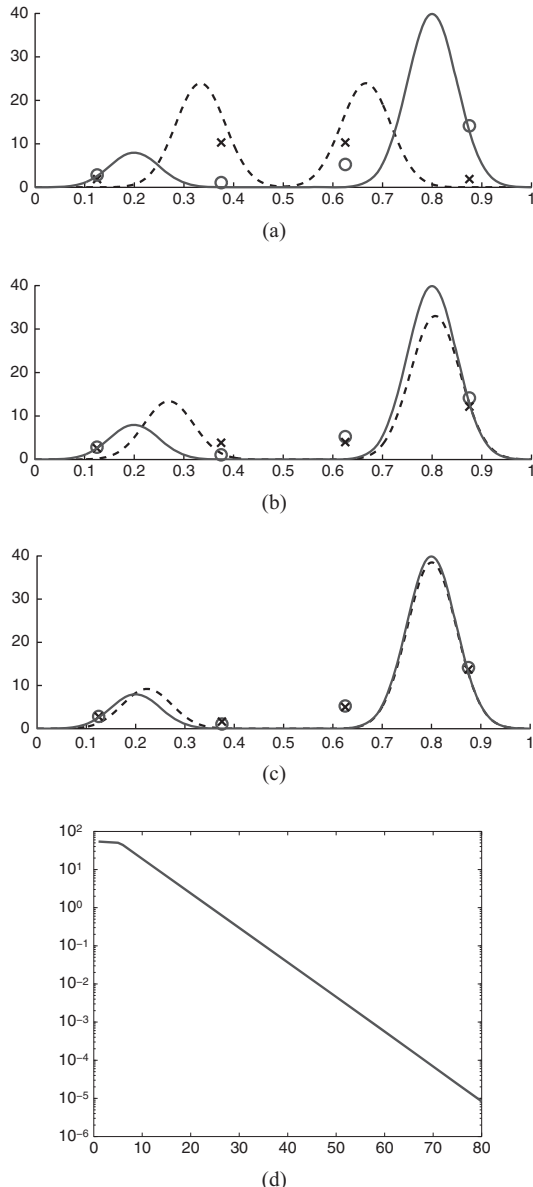


Figure 15.48 Convergence of Newton iterations for pulse stream recovery. (a) Initialization. (b) 15th iteration. (c) 30th iteration. (d) LS objective value as a function of the iterations.

15.7

Applications of FRI

In this section we discuss two applications of the pulse-stream models we studied in this chapter to radar and ultrasound imaging. These applications are treated in detail in [429, 430, 431, 432, 435, 453].

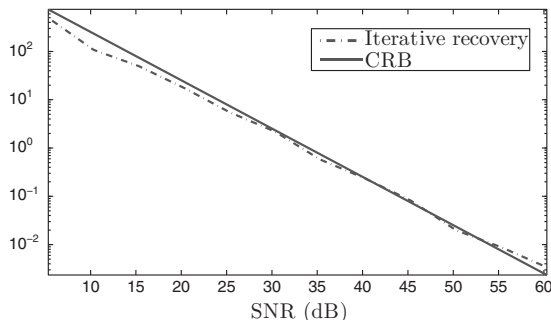


Figure 15.49 MSE as a function of SNR for pulse stream recovery in the setting of Fig. 15.48.

There are a myriad of other possible settings in which FRI modeling can play an important role. One example is image super-resolution, which is considered in [466]. Another interesting application is to signal compression [467]. Other examples include ultra-wideband communications [468], and neuroscience [469]. Many of the ideas presented here have also been extended to multidimensional FRI signals [470, 471].

15.7.1 Sub-Nyquist radar

We begin by applying FRI theory to a pulse-Doppler-based radar system following the ideas in [431]. As we show below, identifying targets' distance and closing velocity in such a radar system becomes equivalent to time-delay and (complex) amplitude estimation from pulse streams. Using the FRI framework together with appropriate processing, referred to as *Doppler focusing* below, will allow one to sample and process radar signals at rates far below Nyquist. Furthermore, Doppler focusing enjoys an optimal SNR improvement which scales linearly with the number of pulses, obtaining good detection performance even at SNR as low as -25 dB.

Radar model

Consider a radar system that detects targets by transmitting a periodic stream of pulses and processing its reflections. The transmitted signal consists of P equally spaced pulses $h(t)$:

$$x_T(t) = \sum_{p=0}^{P-1} h(t - p\tau), \quad 0 \leq t \leq P\tau. \quad (15.197)$$

The pulse-to-pulse delay τ is referred to as the pulse repetition interval (PRI). The entire span of the signal in (15.197) is called the coherent processing interval (CPI). The pulse $h(t)$ is a known time-limited baseband function with CTFT $H(\omega)$ that has negligible energy at frequencies beyond $B_h/2$.

The target scene is composed of L nonfluctuating point targets (Swerling 0 model; see [472, 473]). The pulses reflect off the L targets and propagate back to the transceiver. Each target ℓ is defined by three parameters:

1. A time delay $\tau_\ell = 2r_\ell/c$, proportional to the target's distance from the radar r_ℓ , where c is the speed of light.
2. A Doppler radial frequency $\nu_\ell = 2\dot{r}_\ell f_c/c$, proportional to the target–radar closing velocity, namely, the target's velocity radial component \dot{r}_ℓ , and the radar's carrier frequency f_c .
3. A complex amplitude α_ℓ , proportional to the target's radar cross-section, dispersion attenuation and all other propagation factors.

In order to simplify the received signal model, we make the following assumptions on the targets' location and motion:

1. Far targets: target–radar distance is large compared with the distance change during the CPI which allows for constant α_ℓ within the CPI:

$$\dot{r}_\ell P\tau \ll r_\ell \Rightarrow \nu_\ell \ll \frac{f_c \tau_\ell}{P\tau}. \quad (15.198)$$

2. Slow targets: low target velocity allows for constant τ_ℓ during the CPI and constant Doppler phase during pulse time. This condition holds when the baseband Doppler frequency is smaller than the frequency resolution:

$$\frac{2\dot{r}_\ell B_h}{c} \ll \frac{1}{P\tau} \Rightarrow \nu_\ell \ll \frac{f_c}{P\tau B_h}. \quad (15.199)$$

3. Small acceleration: target velocity remains approximately constant during the CPI allowing for constant ν_ℓ . This condition is satisfied when the velocity change induced by acceleration is smaller than the velocity resolution:

$$\ddot{r}_\ell P\tau \ll \frac{c}{2f_c P\tau} \Rightarrow \ddot{r}_\ell \ll \frac{c}{2f_c (P\tau)^2}. \quad (15.200)$$

Although these assumptions may seem hard to comply with, they all rely on slow enough relative motion between the radar and its targets. Radar systems tracking people, ground vehicles and sea vessels usually comply quite easily, as we illustrate in the following example.

Example 15.24 Consider a $P = 100$ pulse radar system with PRI $\tau = 100 \mu\text{sec}$, bandwidth $B_h = 30 \text{ MHz}$ and carrier frequency $f_c = 3 \text{ GHz}$, tracking cars traveling up to $\dot{r}_\ell = 120 \text{ km/hour}$. To compute the maximal distance change over the CPI we note that $\dot{r}_\ell = 33.3 \text{ m/sec}$. Therefore, the maximal distance change over the observation interval is 0.33 m. If the target's minimal distance from the radar is a few meters, then assumption (1) is satisfied. As for (2), the maximal Doppler frequency is given by $2\dot{r}_\ell f_c/c = 667 \text{ Hz}$, which is much smaller than $f_c/P\tau B_h = 10 \text{ kHz}$. An extreme acceleration of 10 m/sec^2 would cause a velocity change of 0.1 m/sec over the CPI, easily satisfying (3).

Under these three assumptions, we can write the received signal as

$$x_R(t) = \sum_{p=0}^{P-1} \sum_{\ell=0}^{L-1} \alpha_\ell h(t - \tau_\ell - p\tau) e^{-j\nu_\ell p\tau}. \quad (15.201)$$

It will be convenient to express the signal as a sum of single frames:

$$x_R(t) = \sum_{p=0}^{P-1} x_p(t), \quad (15.202)$$

where

$$x_p(t) = \sum_{\ell=0}^{L-1} \alpha_\ell h(t - \tau_\ell - p\tau) e^{-j\nu_\ell p\tau}. \quad (15.203)$$

In reality $x_R(t)$ will be contaminated by additive noise. We will take this into account in the simulations below.

Our goal is to sample the received signal at sub-Nyquist rates and to reconstruct the $3L$ parameters $\{\tau_\ell, \nu_\ell, \alpha_\ell\}$, with $0 \leq \ell \leq L - 1$. Estimating τ_ℓ and ν_ℓ will enable approximation of each target's distance and closing velocity, as demonstrated in Fig. 15.50. The targets in Fig. 15.50 can be equivalently represented by a delay–Doppler map, where each target is marked by its delay (proportional to its distance) and its Doppler frequency (proportional to the radial velocity), as shown in Fig. 15.51.

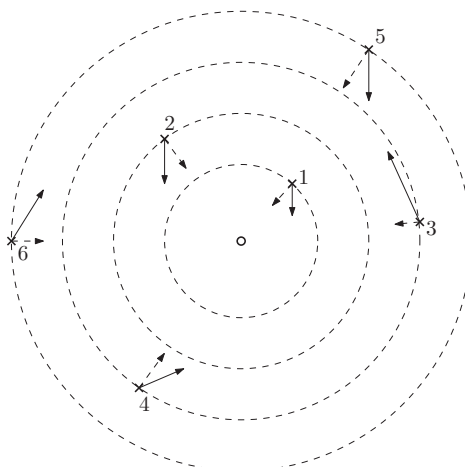


Figure 15.50 Illustration of $L = 6$ point targets in space. Each target, denoted by a cross, is located at a specific distance from the radar and moving at an unknown velocity (continuous vector). The closing velocity of each target is denoted by the dashed vectors. Our goal is to sample the received signal at the radar (in the center) at sub-Nyquist rates and to reconstruct the distance and radial velocity of each target.

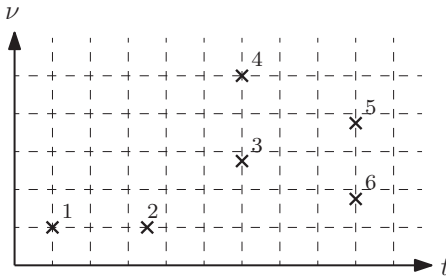


Figure 15.51 The targets of Fig. 15.50 represented by a delay–Doppler map.

Classic sampling

Before describing our proposed sub-Nyquist processing, we review classic methods for radar processing, which typically consists of the following stages [472, 473]:

1. **ADC:** Sample each incoming frame $x_p(t)$ at its Nyquist rate B_h , equal to the bandwidth of $h(t)$, creating $x_p[n]$, $0 \leq n < N$, where $N = \tau B_h$. We assume for simplicity that N is an integer.
2. **Matched filter:** Apply a standard matched filter on each frame $x_p[n]$, as explained in Section 15.2.1. This results in the outputs $y_p[n] = x_p[n] * \bar{h}[-n]$, where $h[n]$ is the sampled version of the transmitted pulse $h(t)$, at its Nyquist rate.
3. **Doppler processing:** For each discrete time index n , perform a P -point DFT along the pulse dimension, namely, $z_n[k] = \text{DFT}_P\{y_p[n]\} = \sum_{p=0}^{P-1} y_p[n] e^{-j2\pi pk/P}$ for $0 \leq k < P$.
4. **Delay–Doppler map:** Stacking the vectors z_n , and taking absolute value, we obtain a delay–Doppler map $\mathbf{Z} = \text{abs}[\mathbf{z}_0, \dots, \mathbf{z}_{N-1}] \in \mathbb{R}^{P \times N}$.
5. **Peak detection:** A heuristic detection process, where knowledge of number of targets, target power, clutter location, etc. may help in discovering target positions. For example, if we know there are L targets, then we can choose the L strongest points in the map.

This process is illustrated in Fig. 15.52.

The classic processing described above requires sampling the received signal at its Nyquist rate B_h , which can be hundreds of MHz and even up to several GHz. The required computational power is P convolutions of a signal of length $N = \tau B_h$ and N FFTs of length P – both also proportional to B_h . Using the FRI framework leads to low-rate sampling and processing of radar signals, regardless of their bandwidth.

Doppler focusing

Doppler focusing is a processing technique, suggested in [431], which uses target echoes from different pulses to create a single superimposed pulse focused at a particular Doppler frequency. The techniques suggested in this chapter can then be used to recover the corresponding delays. This method results in an optimal SNR boost, and

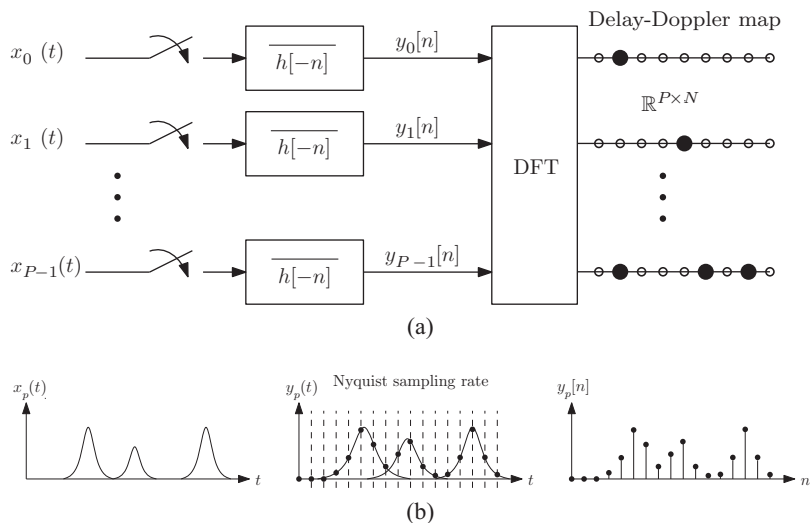


Figure 15.52 Classic processing of radar signals. (a) Each period of the signal is sampled at its Nyquist rate, followed by pulse-matched filtering. Doppler processing then consists of performing a DFT followed by peak detection in the delay–Doppler map. (b) Creating one of the frames $y_p[n]$.

can be carried out in the frequency domain, thus enabling sub-Nyquist sampling and processing with the same SNR increase as matched filtering.

We can view the output of Doppler processing as a discrete equivalent of the following time shift and modulation operation on the received signal:

$$\Phi(t; \nu) = \sum_{p=0}^{P-1} x_p(t + p\tau) e^{j\nu p\tau} = \sum_{\ell=0}^{L-1} \alpha_\ell h(t - \tau_\ell) \sum_{p=0}^{P-1} e^{j(\nu - \nu_\ell)p\tau}, \quad (15.204)$$

where we used (15.203). Consider the sum $g(\nu|\nu_\ell) = |\sum_{p=0}^{P-1} e^{j(\nu - \nu_\ell)p\tau}|$. For any given ν , targets with Doppler frequency ν_ℓ in a band of width $2\pi/P\tau$ around ν will achieve coherent integration and a SNR boost of approximately

$$g(\nu|\nu_\ell) = \left| \sum_{p=0}^{P-1} e^{j(\nu - \nu_\ell)p\tau} \right| \stackrel{|\nu - \nu_\ell| < \pi/P\tau}{\cong} P. \quad (15.205)$$

On the other hand, since the sum of P equally spaced points covering the unit circle is generally close to zero, targets with ν_ℓ not “in focus” will approximately cancel out. We can therefore estimate the sum of exponents in (15.204) as

$$\Phi(t; \nu) \cong P \sum_{\ell \in \Lambda(\nu)} \alpha_\ell h(t - \tau_\ell) \quad (15.206)$$

where $\Lambda(\nu) = \{\ell : |\nu - \nu_\ell| < \pi/P\tau\}$. In other words, the sum is only over the targets whose Doppler shift’s are in the range $|\nu - \nu_\ell| < \pi/P\tau$.

For each Doppler frequency ν , $\Phi(t; \nu)$ represents a standard pulse-stream model where the problem is to estimate the unknown delays. Thus, using Doppler focusing,

we have reduced our problem to delay-only estimation for a small range of Doppler frequencies, with increased SNR by a factor of P . We have seen throughout this chapter that the delays can be found from low-rate samples that are equivalent to a small set of Fourier coefficients. We therefore show next how we can perform Doppler focusing directly on these low-rate samples by viewing Doppler focusing in the frequency domain.

Suppose that we sample m values of $x_R(t)$ over each period τ , such that we obtain m Fourier coefficients $c_p[k]$, $k \in \mathcal{K}$. Here \mathcal{K} are the chosen Fourier frequencies with $|\mathcal{K}| = m$, and $c_p[k]$ is the Fourier series of the p th frame which can be obtained by replacing $t \rightarrow t + p\tau$ and $\alpha_\ell \rightarrow \alpha_\ell e^{-j\nu_\ell p\tau}$ in (15.25):

$$c_p[k] = \frac{1}{\tau} H(2\pi k/\tau) \sum_{l=0}^{L-1} \alpha_\ell e^{-j\nu_\ell p\tau} e^{-j2\pi k\tau_\ell/\tau}. \quad (15.207)$$

Performing the Doppler focusing operation results in

$$\Psi_\nu[k] = \sum_{p=0}^{P-1} c_p[k] e^{j\nu p\tau} = \frac{1}{\tau} H(2\pi k/\tau) \sum_{l=0}^{L-1} \alpha_\ell e^{-j2\pi k\tau_\ell/\tau} \sum_{p=0}^{P-1} e^{j(\nu - \nu_\ell)p\tau}. \quad (15.208)$$

Note that $\Psi_\nu[k]$ is the Fourier series of $\Phi(t; \nu)$ with respect to t . Following the same arguments as in (15.205), for any target ℓ satisfying $|\nu - \nu_\ell| < \pi/P\tau$, we have

$$\Psi_\nu[k] \cong \frac{P}{\tau} H(2\pi k/\tau) \sum_{\ell \in \Lambda(\nu)} \alpha_\ell e^{-j2\pi k\tau_\ell/\tau}. \quad (15.209)$$

In [431] it is shown that in the presence of white noise on $x_R(t)$, Doppler focusing achieves an increase in SNR by a factor of P . It is also proven that this approach can operate at the minimal possible sampling rate for recovering the radar's parameters. Finally, an additional advantage of Doppler focusing is its ability to deal with certain models of clutter and target dynamic range, by adding a simple windowing operation in the sum (15.208).

Equation (15.209) is identical in form to (15.25) except it is scaled by P . Thus, for each ν , we now have a standard delay estimation problem, as treated throughout the chapter. Note, however, that improved performance can be obtained by jointly processing the sequences $\{\Psi_\nu[k]\}$ for different values of ν , since we know that there are at most L targets over all possible ν . Thus, instead of searching separately for each of the delays $\tau_\ell, \ell \in \Lambda(\nu)$, we can estimate the L delays by joint processing over all Doppler frequencies.

A particularly convenient method in this case is to employ a matching pursuit type approach where we begin by searching for the strongest peak over all ν assuming a single delay. For simplicity we assume that the pulse is flat, or we simply divide the values of $\Psi_\nu[k]$ by $H(2\pi k/\tau)$. We then solve

$$(\hat{t}, \hat{\nu}) = \arg \max_{t, \nu} \left| \sum_{k \in \mathcal{K}} \Psi_\nu[k] e^{j2\pi kt/\tau} \right|. \quad (15.210)$$

Once the optimal values \hat{t} and $\hat{\nu}$ are found, we subtract their influence from the focused sub-Nyquist samples:

$$\Psi'_{\hat{\nu}}[k] = \Psi_{\hat{\nu}}[k] - \frac{1}{\tau} \hat{\alpha}_\ell e^{-j2\pi k\hat{t}/\tau} \sum_{p=0}^{P-1} e^{j(\nu-\hat{\nu}_\ell)p\tau}, \quad (15.211)$$

where

$$\hat{\alpha}_\ell = \frac{\tau}{P|\mathcal{K}|} \sum_{k \in \mathcal{K}} \Psi_{\hat{\nu}}[k] e^{j2\pi k\hat{t}/\tau}. \quad (15.212)$$

We then continue to iterate by finding all the desired L peaks. In practice, the search for peaks can be limited to a grid, which allows to carry out all operations using simple FFT operations (see Section VI.E of [431]).

Example 15.25 In this example we present numerical experiments reported in [431] illustrating the recovery performance of a sparse target scene.

We corrupt the received signal $x_R(t)$ with an additive white Gaussian noise $n(t)$ with power spectral density $N_0/2$, bandlimited to $x(t)$'s bandwidth B_h . We define the signal to noise power ratio for target ℓ as

$$\text{SNR}_\ell = \frac{\frac{1}{T_p} \int_0^{T_p} |\alpha_\ell h(t)|^2 dt}{N_0 B_h}, \quad (15.213)$$

where T_p is the pulse time. The scenario parameters used were $L = 5$ targets, $P = 100$ pulses, a PRI of $\tau = 10 \mu\text{sec}$, and a signal bandwidth $B_h = 200 \text{ MHz}$. Target delays and Doppler frequencies are spread uniformly at random in the appropriate unambiguous regions, and target amplitudes were chosen with constant absolute value and random phase. The classic time and frequency resolutions (Nyquist bins), defined as $1/B_h$ and $1/P\tau$, are 5 nsec and 1 kHz, respectively.

The signal was subsampled at a tenth of the Nyquist rate, resulting in 200 Fourier coefficients per pulse. Doppler focusing was tested with two types of Fourier coefficient sets: a consecutive set and a random set. The performance of Doppler focusing is compared with classic processing using the hit rate, which is defined as the number of correct target detections, where a hit corresponds to a delay–Doppler estimate which is circumscribed by an ellipse around the true target position in the time–frequency plane. We used an ellipse with axes equivalent to ± 3 times the time and frequency Nyquist bins. In both Doppler focusing and classic processing the delay and Doppler frequency region was discretized with uniform steps of half a Nyquist bin. Figure 15.53 demonstrates the hit-rate of the different recovery methods for various SNR values. Doppler focusing with consecutive coefficients tends to perform better under this metric for lower SNR, while choosing coefficients randomly improves performance as SNR increases. As opposed to Doppler-focusing recovery

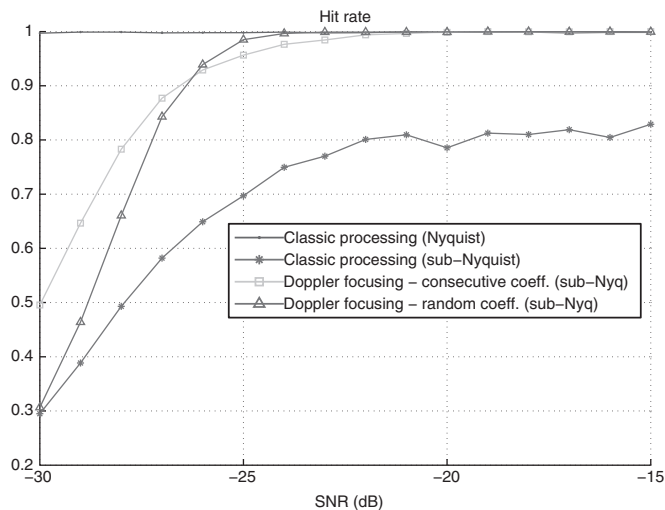


Figure 15.53 Hit Rate for Doppler focusing at one-tenth of the Nyquist rate, and classic processing.

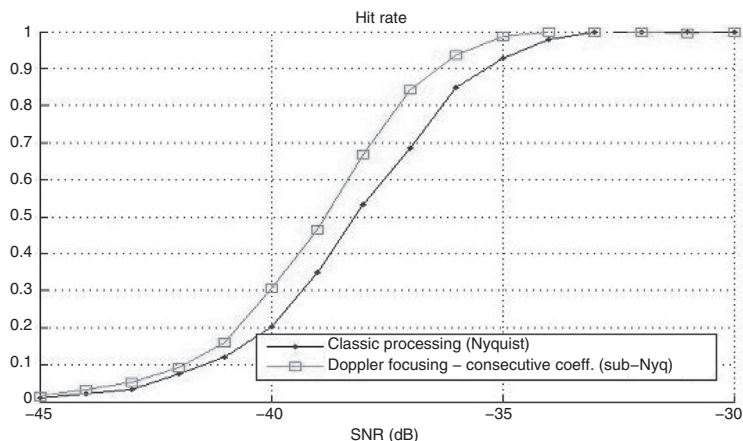


Figure 15.54 Hit rate for classic processing and Doppler focusing at one-tenth the Nyquist rate, where the waveform used for Doppler focusing has its entire energy contents concentrated in the sampled frequencies.

performance which decreases gracefully with sample rate reduction, classic processing suffers significantly when the sampling rate is reduced below Nyquist.

Figure 15.54 shows the same hit-rate graph for classic processing, but this time the waveform used for Doppler focusing had its CTFT adjusted so that energy was transferred from frequencies which were not sampled, to those that were. This was performed by passing the signal through a low-pass filter and rescaling its amplitude so that target SNR (15.213) remains constant. Since Doppler focusing imposes no restrictions on the transmitter, we can use a signal with the same total energy, but

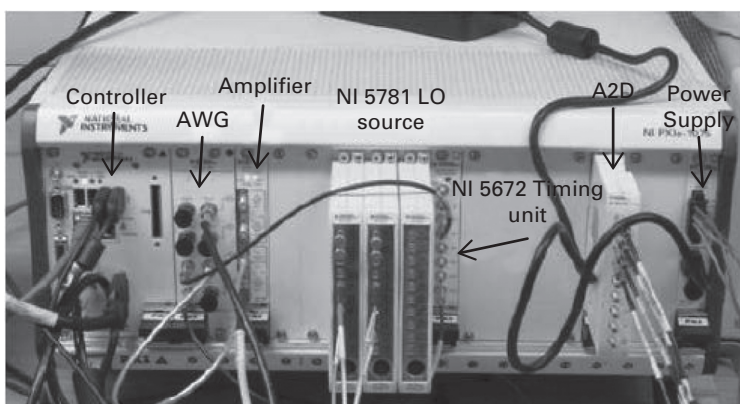


Figure 15.55 The NI chassis.

have it spread out in a manner which is more favorable to the frequency-domain sub-Nyquist sampling, so that signal energy is not lost in sampling. As performance for Doppler focusing improves significantly, excellent recovery results can be obtained at much lower SNR values, surpassing classic processing which uses 10 times as many samples. This shows that the performance degradation caused by sub-Nyquist sampling can be compensated for using a suitable transmitter.

Radar experiment

In [431], the idea of Doppler focusing is used in combination with the sub-Nyquist prototype of Fig. 15.40 in order to demonstrate radar reception at sub-Nyquist rates. The experimental setup is based on national instruments (NI) PXI equipment which is used to synthesize a radar environment and also ensure system synchronization. The entire component ensemble, wrapped in the NI chassis, is depicted in Fig. 15.55. Additional information regarding the system's configuration and synchronization issues can be found in [432].

The experimental process consists of the following steps. We begin by using the applied wave research (AWR) software, which enables us to examine a large variety of scenarios, consisting of different target parameters, i.e. delays, Doppler frequencies, and amplitudes. The AWR software can simulate a complete radar scenario, including pulse transmission and accurate power loss due to wave propagation in a realistic medium. We then use an arbitrary waveform generator (AWG) module to produce an analog signal which is amplified and routed to the radar receiver board of Fig. 15.40. The Nyquist rate of the signal chosen is 30 MHz. The crystal receivers in the filter have a bandwidth of 80 kHz each. Each channel is sampled at a rate of 250 kHz, leading to a total sampling rate of 1 MHz. These samples are fed into the chassis controller and a Matlab function is launched that runs the Doppler focusing reconstruction algorithm. The system contains a fully detailed interface implemented in the LabView environment. Various target scenes, with different target delays, Doppler frequencies and amplitudes, are recovered

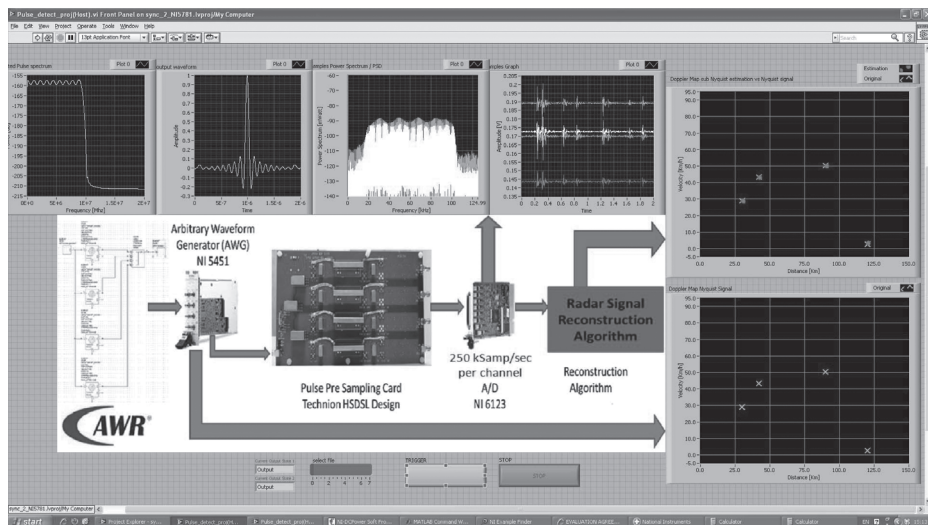


Figure 15.56 The LabView experimental interface. From left to right: $H(\omega)$, $h(t)$, the frequency response of each channel, the four signals detected in each channel; at the top, the reconstructed target scene; at the bottom, the original target scene.

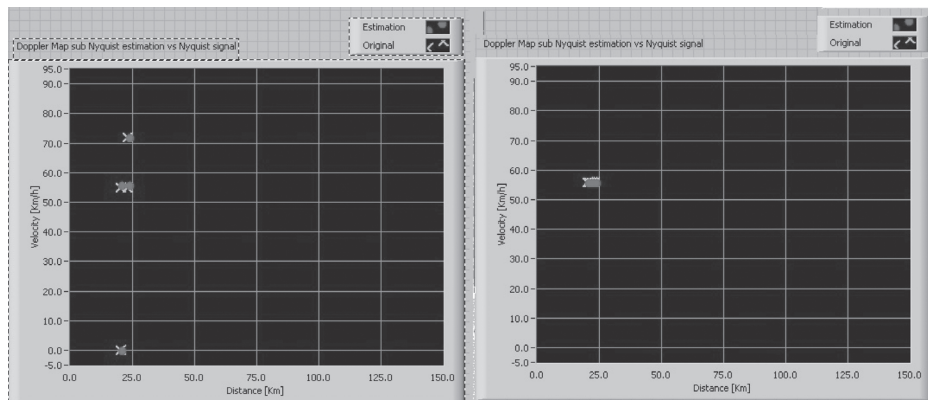


Figure 15.57 Two additional target scenes. On the left, all four targets have closely spaced delays, and two of the targets also have close Doppler frequencies. On the right, all four targets have very similar delays and Doppler frequencies. Doppler focusing based recovery is successful in both cases.

successfully using this setup. Screenshots of the interface are depicted in Figs. 15.56 and 15.57.

This experimental prototype demonstrates that the sub-Nyquist methodology described in this chapter is feasible in practice and can be implemented with standard RF hardware.

Before concluding this application, we note that the ideas presented here can also be extended to the case in which the pulse shape is not known. The path to sub-Nyquist

sampling in this setting is by using the Gabor transform and noting that short radar pulses will have a sparse Gabor representation. These sparse coefficients can be recovered, as in the known pulse case, from a small set of Fourier coefficients. We refer the reader to [474] for details.

15.7.2 Time-varying system identification

The techniques used to treat the radar problem can also be applied to identification of underspread linear systems (ULSs), whose responses lie within a unit-area region in the delay–Doppler space. The importance of this problem stems from the fact that many physical systems can be described as linear and time-varying. The work in relies on FRI theory and algorithms to show that sufficiently underspread parametric linear systems, described by a finite set of delays and Doppler shifts, are identifiable from a single observation as long as the time–bandwidth product of the input signal is proportional to the square of the total number of delay–Doppler pairs in the system.

Mathematically, identification of a given time-varying linear system \mathcal{H} involves probing it with a known input signal $x(t)$ and identifying \mathcal{H} by analyzing the single system output $\mathcal{H}(x(t))$. Unlike time-invariant linear systems, however, a single observation of a time-varying linear system does not lead to a unique solution unless additional constraints on the system response are imposed. This is due to the fact that such systems introduce both time shifts (delays) and frequency shifts (Doppler shifts) to the input signal. It is now a well-established fact in the literature that a time-varying linear system \mathcal{H} can only be identified from a single observation if $\mathcal{H}(\delta(t))$ is known to lie within a region \mathcal{R} of the delay–Doppler space such that $\text{area}(\mathcal{R}) < 1$ [475, 476, 477, 478]. Identifiable time-varying linear systems are termed *underspread*, as opposed to nonidentifiable *overspread* linear systems, which satisfy $\text{area}(\mathcal{R}) > 1$ [477, 478].²

The response of an ULS can be described by a finite set of delays and Doppler shifts:

$$\mathcal{H}(x(t)) = \sum_{\ell=1}^L \alpha_\ell x(t - \tau_\ell) e^{j\nu_\ell t} \quad (15.214)$$

where (τ_ℓ, ν_ℓ) denotes a delay–Doppler pair and $\alpha_\ell \in \mathbb{C}$ is the complex attenuation factor associated with (τ_ℓ, ν_ℓ) . An important problem in this context is to characterize conditions on the bandwidth and temporal support of the input signal that ensure identification of such ULSs from a single observation. A small time–bandwidth product allows fast identification with low sampling rates.

Suppose that the delays and Doppers are limited to the region $(\tau_i, \nu_i) \in [0, \tau_{\max}] \times [-\nu_{\max}/2, \nu_{\max}/2]$. We use \mathcal{T} and \mathcal{W} to denote the temporal support and the two-sided bandwidth of the known input signal $x(t)$ used to probe \mathcal{H} , respectively. The probing signal is chosen as a finite train of pulses:

² It is still an open research question as to whether *critically spread* linear systems, which correspond to $\text{area}(\mathcal{R}) = 1$, are identifiable or nonidentifiable [478]; see [477] for a partial answer to this question for the case where \mathcal{R} is a rectangular region.

$$x(t) = \sum_{n=0}^{N-1} x_n h(t - n\tau), \quad 0 \leq t \leq \mathcal{T} \quad (15.215)$$

where $h(t)$ is a prototype pulse of bandwidth \mathcal{W} that is (essentially) temporally supported on $[0, \tau]$ and is assumed to have unit energy ($\int |h(t)|^2 dt = 1$), and $\{x_n \in \mathbb{C}\}$ is an N -length probing sequence. The parameter N is proportional to the time–bandwidth product of $x(t)$, which roughly defines the number of temporal degrees of freedom available for estimating \mathcal{H} [479]: $N = \mathcal{T}/\tau \propto \mathcal{T}\mathcal{W}$. As in the radar setting, we assume that $\tau_{\max} < \tau$, and $\nu_{\max} \ll \mathcal{W}$. Under these assumptions, the Doppler focusing method developed in the context of radar can be used to prove the following result:

Theorem 15.5 (Identification of parametric underspread linear systems). *Suppose that \mathcal{H} is a parametric ULS that is completely described by a total of L triplets $(\tau_i, \nu_i, \alpha_i)$. Then, under the assumptions stated above, and as long as the probing sequence $\{x_n\}$ remains bounded away from zero in the sense that $|x_n| > 0$ for every $n = 0, \dots, N - 1$, the system can be identified if the time–bandwidth product of the known input signal $x(t)$ satisfies*

$$\mathcal{T}\mathcal{W} \geq 8\pi L_\tau L_{\nu, \max} \quad (15.216)$$

where L_τ is the number of distinct delays, and $L_{\nu, \max}$ is the maximum number of Doppler shifts associated with any one of the distinct delays. In addition, the time–bandwidth product of $x(t)$ is guaranteed to satisfy (15.216) as long as $\mathcal{T}\mathcal{W} \geq 2\pi(L + 1)^2$.

15.7.3 Ultrasound imaging

We next show how FRI modelling can be used to obtain ultrasound images at rates much lower than Nyquist, following the ideas in [430, 453]. The main novelty in this context is that not only can the sampling rate be substantially reduced, but the required digital processing, which takes on the form of *beamforming*, is performed on the low-rate samples without the need for interpolation.

Ultrasound transmission

In diagnostic ultrasound, imaging is performed by transmitting a pulse along a narrow beam from an array of transducer elements. During its propagation, echoes are scattered by acoustic impedance perturbations in the tissue and detected by the array elements. The data, collected by the transducers, is sampled and digitally integrated in a way referred to as beamforming, which results in SNR enhancement and improvement of angular localization. Such a beamformed signal, referred to as a beam, forms a line in the image [480, 481].

Consider the array depicted in Fig. 15.58, comprising M transducer elements, aligned along the x axis. Denote by δ_m the distance from the m th element to the reference receiver m_0 set at the origin ($\delta_{m_0} = 0$). A pulse of energy, $h(t)$, is transmitted at $t = 0$ along a relatively narrow beam, whose central axis forms an angle θ with the axis z . Focusing the energy pulse along such a beam is achieved by applying appropriate time

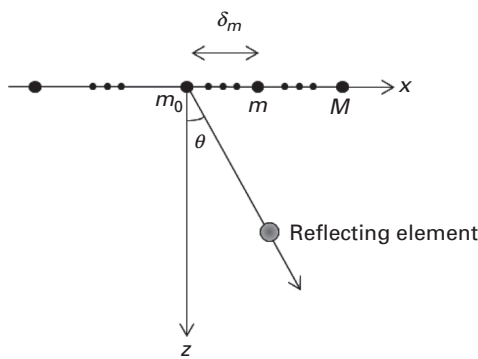


Figure 15.58 M receivers aligned along the x axis. An acoustic pulse is transmitted in a direction θ . The echoes scattered from perturbation in the radiated tissue are received by the array elements.

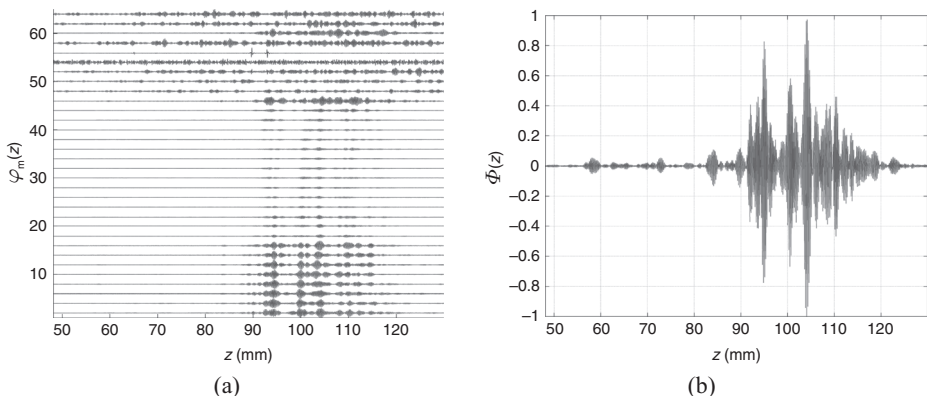


Figure 15.59 (a) Signals detected for cardiac imaging following the transmission of a single pulse. The vertical alignment of each trace matches the index of the corresponding receiver element. (b) Beamformed signal obtained by combining the detected signals with appropriate time-varying time delays. The data was acquired using a GE breadboard ultrasonic scanner [430].

delays to modulated acoustic pulses, transmitted from the different antennas in the array. The echoes of the transmitted pulse are received in the array elements. Ignoring noise for now, the detected signal in the m th antenna can be written as

$$\varphi_m(t) = \sum_{\ell=1}^L a_{\ell,m} h(t - t_{\ell,m}), \quad (15.217)$$

where L is the number of scattering elements, distributed throughout the sector radiated by the transmitted pulse, $t_{\ell,m}$ denotes the time in which the reflection from the ℓ th element arrived at the m th receiver, and $a_{\ell,m}$ denotes the reflection's amplitude, as detected by the m th receiver. Figure 15.59(a) depicts signals detected by 32 out of 64 active array elements for a cardiac image of a healthy volunteer. Note that the z -axis represents time.

From (15.217) it follows that the received signal in each antenna can be modeled as a stream of pulses. Therefore, in principle we may apply FRI sampling methods, as explained throughout the chapter, to each receiver element individually in order to sample the detected signals at a low rate and then determine the positions of the scattering elements along the beam. A B-mode image³ can then be formed by transmitting over all feasible θ , and deriving a geometric model for estimating the two-dimensional position of a scattering element, based on the delays of pulses associated with it. This approach, however, faces two fundamental obstacles. The first is the low SNR at each of the detected elements, as can be seen in Fig. 15.59(a), due to the strong noise. The second is proper interpretation of the estimated signal parameters, considering the profile of the transmitted beam. Owing to the difference in their geometric location, each of the array elements detects a signal with a different delay compared with the reference signal at m_0 .

In standard ultrasound imaging, both these difficulties are overcome by the process of *beamforming*, described next, which increases the SNR and focuses the signal [480, 481].

Beamforming

Beamforming refers to averaging the detected signals, after their alignment with appropriate time-varying delays, as depicted in Fig. 15.59(b). This results in a single focused beam with improved angular localization of the scattering structures and improved SNR.

To obtain a mathematical description of beamforming, consider a pulse, transmitted by the array at $t = 0$, in the direction θ . The pulse propagates through the tissue at speed c , so that at time $t \geq 0$ its coordinates are $(x, z) = (ct \sin \theta, ct \cos \theta)$. A potential point reflector located at this position scatters the energy, such that the echo is detected by all array elements at a time depending on their locations. Denote by $\varphi_m(t; \theta)$ the signal detected by the m th element and by $\hat{\tau}_m(t; \theta)$ the time of detection. It is then readily seen that:

$$\hat{\tau}_m(t; \theta) = t + \frac{d_m(t; \theta)}{c}, \quad (15.218)$$

where $d_m(t; \theta) = \sqrt{(ct \cos \theta)^2 + (\delta_m - ct \sin \theta)^2}$ is the distance traveled by the reflection. Beamforming involves averaging the signals detected by multiple receivers while compensating the differences in detection time. In that way we obtain a signal containing the intensity of the energy reflected from each point along the central transmission axis θ .

Using (15.218), the detection time at m_0 is $\hat{\tau}_{m_0}(t; \theta) = 2t$ since $\delta_{m_0} = 0$. Applying an appropriate delay to $\varphi_m(t; \theta)$, such that the resulting signal $\hat{\varphi}_m(t; \theta)$ satisfies $\hat{\varphi}_m(2t; \theta) = \varphi_m(\hat{\tau}_m(t; \theta))$, we can align the reflection detected by the m th receiver with the one detected at m_0 . Denoting $\tau_m(t; \theta) = \hat{\tau}_m(t/2; \theta)$ and using (15.218), the following aligned signal is obtained:

³ B-mode is a common ultrasound imaging technique, where the resulting image displays a two-dimensional cross-section of the tissue being imaged.

$$\begin{aligned}\hat{\varphi}_m(t; \theta) &= \varphi_m(\tau_m(t; \theta); \theta), \\ \tau_m(t; \theta) &= \frac{1}{2} \left(t + \sqrt{t^2 - 4(\delta_m/c)t \sin \theta + 4(\delta_m/c)^2} \right).\end{aligned}\quad (15.219)$$

The beamformed signal results from averaging the aligned signals:

$$\Phi(t; \theta) = \frac{1}{M} \sum_{m=1}^M \hat{\varphi}_m(t; \theta). \quad (15.220)$$

Such a beam is optimally focused at each depth and hence exhibits improved angular localization and enhanced SNR.

Ultrasound imaging systems perform the beamforming process in (15.219) and (15.220) in the digital domain: The analog signals $\varphi_m(t; \theta)$ are sampled individually, so that the delays in (15.219) can be applied digitally. Typically, the sampling interval is on the order of nanoseconds, resulting in sampling rates that are sometimes as high as several hundred MHz. To overcome the demand for such high rates, often the sampling rate is reduced to tens of MHz followed by digital interpolation. However, the processing, or beamforming rate, still remains high. As imaging systems evolve, the amount of elements participating in the imaging cycle continues to grow. Consequently, large amounts of data need to be transmitted from the system front end and digitally processed in real time. This motivates reducing the amounts of data as close as possible to the system front end.

Sub-Nyquist beamforming

In [430, 453] it is shown that the time-domain beamforming introduced in (15.219) can be replaced by Fourier-domain beamforming. Denoting the Fourier coefficients of the beamformed signal $\Phi(t; \theta)$ and the individual signals $\varphi_m(t)$ by $c[k]$ and $\Upsilon_m[k]$ respectively, we have that

$$c[k] = \frac{1}{M} \sum_{m=1}^M \sum_n \Upsilon_m[k-n] Q_{k,m,\theta}[n], \quad (15.221)$$

where $Q_{k,m,\theta}[n]$ is a pre-computed function which depends on the array geometry and on the angle θ . As shown in [453], this function decays quite rapidly so that in practice only a small number of elements in the sum are needed to compute $c[k]$.

The relationship in (15.221) allows one to carry out the beamforming process entirely in the frequency domain. Since the beamformed signal is typically narrow band, this implies that only a small number of coefficients $\Upsilon_m[k]$ are needed to compute all nonzero values of $c[k]$, from which the beamformed signal can be determined. Throughout the chapter we showed how low-rate sampling can be used to determine a small set of Fourier coefficients. Thus, the beamformed signal may be computed by using the low-rate sampling techniques introduced in this chapter to obtain a small set of Fourier coefficients $\Upsilon_m[k]$, and then applying (15.221). This allows us to exploit the low bandwidth of the ultrasound signal and bypass the oversampling dictated by digital implementation of beamforming in time.

To further reduce the rate beyond the bandwidth of $\Phi(t; \theta)$, we exploit the fact that, as shown in [430], the beamformed signal can be well approximated by a stream of pulses of the form

$$\Phi(t; \theta) = \sum_{\ell=1}^L b_\ell h(t - t_\ell), \quad (15.222)$$

where t_ℓ denotes the time in which the ℓ th reflection arrived at the reference receiver. Using FRI or CS techniques, this implies that the required delays t_ℓ and amplitudes b_ℓ can be determined from only a small number of Fourier coefficients $c[k]$. Thanks to (15.221), this translates into a small number of samples of each of the individual signals $\varphi_m(t)$. We therefore conclude that each signal may be sampled at a low rate using FRI sampling. After performing a DFT, the samples are combined via (15.221) to obtain the Fourier coefficients of the beamformed signal. Using FRI or CS methods, the delays t_ℓ and amplitudes b_ℓ are computed, based on which the appropriate line in the image is plotted.

Simulations and results

We now present simulation results, taken from [453], that demonstrate low-rate frequency-domain beamforming. We also show images obtained by a stand-alone ultrasound machine. These simulations prove the feasibility of sub-Nyquist processing for medical ultrasound, leading to the potential of considerable reduction in future ultrasound machines size, power consumption, and cost.

To demonstrate low-rate beamforming in frequency and evaluate the impact of rate reduction on image quality, we applied the method on *in vivo* cardiac data. The data acquisition setup consisted of a pulse with a carrier frequency of 16 MHz, leading to 3360 real-valued samples when sampled at the Nyquist rate. To perform beamforming in frequency we used a subset of 100 DFT coefficients. This implies 28-fold reduction in sampling compared with standard beamforming. The resulting images, corresponding to two different frames, are shown in Figs. 15.60(b) and (d). Although the images are not identical to those obtained by standard beamforming (Figs. 15.60(a) and (c)), it can easily be seen that this approach allows to reconstruct both strong reflectors and speckle noise.

We next show the results of low-rate frequency-domain beamforming implemented on an ultrasound imaging system. The lab setup used for implementation and testing is shown in Fig. 15.61 and includes a GE ultrasound machine, a phantom, and an ultrasound scanning probe.

The breadboard ultrasonic scanner contains 64 acquisition channels. The radiated depth $r = 15.7$ cm and speed of sound $c = 1540$ m/sec yield a signal of duration $T = 2r/c \simeq 204$ μ sec. The acquired signal is characterized by a narrow bandpass bandwidth of 1.77 MHz, centered at a carrier frequency $f_0 \approx 3.4$ MHz. The signals are sampled at the rate of 50 MHz and then are digitally demodulated and downsampled to the demodulated processing rate of $f_p \approx 2.94$ MHz, resulting in 1224 real-valued samples per transducer element. Linear interpolation is then applied in order to improve beamforming resolution, leading to 2448 real-valued samples. Low-rate processing is

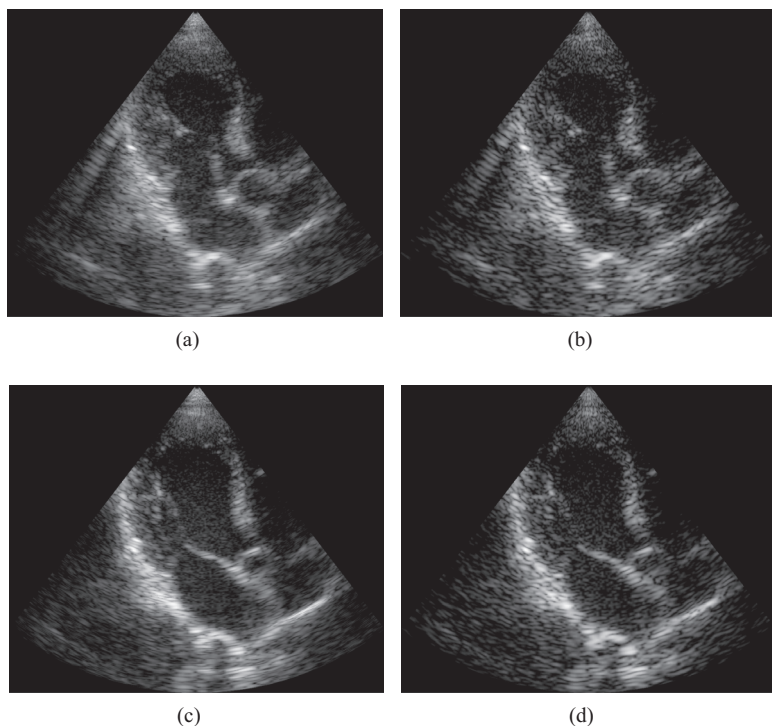


Figure 15.60 Simulation results on *in vivo* cardiac data taken from [453]. The first row, (a),(b), corresponds to frame 1, the second row, (c),(d), corresponds to frame 2. (a),(c) Time-domain beamforming at the Nyquist rate. (b),(d) Frequency-domain beamforming at 1/28 of the Nyquist rate.



Figure 15.61 Lab setup: Ultrasound system, probe, and cardiac phantom.

performed on the data obtained in real time by scanning a heart with a 64-element probe by using only 100 DFT coefficients of the beamformed signal. These are computed using 120 DFT coefficients of each one of the detected signals. This corresponds to 240 real-valued samples used for beamforming in frequency compared with 2448 samples

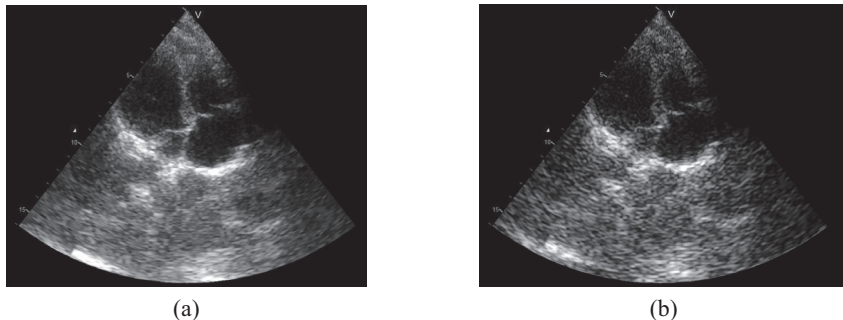


Figure 15.62 Cardiac images obtained by the demo system of [453]. (a) Time-domain beamforming. (b) Frequency domain beamforming, obtained with 12-fold reduction in processing rate.

when sampling at the Nyquist rate. The images obtained by low-rate beamforming in frequency and standard time-domain beamforming are presented in Fig. 15.62. As can be readily seen, sufficient image quality is retained despite the significant reduction in sampling and processing rates.

15.8 Exercises

1. Determine the τ -local rate of innovation of the following signals for two choices of $h(t)$: $h(t) = e^{-t^2/2}$ and $h(t) = \beta^p(t)$ where $\beta^p(t)$ is the p th-order B-spline function.
 - a. $x(t) = \sum_{n \in \mathbb{Z}} a[n]h(t - n\tau).$
 - b. $x(t) = \sum_{\ell=1}^L \alpha_\ell h(t - t_\ell).$
 - c. $x(t) = \sum_{n=1}^N \sum_{\ell=1}^L \alpha_\ell h(t - t_\ell - n\tau).$
 - d. $x(t) = \sum_{n \in \mathbb{Z}} \sum_{\ell=1}^L a_\ell[n]h(t - n\tau) \sin(\omega_\ell t).$
2. Establish the equivalence between (15.13) and (15.14) by noting that $a[m] = \tilde{a}[m] - \tilde{a}[m - 1]$ and substituting this relation into (15.13).
3. Let $y(t) = \overline{h(-t)} * x(t)$ where $h(t)$ is a given pulse bandlimited to π/T , and let $1/T$ denote the Nyquist rate of $y(t)$. Show that $y[n] = \overline{h[-n]} * x[n]$ where $y[n] = y(nT)$, $h[n] = h(nT)$ and $x[n]$ are samples at rate $1/T$ of a bandlimited version of $x(t)$.
4. In Section 15.2.1 we developed the MF estimate of a single delay and amplitude by minimizing a least-squares error in the time domain. In this exercise we derive a frequency-domain equivalent. Suppose we are given m samples of a single exponential function: $X[k] = a_1 e^{-j2\pi k t_1 / \tau}$ for $k = 0, 1, \dots, m-1$. We would like to estimate a_1 and t_1 from $X[k]$.
 - a. Develop an expression for the values of a_1 and t_1 that minimize the least-squares error $\sum_{k=0}^{m-1} |X[k] - a_1 e^{-j2\pi k t_1 / \tau}|^2$.
 - b. Relate your answer to equations (15.20) and (15.21).
5. 1. Consider the signal $x(t) = \sum_{\ell=1}^L \sum_{n \in \mathbb{Z}} a_\ell h(t - t_\ell - n\tau)$ where $h(t) = \text{sinc}(t)$.
 - a. Determine whether or not $x(t)$ is FRI. If so, then what is its rate of innovation?

- b. Determine the CTFT of $x(t)$.
2. Repeat the previous part with:
- $x(t) = \sum_{\ell=1}^L a_\ell h(t - t_\ell)$.
 - $x(t) = \sum_{\ell=1}^L \sum_{n \in \mathbb{Z}} a_\ell[n] h(t - t_\ell - n\tau)$.
6. Suppose that $Y[k]$ obeys (15.32) with $\omega_1 = 2\pi \cdot 0.2, \omega_2 = 2\pi \cdot 0.7$ and $a_1 = 1, a_2 = 0.2$. We are given noisy observations of $Y[k]$ where the noise is zero-mean white Gaussian noise with variance equal to 0.1. Estimate the values u_ℓ in (15.32) using Prony's method for the following choices of \mathcal{K} . Explain your results:
- $\mathcal{K} = \{0, 1, \dots, 9\}$;
 - $\mathcal{K} = \{5, 6, \dots, 14\}$;
 - $\mathcal{K} = \{0, 2, 4, \dots, 18\}$.
7. Let $\mathbf{A}_{n \times m}$ with $n \geq m$ be a full column-rank matrix, let $\mathbf{C}_{m \times k}$ with $m \leq k$ be a full row-rank matrix, and let \mathbf{B} be a matrix with rank r . Show that the rank of \mathbf{ABC} is equal to r .
8. Consider a Hankel matrix \mathbf{A} . Show that the matrix \mathbf{A} that minimizes the error $\|\mathbf{B} - \mathbf{A}\|_F^2$ is obtained by averaging the skew-diagonals of \mathbf{B} .
9. In this exercise we examine several methods for estimating the unknown amplitudes and frequencies in the model (15.26).
- Suppose that $t_1 = 0, t_2 = 0.1, t_3 = 0.41$, the amplitudes are all set to 1 and $\tau = 1$. Plot the performance of MUSIC, root-MUSIC, and matrix pencil for $m = 30$ measurements as a function of SNR between -10 to 10 dB.
 - Repeat the previous part where now we use a compressed sensing approach with different choices of resolution step $\Delta = 0.02, 0.01$.
 - Repeat the question where now $a_1 = 0.1, a_2 = 1, a_3 = 3$. Explain the results.
10. A special case of the model (15.26) occurs when $L = 1$ so that only one exponent is present in the sum: $Y[k] = ae^{-j2\pi t_0 k/\tau}, k \in \mathcal{K}$.
- What is the minimal number of samples $Y[k]$ needed in order to recover a and t_0 ?
 - Write out Algorithms Algorithm 15.1–Algorithm 15.5 explicitly for this special case.
 - Let $a = 1, t_0 = .2, \tau = 1$. Suppose we are given noisy measurements $Z[k] = Y[k] + W[k]$ where $W[k]$ are zero-mean iid Gaussian variables with variance σ^2 , and $\mathcal{K} = \{0, 1, 2, 3\}$. Plot the performance of the algorithms above as a function of SNR for $\sigma^2 = [0 : 0.01 : .5]$.
11. Suppose that $p(t)$ is a periodic waveform with period T and let $d[k]$ denote its Fourier series coefficients. We filter $p(t)$ with $g(t)$ and denote the filtered waveform by $\tilde{p}(t) = p(t) * g(t)$. Show that the Fourier series coefficients of $\tilde{p}(t)$ are given by $\tilde{d}[k] = d[k]G(\frac{2\pi}{T}k)$.
- Suppose that the periodic stream of pulses $x(t)$ is contaminated by white noise. We sample $x(t)$ using a single filter and consider two approaches: coset sampling and sampling with a sum-of-sincs prefilter. Explain which method is preferable in terms of the output SNR.
12. Consider the MSE bound of (15.163) for estimating a single shifted pulse $x(t) = a_1 h(t - t_1)$ defined over $[0, \tau]$ from noisy measurements $y(t) = x(t) + w(t)$ as in (15.155), where $w(t)$ is continuous-time white Gaussian noise with variance σ^2 .

- a. Plot the bound for $h(t) = \delta(t)$ and the following sampling functions $\varphi_n(t)$ in (15.159):

a. $\varphi_n(t) = e^{j2\pi nt/\tau}$.

b. $\varphi_n(t) = \beta^0(t)$, where $\beta^0(t)$ is the 0th order B-spline function.

Suppose now that $h(t) = 1$ for $0 \leq t \leq \tau/2$ and $h(t) = 0$ otherwise.

- b. Repeat the previous section for this choice of $h(t)$.

- c. Suggest sampling functions $\varphi_n(t)$ that will yield a lower bound than those obtained by the two choices above.

- 13.** Consider a sum of exponents of the form

$$Y[k] = \sum_{\ell=1}^L a_\ell e^{-j\omega_\ell k}, \quad k = 0, 1, \dots, m-1. \quad (15.223)$$

Suppose that $N < m$ of the values ω_ℓ are known and the remaining frequencies are unknown. The amplitudes a_ℓ are all unknown. Suggest two methods to recover the unknown amplitudes and frequencies based on the techniques discussed in this chapter, modified to take into account the known frequencies.

- 14.** Suppose we have a random process composed of L complex exponentials

$$Y[k] = \sum_{\ell=1}^L a_\ell e^{-j(\omega_\ell k + \theta_\ell)}, \quad k = 0, 1, \dots, m-1, \quad (15.224)$$

where θ_ℓ are iid random variables uniformly distributed over $[0, 2\pi)$ and the amplitudes a_ℓ are zero-mean iid random variables with variance σ_ℓ^2 .

- a. Show how to estimate ω_ℓ using a covariance-based method as discussed in Section 15.2.7.
- b. Suppose now that the phases are known, and the amplitudes are unknown deterministic values. Can we use the annihilating filter method to recover the unknown frequencies?